Photosensors based on colloidal quantum dots

Vladimir P. Ponomarenko,[a,b] **Victor S. Popov,**[a,b]* **Ivan A. Shuklov,**[b] **Victor V. Ivanov,**[b]
Vladimir F. Razumov[b,c]

[a] *Enterprise 'RD&P Center 'Orion',*
 ul. Kosinskaya 9, 111538 Moscow, Russian Federation
[b] *Moscow Institute of Physics and Technology (MIPT),*
 Institutskiy per. 9, 141701 Dolgoprudny, Moscow Region, Russian Federation
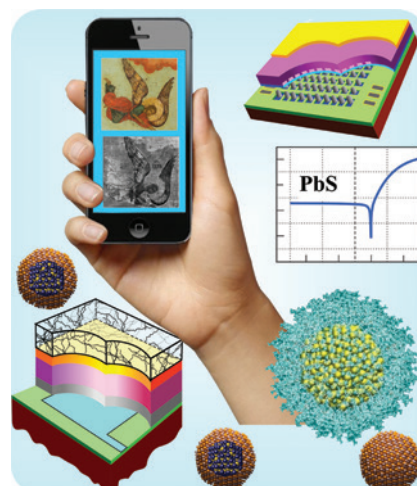[c] *Federal Research Center of Problems of Chemical Physics and Medicinal Chemistry*
 RAS (FRC PCP MC RAS)
 prosp. Akademika Semenova 1, 142432 Chernogolovka, Moscow Region, Russian Federation

Photosensing based on colloidal quantum dots (CQDs) is a rapidly developing area of infrared photoelectronics. The use of colloidal quantum dots markedly simplifies the manufacture, decreases the restrictions to the pixel pitch of the photosensitive elements, and reduces the production cost, which facilitates the wide use of IR sensors in various technological systems. This paper is the first exhaustive overeview of the architectures, methods of manufacturing and basic properties of photonic sensors based on colloidal quantum dots of compounds of Group II, IV and VI elements. Characteristic features of the synthesis and roles of the ligands and CQD morphology in the design of photosensors are considered in detail. The structures of photoresistive, photodiode and phototransistor elements based on HgTe, HgSe, PbS and PbSe CQDs, which are sensitive in various spectral ranges, are described. The main parameters of the most advanced optoelectronic devices based on colloidal quantum dot structures are presented. The key trends in the development of this area are analyzed.
The bibliography includes 361 references.

Keywords: colloidal quantum dot, ligand, Ostwald ripening, spectral range, photodiode, detectivity.

Contents

1. Introduction

The environment is perceived by humans mainly by vision and hearing organs, with 70% of information being gained by vision. Despite the unique characteristics of the human eye as an optical photosensor,[1] it can perceive only things in a rather narrow range of electromagnetic radiation wavelengths, from ~0.38 μm to ~0.72 μm (visible region), while leaving subjects in X-ray ($10^{-6}-10^{-2}$ μm), ultraviolet (0.1–0.4 μm) and infrared (0.8–100 μm) electromagnetic wavelengths beyond the visibility.

The attempts to fabricate devices that would detect and visualize ultraviolet and infrared radiation sources, which were actively started after the World War II, initiated a new research area called optoelectronics; the milestones of its development have been described in a number of publications.[2−6] Optoelectronic devices form the basis for night vision, thermal imaging, infrared direction finding, laser location, optical data transmission and other systems. Of particular interest are

research and development related to the elemental base of modern optoelectronics, that is, photosensors sensitive to near-infrared (NIR, $0.8-1.0$ μm), short-wave infrared (SWIR, $1.0-3.0$ μm), mid-wave infrared (MWIR, $3-5$ μm), long-wave infrared (LWIR, $8-14$ μm), very long-wave infrared (VLWIR, $14-30$ μm), and extremely-long wave infrared ($30-100$ μm) electromagnetic radiation.

There exist a variety of approaches to the design of photosensing devices. The design and manufacturing of photosensors for the wavelength range of $0.4-0.9$ μm covering the visible and near-infrared light are largely related to image intensifiers, which use the external emission of electrons excited by absorption of photons focused by an IR lens on the photocathode of an electro-optical converter.[6]

For spectral wavelengths $\lambda > 0.9$ μm, development of photosensors is mainly associated with the solid-state semiconductor photoelectronics based on the internal photoelectric effect. In photonic sensors, the observed signal is the measure of excitation by incident photons of the electronic system of a semiconducting material forming the photosensitive structure. There are a number of architectures for photonic elements that form the basis of virtually all types of photosensors used in both the infrared and ultraviolet and visible regions. Most often, single-area and line photosensors with no more than 200 elements are designed on the basis of photoresistors. There are also examples of photodetector arrays. For example, a latest-generation photodetector array is a two-dimensional GaAs/AlGaAs-based quantum well infrared photodetector (QWIP), which uses the photoresistive effect.[4] Energy barrier photodiodes can be based on both homo- (p-n) and heterojunctions of various types (P-n, N-p, P-p, n-N), Schottky barriers, p-i-n homo- and heterojunctions, avalanche gain, bariode heterosystems, injection diodes, *etc*. Most of modern 2D photodetector arrays are based on photodiodes. Depending on the required sensitivity range, operating temperature and operation speed, photodetectors are manufactured using various materials such as Ge and Si (in particular, those doped with Hg, Au, Zn, B, As, P, Al, In, S, Mg, and other ions), PbS, PbSe, PbTe, CdS, CdSe, InSb, InP, GaAs, InAs, InGaAs, CdHgTe, and so on.[7-9] In the far-IR region, apart from photodetectors, non-selective thermal detectors (microbolometers) are often used.[4]

The modern trend of development of solid-state IR photosensors is associated with the design of 2D photodetector arrays. Currently, they are being developed virtually for all semiconductor compounds that have a sufficient photosensitivity in the ultraviolet and near-, mid- and far-IR regions and in the terahertz (THz) region. These camera arrays (N×N format in systems without image scanning) and TDI subarrays [M×N format, where M = 2, 4, 8, 12, for the *time delay and integration* (*TDI*) mode in optical mechanical scanning systems) are

referred to as second-generation solid state photosensing devices.[4]

A considerable progress has been made in the development of second-generation solid-state semiconductor photosensors. Imaging arrays comprising more than a few million elements with 1280×1024, 1920×1080, 2048×2048, and 4096×4096 formats (Fig. 1) have now been fabricated for the main infrared spectral regions, $0.9-1.7$ μm, $3-5$ μm and $8-12$ μm, corresponding to the transparency windows of the Earth's atmosphere.[10,11] Lately, special attention has been paid to the development of multiband devices sensitive in several spectral regions. The possibilities of increasing the operating temperature are being investigated. The ways for reducing size, weight and power consumption of photosensors [size-weight-and-power (SWaP) concept of development] are being explored.

Meanwhile, in recent years, certain drawbacks of the currently developed technologies of infrared and ultraviolet photosensors based on solid-state semiconductor electronic materials, structures and approaches have become more obvious, and they restrict some applications of the developed devices. First of all, this refers to complexity of integrating photosensor arrays with microelectronic readout integrated circuits (ROIC), which restricts the format and the minimum size of photosensitive elements; high cost of the starting semiconductor materials; the need to use cryogenic operating temperatures; and sophisticated and expensive manufacturing equipment, resulting in high cost of the final product. This stimulates the search for alternative approaches to the production of components for optoelectronics, new photosensitive materials and techniques for multi-element photosensors and photosensor arrays operating in ultraviolet and infrared spectral ranges.

The last decades witness the rapid increase in the number of studies directed towards the design of photosensors using low-
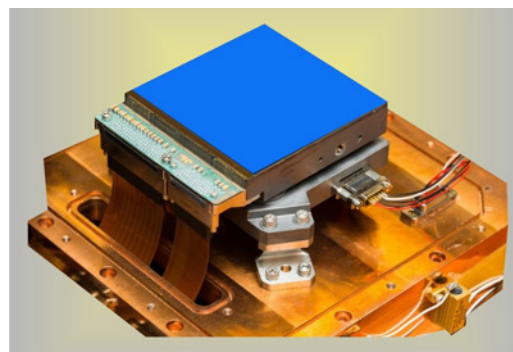
Figure 1. Photosensitive element based on $Cd_xHg_{1-x}Te$ photodiode ($\lambda_c = 2.5$ μm) of 4096×4096 format for the James Webb space telescope; λ_c is the cut-off wavelength.[10]

V.P.Ponomarenko. Professor, Doctor of Science, Chief designer at the 'Orion', Head of Physical Electronics Department at MIPT.
E-mail: orion@orion-ir.ru
Current research interests: solid state physics, photosensorics, quantum dots.
V.S.Popov. PhD in Chemistry. Head of the department at the 'Orion'. Head of the laboratory at MIPT.
E-mail: popov.vs@mipt.ru
Current research interests: semiconductor 0D-, 1D-, 2D-nano-materials, photosensorics, physics and chemistry of nanomaterial surfaces.
I.A.Shuklov. Dr. rer. nat. Leading Researcher and Docent at MIPT.
E-mail: Shuklov.ia@mipt.ru

Current research interests: nanochemistry, quantum dots, solvent effect, catalysis.
V.V.Ivanov. Professor, RAS Corresponding Member, Doctor of Science, Director of the Institute for Quantum Technologies at MIPT.
E-mail: ivanov.vv@mipt.ru
Current research interests: nanomaterials, chemical physics, printed electronics, optoelectronics, colloidal photonics.
V.F.Razumov. Professor, RAS Corresponding Member, Doctor of Science, Chief Scientist, Head of Laboratory at FRC PCP MC RAS, Chief Scientist, Head of Laboratory at MIPT.
E-mail: razumovvf@list.ru
Current research interests: chemical physics.

Translation: Z.P.Svitanko

V.P.Ponomarenko, V.S.Popov, I.A.Shuklov, V.V.Ivanov, V.F.Razumov
Russ. Chem. Rev., 2024, **93** (4) RCR5113

3 of 48

dimensional materials and structures. Examples are structures based on graphene and graphene-like and related 2D nanomaterials, non-graphene 2D materials composed of Group IV, V, VI and IIIa elements, nano-sized layers of topological insulators like bismuth telluride, *etc*.[12–15] The design of photosensors based on type-II superlattices (T2SL) is being successfully developed. The T2SL structures are alternating nano-sized layers with different band-gap semiconductors (*InAsSb/InSb, InGaAs/GaAsSb, InAs/GaSb, PbTe/PbS, PbTe/SnTe*).[16] The properties of T2SL structures often eliminate some drawbacks inherent in solid-state semiconductor photosensors based on 3D single crystals and epitaxial layers, *e.g.*, increase the sensor operating temperature owing to significantly lower dark currents.

The last two decades witnessed the appearance a new trend in the design of photosensors, particularly, the use of so-called colloidal quantum dots (CQDs), the spectral properties of which are specified by the average size of semiconductor nanoparticles, which is varied in the 2–50 nm range. Meanwhile, the width of the luminescence spectrum of a single nanoparticle at room temperature is only 20–30 nm. Thus, quite a small set of luminescent quantum dots based on $A^{II}B^{VI}$, $A^{III}B^{V}$ or $A^{IV}B^{VI}$ type semiconductors easily cover the spectral range from 350 to 3500 nm owing to variation of their size.[17, 18]

The size dependence of the absorption and luminescence spectrum properties of ultradisperse semiconductors was first demonstrated in 1981 by A.I.Ekimov and A.A.Onushchenko from the S. I.Vavilov State Optical Institute, in relation to CuCl nanoparticles grown in multicomponent silicate glasses during thermally initiated diffusion phase decomposition of a supersaturated solid solution, and theoretically substantiated by Al.L.Efros and A.L.Efros.[19, 20] Independently, L.E.Brus the same dependence for a CdS dispersion.[21, 22] Over the following several years, this effect was experimentally detected and confirmed for ultradisperse particles of a number of semiconductors such as CdS, CuBr, CdSe, PbS, ZnS, Zn_3P_2, and Cd_3P_2.[23–28] The term 'quantum dot' (QD) was first introduced in 1988 by Reed *et al.*,[29] who studied the electron transport in quasi-zero-dimensional semiconductor nanocrystals and showed that an electron behaves in a nanocrystal as in a three-dimensional potential well. When the nanocrystal size becomes smaller than the exciton Bohr radius, the continuous spectrum of allowed charge carrier energies (characteristic of the conduction and valence bands of bulk crystals) is replaced by a discrete spectrum. The size of such nanocrystals consisting of $10^3–10^5$ atoms and called quantum dots was found to range from 2 to 50 nm. A similar size quantization of the energy spectrum was also observed for nanocrystals formed as nanoparticle dispersions in organic or aqueous solutions. These nanocrystals are called colloidal quantum dots.

In 1993, Murray, Norris and Bawendi[30] proposed a facile and highly efficient chemical method for the synthesis of quantum dots, which was called high-temperature colloidal synthesis. This method not only opened up new opportunities for studying CQDs, but also clarified the real prospects for their practical applications.

As a recognition of the significance of this research area and priority of the pioneering studies that initiated a new field of photonics that actively develops now, Louis Bruce, Alexey Ekimov and Alexander Efros were awarded the R.W.Wood Prize in 2006, while in 2008, Louis Bruce was awarded the Fred Kavli Prize in nanoscience. In 2023, Moungi Bawendi, Louis Bruce and Alexey Ekimov won the Nobel Prize in Chemistry.

The CQD-based approach to the fabrication of infrared photodetector arrays, which has actively developed in recent years, markedly simplifies the technology, reduces the pixel pitch limitation for the photosensitive elements and considerably reduces the cost of photodetector arrays.[31, 32] The vigorous development of this area in the last few years resulted in the fabrication of the first commercial imagers and cameras based on them, which operate in the spectral range from 0.4 to 2.1 μm.[33–36]

A number of reviews published over the past few years generally address the use of CQDs for a wide range of applications.[37, 38] In 2023, Mamiyev and Balayeva[39] considered various applications of PbS-based CQDs. The key achievements in the synthesis of PbS CQDs and the fabrication of thin films based on them are addressed by W.M.M.Lin *et al.*[40]

In addition, there are a number of specialized reviews devoted to particular issues of photosensor applications of CQDs. For example, V.Pejovic *et al.*[41] analyzed the advances in the CQD image sensor technology as of June, 2022. The protosensor applications of PbSe and PbS CQDs are addressed by M.C.Gupta *et al.*[42] and H.Wu and Z.Ning.[43]

Ponomarenko *et al.*[44] analyzed the architectures of photosensitive elements and described the advances in the CQD-based photoelectronics as of the beginning of 2021.

The present review gives the first comprehensive and detailed account of the architectures, fabrication methods and properties of photonic sensors based on colloidal quantum dots of Group II, IV and VI elements. The review describes the synthetic approaches, the influence of ligands and morphology of various CQDs used in photosensors. Functional diagrams are considered for photoresistor, photodiode and phototransistor elements with absorption layers based on HgTe, HgSe, PbS and PbSe colloidal quantum dots for operation in various spectral ranges, including hybrid elements using functional layers made of 2D materials. The parameters of the best optical devices based on colloidal quantum dot structures as of the beginning of 2024 are given. On the basis of publications of the last few years, we analyze the potential and development trends for the photonic sensors composed of colloidal quantum dots of compounds of Group II, IV and VI elements as one of the most promising new areas of quantum photosensorics.

2. Photosensing devices based on 3D semiconductor structures

2.1. Photosensor arrays based on 3D semiconductor structures. State of the art, benefits and drawbacks

The fabrication of second-generation two-dimensional photodetectors required the development of way for electrical connection (hybridization) of hundreds of thousands and millions of photosensitive elements made of semiconductor materials (Fig. 2) with an equal number of microelectronic input devices arranged in a silicon readout integrated circuit (ROIC). This is exemplified in Fig. 2, which shows the connection of an indium antimonide photodiode array to silicon ROIC. The development of the hybrid technology started in the second half of the 1970s. This required elaboration of a method for growing indium bumps with size and height variations of approximately fractions of a micrometre; development of special high-precision equipment for the thermocompression bonding of a group of bumps located on a silicon ROIC to a similar group located on an array of photosensitive elements.[45] The above hybridization
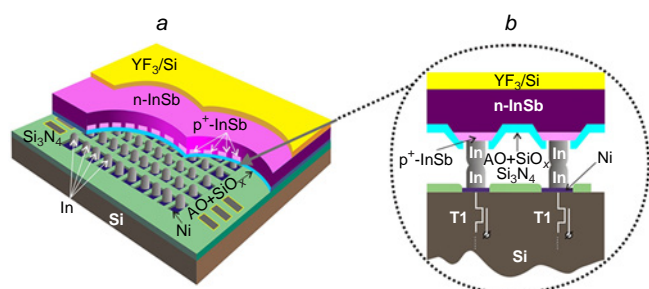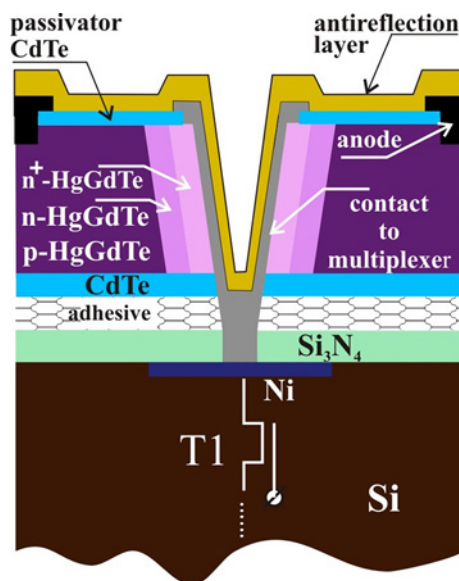
Figure 2. Hybridization of InSb photodiode array with Si ROIC wafer for signal readout and preliminary processing using indium bumps: (*a*) hybridized photosensitive elements and Si ROIC wafer; (*b*) two array elements connected by columnar indium bumps to the ROIC input devices (T1 transistor sources).

operation is a key issue for all second-generation photodetector arrays. Using this operation, photonic detector arrays were fabricated, including those of a mega-pixel format, based on InSb (1280×1024, 1920×1536), InGaAs (1280×1024) and CdHgTe (2048×2048, 4096×4096) photodiodes and multielement AlGaN arrays (320×256, 640×512).[11,12,46–51] The hybridization technique substantially influences the photosensor quality, since connection defects (bonding disruption between single bumps of the photodiode array and ROIC wafer due to their different heights, high resistance in the contact layer, *etc*.) give rise to non-functional photosensitive elements.

The hybridization operations performed using the above-described indium bumps restrict most appreciably characteristics of photosensor arrays for near and short-wave spectral regions of $0.7–3.0$ µm. The diameter of columnar indium bumps with minor variations of the diameter and height can hardly be made smaller than $3–5$ µm. Meanwhile, the maximum pixel pitch for photosensitive elements for arrays operating in the $0.4–1.7$ µm that provides the best spatial resolution for an electro-optical system is approximately 2 µm. For the mid-wave infrared range (MWIR) of $3–5$ µm, the pixel pitch should be approximately 4 µm. In the design of CdHgTe-based avalanche photodiodes (APD) in the early 2000s, a hybridization method of APD array with Si ROIC without using columnar or spherical indium bumps was developed; this gave so-called high density vertically integrated photodiodes (HDVIPs).[52] The architecture of an avalanche p-n-n$^+$ photosensitive element based on the CdTe/HgCdTe pair hybridized by the HDVIP process with silicon readout input is shown in Fig. 3.[52–54] The diameter of the vertical *via* formed by ion etching in CdTe/HgCdTe is approximately 6 µm. However, this hybridization method did not provide the required pixel pitch for photosensitive elements either.


Figure 3. Hybridization of a p-n-n$^+$ avalanche photodiode with the input to silicon readout circuit by the HDVIP process without using columnar (or spherical) indium bumps (in relation to the CdTe/HgCdTe array). The Figure was created by the authors using published data.[52–54]

Thus, hybridization of photodiode arrays and signal readout electronic circuits using columnar bumps or *via* holes (HDVIP method) is not only labour-consuming, requires the use of highly precise and expensive equipment, decreases the percentage yield of acceptable arrays and increases the cost of products, but also limits the pixel pitch of photosensitive elements for arrays not smaller than $3–5$ µm, which has an adverse effect on the spatial resolution of optoelectronic devices and complexes using such arrays.

2.2. Photosensor devices for near- and short-wave infrared regions: problems and solutions

Unlike the thermal imaging devices operating in the mid ($3–5$ µm) and far ($8–12$ µm) spectral regions and recording the intrinsic radiation of items heated to $240–970$ K, the devices operating in the $0.7–1.0$ µm and $1.0–3.0$ µm ranges record the intrinsic radiation of items heated to temperatures above 970 K and reflected radiation of, first of all, natural sources (Sun, Moon, stars, natural radiation of the night sky). The images obtained using special instruments in these spectral ranges by measuring the radiation reflected from an observed object have shadows and half-tones and thus allow highly accurate recognition of these objects or parts of objects that have no


| 0.4–0.7 µm | 1.0–3.0 µm | 3.0–5.0 µm | 8.0–14.0 µm |
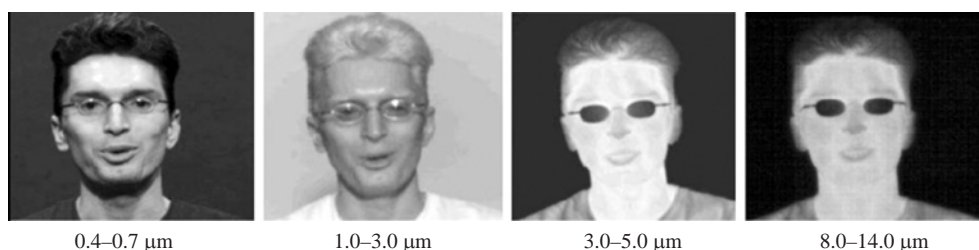
Figure 4. Facial images of the same person in different spectral ranges: $0.4–0.7$ µm (visible), $1.0–3.0$ µm (SWIR), $3.0–5.0$ µm (MWIR) and $8.0–14.0$ µm (LWIR).[55]

V.P.Ponomarenko, V.S.Popov, I.A.Shuklov, V.V.Ivanov, V.F.Razumov
Russ. Chem. Rev., 2024, **93** (4) RCR5113

5 of 48

temperature contrast. This is illustrated by Fig. 4, demonstrating that only visible $(0.38-0.72\ \mu m)$ and short-wave IR $(1.0-3.0\ \mu m)$ images make it possible to confidently recognize the facial features and, hence, identify a person.[55] Due to the inevitable differences in the reflectivity of different fabrics and dyes, the range of $1.0-3.0\ \mu m$ makes it possible to distinguish between camouflage outfits of different countries and thus to make the friend-or-foe identification. This indicates the relevance of development of advanced photosensors providing high-quality images in the NIR and SWIR ranges of electromagnetic radiation. The major part of the visible and near-IR ranges is covered by night vision devices (NVD); the photosensors of these devices are represented by generation III and III$^+$ vacuum electrical to optical converters with GaAs-based photocathodes with a negative electron affinity and cut-off wavelength of not more than $0.93\ \mu m$ and quantum efficiency of approximately 30% (Fig. 5, curve *6*).[56] The Sb–Rb–Cs or Sb-K–Cs bialkali photocathodes (*e.g.*, K_2CsSb and Rb_2CsSb), photocathodes based on GaAsP ternary solid solution, and Na-K–Sb–Cs multi-alkali photocathodes [*e.g.*, $(Cs)Na_3KSb$] (Fig. 5, curves *3*, *4*, *5*) have a higher quantum efficiency (30–55%), but their spectral sensitivity is limited to the visible and near-infrared spectral regions. The same is true for the super bialkali (SBA) and ultra bialkali (UBA) type photocathodes based on bialkali compounds manufactured by a specific technique resulting in an increase in the absolute sensitivity, but not in an extension of the spectral range.[57] The efforts of the last decades on the search for photocathodes with a cut-off wavelength extended to the short-wave IR (SWIR) region resulted in the development of new-generation photocathodes based on InGaAs and InGaAsP solid solutions and photocathodes based on InP/InGaAsP and InGaP/InGaAs heterojunctions with cut-off wavelengths at about $1.6\ \mu m$. The greatest progress was attained for photocathodes with InP/InGaAs heterojunction (Fig. 5, curve *9*). However, the wide use of such devices in night vision technology is hindered by their low quantum efficiency, not exceeding a few percent, and high cost.

The key NVD parameters (range of vision, probability of detection and recognition, noise protection and noise resistance, power consumption, *etc*.) depend on the external conditions under which NVD is used. The key external conditions of NVD operation (in passive systems without artificial light source) include

— spectral composition and level of the natural night illumination (NNI);

— atmospheric parameters along the observation track;
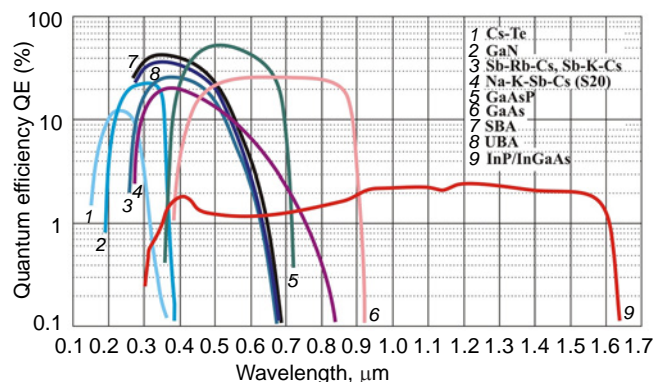
**Figure 5.** Photosensitivity spectra of some photocathodes used in modern EOCs.[56]

— atmospheric haze;

— brightness coefficients of natural entities and observation targets.

The natural night illumination of the Earth's surface at different times of the day, in various regions, at different weather conditions, *etc*. has been investigated for many years. Generally, the results of these studies can be summarized as follows.[58–60]

The major source of NNI is moonlight, which provides spectral irradiance of 1.8×10^{-3} W m^{-2} μm^{-1} at $\lambda\approx0.7\ \mu m$ near the Earth's surface; for the wavelength $\lambda\approx1.6\ \mu m$, this value decreases to approximately 1.2×10^{-3} W m^{-2} μm^{-1} (Fig. 6*a*).[58] The spectral irradiance generated by stars in the visible region in the wavelength range of $1.4-1.8\ \mu m$ is much lower. On a clear moonless night, the main natural sources of illumination are the airglow, starlight and zodiacal light. The main contribution to the ground illumination is made by airglow (Fig. 6*b*).[58] The night airglow is caused by various processes taking place in the upper atmospheric layers: recombination of ions formed upon photoionization during daytime under the influence of the solar radiation; reactions between oxygen, nitrogen and hydroxyl OH$^-$ accompanied by photon emission; luminescence caused by the passage of cosmic rays in the upper atmosphere; reactions involving lithium and sodium; and combination reactions between nitrogen and oxygen atoms accompanied by photon emission.

Comparison of these characteristics for the $0.4-0.9\ \mu m$ and $1.4-1.8\ \mu m$ spectral ranges shows that[61]

(a) the spectral irradiance from NNI regularly increases on going from the visible [from $\lambda\approx0.38\ \mu m$ (violet) to $0.78\ \mu m$
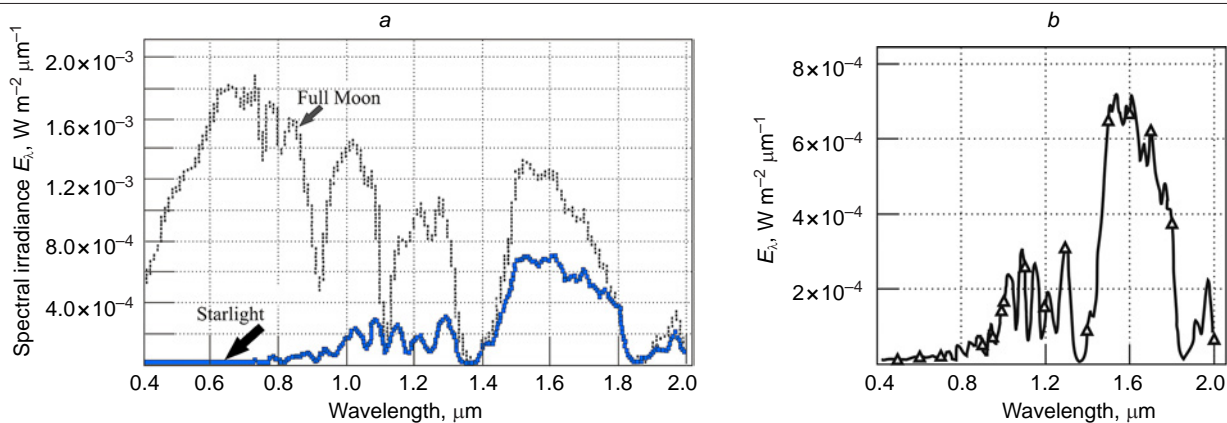
Figure 6. Spectral irradiance of natural night illumination: (*a*) with a full Moon; (*b*) airglow in a moonless night.[58]
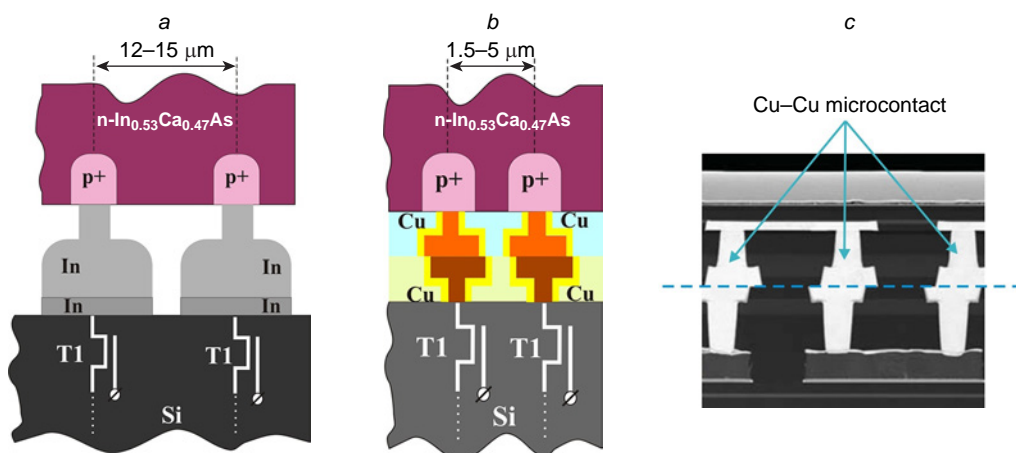
Figure 7. Hybridization of a 1280×1024 photodiode array based on InGaAs solid solution semiconductor with Si ROIC: (*a*) using indium bumps (17 µm pitch); (*b*) using planar Cu–Cu microcontacts (5 µm pitch); (*c*) TEM image of planar Cu–Cu microcontacts (3 µm pitch). The Figure was created by the authors using published data.[48, 64, 66]

(red)] to IR spectral region ($\lambda \geqslant 0.9$ µm); indeed, in the absence of moonlight, the average spectral irradiance for $\lambda = 0.6 - 0.8$ µm is $(1.5 - 3.0) \times 10^{-5}$ W m^{-2} µm^{-1}, while in the $1.4 - 1.8$ µm wavelength range, it increases to $(6.0 - 7.0) \times 10^{-4}$ W m^{-2} µm^{-1};

(b) air transparency is much higher in the near-IR range than in the visible range; for example, for the meteorological visibility $S_M = 10$ km, transmittance of a 1 km-thick atmospheric layer is 0.72 at $\lambda = 0.6$ µm and 0.93 at the centre of the transparency window ($1.4 - 1.8$ µm);

(c) brightness of the atmospheric haze decreases more than 10-fold in the $1.4 - 1.8$ µm wavelength range compared with thee visible region;

(d) NNI changes during the night from 10^{-1} W m^{-2} to 2.5×10^{-5} W m^{-2} (*i.e.*, by almost four orders of magnitude) in the $0.4 - 0.9$ µm spectral range, while in the $1.4 - 1.8$ µm range, this change is from 1.6×10^{-1} W m^{-2} to $(3 - 4) \times 10^{-3}$ W m^{-2};

(e) the contrast (observation target/background) is $1.4 - 1.5$ times higher in the $1.4 - 1.8$ µm wavelength range than in the $0.4 - 0.9$ µm range.

A comparative estimation of the ranges of vision L_1 and L_2 for two NVDs with identical optical systems, but different spectral sensitivity ranges was reported by Gusarova *et al.*[61] The L_1/L_2 ratio was calculated by the formula:

$$\frac{L_1}{L_2} = \frac{K_1}{K_2} \left(\frac{2 + K_2}{2 + K_1} \right)^{1/2} \times \frac{\displaystyle\int_{1.4}^{1.8} E_\lambda \tau_{a\lambda} S_{1\lambda} \, d\lambda}{\displaystyle\int_{0.4}^{0.9} E_\lambda \tau_{a\lambda} S_{2\lambda} \, d\lambda} \qquad (1)$$

where L_1 is the distance of action of NVD at which the detection of an object ensures recognition, K_1 is contrast, $\tau_{a\lambda}$ is the spectral atmospheric transmittance between the target and the observer, $S_{1\lambda}$ is the relative spectral sensitivity of a conventional detector operating in the $1.4 - 1.7$ µm range, equal to $S_{1\lambda}/S_{1\lambda \max}$, E_λ is the spectral irradiance on the target surface; L_2, K_2, $S_{2\lambda}$ are the same parameters for EOC with the sensitivity range of $0.4 - 0.9$ µm. The estimated L_1/L_2 ratios indicate that for a low illumination level on a horizontal track, $E_H = 1.4 \times 10^{-3}$ lux and meteorological visibility $S_M = 2.5$ km, the L_1/L_2 ratio is 13, while for $S_M = 20$ km, $L_1/L_2 = 8$.

This estimate convincingly demonstrates the considerable advantage of photonic sensor arrays with cut-off wavelength λ_c of approximately $1.8 - 2.0$ µm for night vision devices. Meanwhile, the manufacture of these devices all over the world is currently based on vacuum electrical to optical converters operating in the range of $0.4 - 0.9$ µm.

The solid-state photonic sensors with cut-off wavelength $\lambda_c \approx 1.8$ µm are now largely manufactured using semiconductor solid solutions In$_{053}$Ga$_{047}$As as epitaxial layers grown on InP substrates for which there exist a technique for the fabrication of photodiodes with a photosensitive element pitch of $12 - 15$ µm and an assembly technique with signal readout and processing integrated circuits made of silicon by means of indium bumps.[11, 12, 48, 49] Due to the active optical absorption of visible light, the InP substrate restricts the short-wavelength cut-off to approximately $\lambda \approx 0.9$ µm. In order to extend the photosensitivity range to the visible part of the spectrum, various methods are used for thinning or eliminating the InP substrate.[62 – 64] This may provide a photosensor quantum efficiency of approximately 60% at $\lambda = 0.5$ µm.[64] In recent years, considerable progress was also attained in the development of methods for reducing the pixel pitch for InGaAs-based photodiode arrays by switching from the indium bumps to copper-based planar microcontacts (cupper-to-copper microcontacts), the basic diagram for which is shown in Fig. 7.[48, 64 – 68] However, this type of hybridization does not eliminate the above-noted drawbacks of photosensor arrays based on 3D materials, related to the necessity to use highly precise and expensive equipment and high labour consumption, resulting in high cost of products.

3. Photonic sensor arrays for the near- and short-wave spectral regions based on colloidal quantum dots

Quite a few recent publications are devoted to the design of photosensitive elements operating in the near and short-wave IR regions using CQD-based low-dimensional structures.[69 – 74] The use of CQD-based structures as the element base of photosensorics provides a number of characteristics that are of fundamental importance for the key technology of photodetector arrays. The most significant of these characteristics are the following:

— CQD-based arrays are completely free from In or Cu metal microcontacts, usually utilized for connecting the photodiode arrays to silicon multiplexers; CQD-based photosensitive layers can be formed by spin-coating, jet or aerosol printing at moderate temperatures directly on the surface of input devices of silicon ROIC (Fig. 8);[75]

— currently, there are mega-pixel (2.1 MP) CQD PbS array formats amounting to 1920×1080 at a 15 µm pitch;[76] however, the pixel pitch and format are restricted only by those of the silicon multiplexor; therefore, the fabrication of supermega-pixel devices is possible in the future;

V.P.Ponomarenko, V.S.Popov, I.A.Shuklov, V.V.Ivanov, V.F.Razumov
Russ. Chem. Rev., 2024, **93** (4) RCR5113

7 of 48
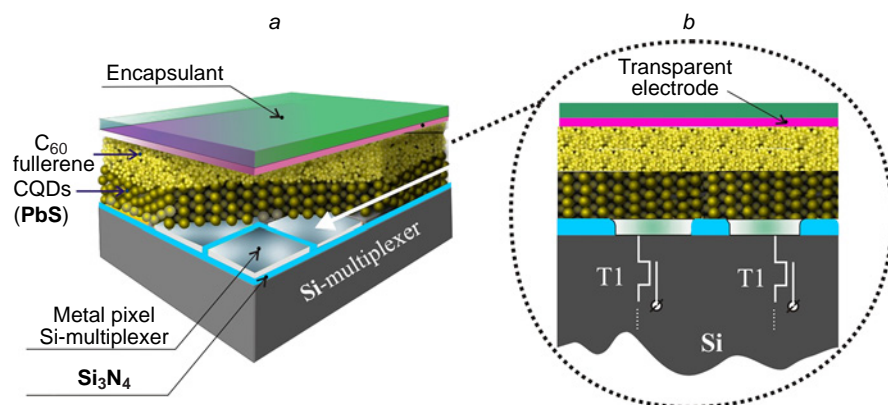
Figure 8. Diagram of integration of photo-sensitive element array based on CQD barrier structure to Si ROIC with the *top contact/ C60/CQD PbS/bottom contact* architecture: (*a*) photodiode array hybridized with Si ROIC; (*b*) two C60/CQD elements electrically connected to the input devices of ROIC (T1 transistor sources). The energy barrier is formed at the *C60/PbS CQD* contact. The Figure was created by the authors using published data.[75,88]

— the two smallest pixel pitches known for SWIR sensors (1.62 and 1.82 µm) were implemented in ROIC used with CQD-based photodiodes in which there are no limitations related to the minimum size of indium bumps;[77,78]
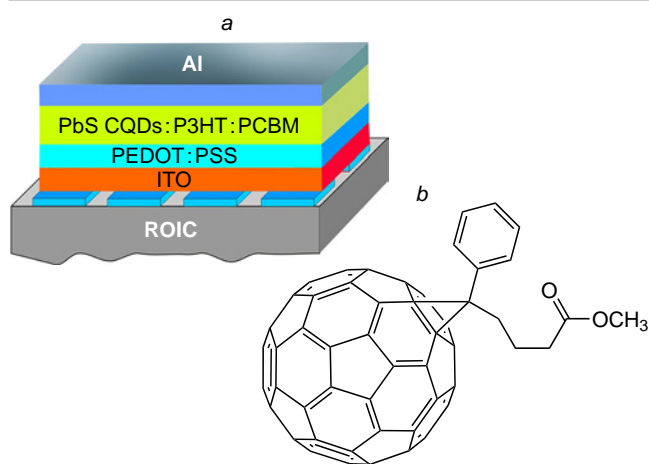
— a 640×512 array based on HgTe CQDs with a pitch of 15 µm for the SWIR spectral range is markedly less expensive than the same array based on the epitaxial InGaAs heterostructure;[32]

— wide range of spectral sensitivity $S_\lambda(\lambda)$ of PbS nanocrystal; furthermore, the right edge of $S_\lambda(\lambda)$ dependence can be controlled by varying the quantum dot size *via* variation of conditions of CQD synthesis.[69,79]

The first attempts of using PbS nanocrystals as quantum dots for recording electromagnetic radiation in the wavelength range of $0.975-1.3$ µm were undertaken in 2004 and reported by McDonald *et al.*[80]

The authors[80] described photoresistors in which PbS nanocrystals distributed throughout the MEH-PPV polymer served as the photosensitive medium. The photoconductivity spectra of the *MEH-PPV:PbS CQD* nanocomposites for variable PbS CQD size showed maxima at 0.98, 1.2 and 1.355 µm wavelengths. The photosensitive layer was deposited on an electrode coated by indium tin oxide (ITO). McDonald *et al.*[81] described the first photodiode with the *ITO/PPV/ PbS CQD:MEH-PPV/Mg* architecture. In 2009, McDonald *et al.*[82] described the architecture of a photosensitive element

obtained by deposition of 256×256 pixel array on Si ROIC from a solution. The photosensitive element consisted of photodiodes based on bulk heterojunctions produced by mixing PbS colloidal quantum dots with two organic compounds, poly(3-hexylthiophene-2,5-diyl) (P3HT) and phenyl-C61-butyric acid

Structure of MEH-PPV

Structure of P3HT

Structure of PEDOT:PSS

Figure 9. (*a*) Architecture of a photosensitive element based on the *PbS CQD:P3HT:PCBM* bulk heterojunctions; (*b*) structure of PCBM (phenyl-C61-butyric acid methyl ester).[82]

Figure 10. Photosensitive element with an energy barrier at the *PbS CQD/fullerene C60* contact: (*a*) architecture of a photosensitive element of 1 mm in diameter; (*b*) energy diagram; (*c*) current–voltag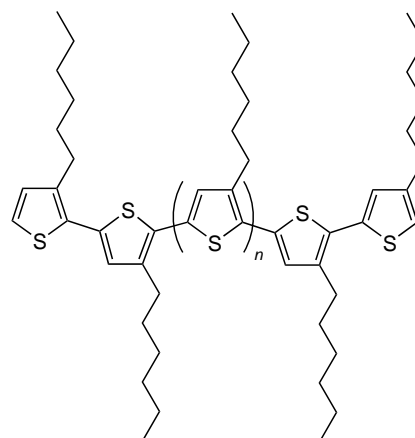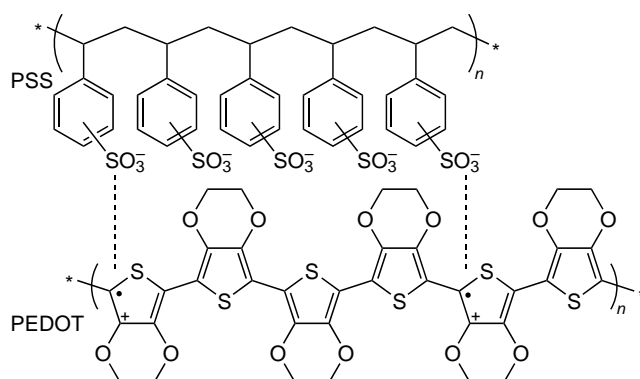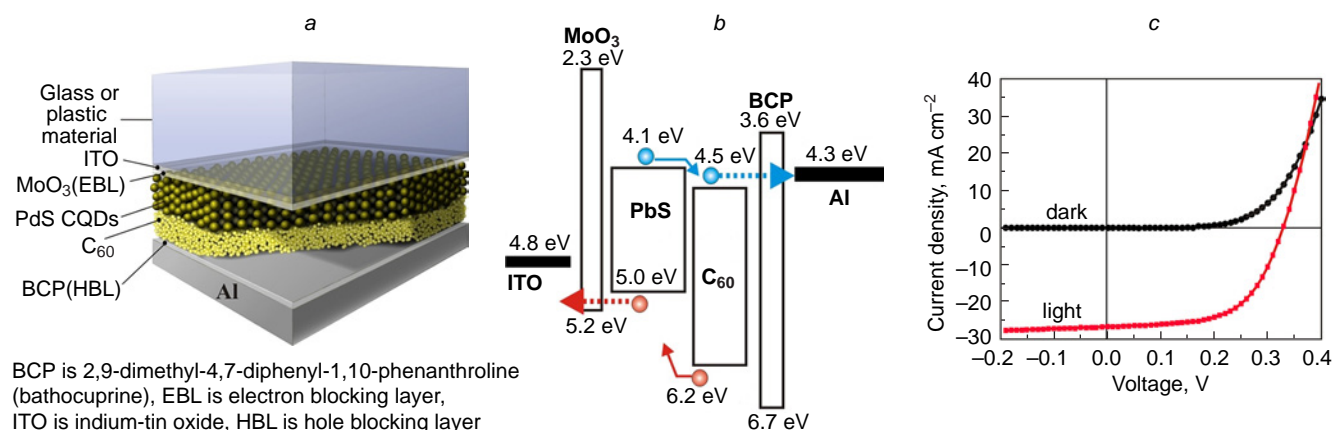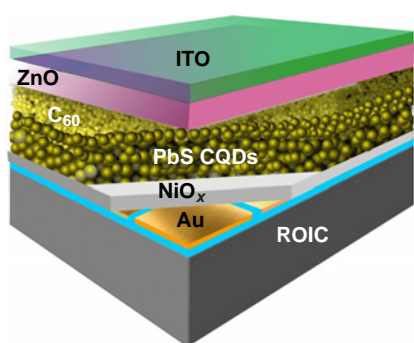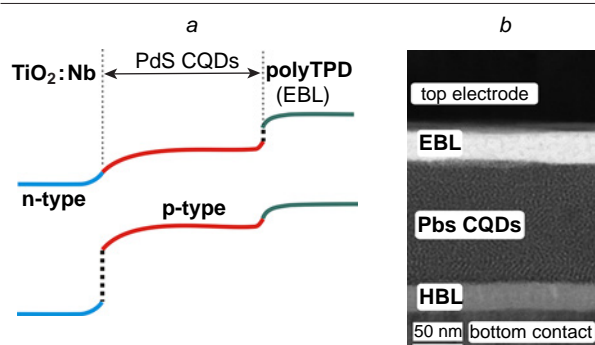e characteristic of the structure: in the dark (dark) and under illumination (light) from a source with a spectral composition and power of 100 mW×cm⁻² corresponding to solar radiation.[75,83–89]

Figure 11. Architecture of a 640×512 photosensor array with a 15 μm pitch based on PbS CQDs.

methyl ester (PCBM) (Fig. 9).[82] A better contact between the photosensitive layer and the ITO electrode was attained by using an interlayer based on the poly(3,4-ethylenedioxythiophene) (PEDOT):poly(styrene sulfonic acid) (PSS) composite. Since then, lead sulfide colloidal quantum dots have been recognized as one of the most promising materials of IR photosensorics.

Lately, two architectures have been most popular for the development and fabrication of photodetector arrays based on PbS colloidal quantum dots, particularly, one using the energy barrier of the *PbS CQD/C60* heterojunction (Figs. 10, 11)[75,83–89] and one using the energy barrier across the *p-PbS CQDs/n-TiO2* contact (Fig. 12).[90–93] The former architecture was used to design 640×512, 1280×1024 and 1920×1080 photodiode arrays with an extended sensitivity range from 0.35 to 2.1 μm and photosensitive element pitch of 15 μm, which are commercially distributed.[76,83–89] The latter architecture was used to design image sensors with 640×480, 640×512 and 768×512 formats and a reduced pixel pitch of 5 μm.[90] Using this architecture, photodetectors with very small pixel pitches of 2.1 and 1.82 μm were studied.[34,91–93] A pixel pitch of 1.62 μm was attained for photosensitive elements based on PbS CQDs with microlenses and copper reflective coatings.[78]

The architecture of a single photosensitive element with a *PbS CQD/C60* heterojunction energy barrier is shown in Fig. 10*a*. This is a sequence of nanolayers ITO *(top contact)/ MoO3 (EBL)/PbS CQD/C60/BCP (HBL)/bottom contact* where MoO3 serves as the electron blocking layer (EBL). In the CQD and fullerene C60 layers, photons of electromagnetic radiation are absorbed, excitons appear and decay to give electron–hole pairs, which are separated at the boundary between PbS CQDs and C60. The electrons are transported through the C60 layer, pass through the hole blocking layer (HBL) and are collected by the aluminium bottom contact. 2,9-Dimethyl-4,7-diphenyl-1,10-phenanthroline [bathocuprine (BCP)] acts as HBL. Similarly, holes are transported through the PbS CQD layer, pass through the EBL layer and are collected at the indium tin oxide (ITO) (In2O3)0.9(SnO2)0.1 top contact. The energy diagram of this structure and the current–voltage characteristic (CVC) (in the dark and under illumination from a radiation source with a spectral composition corresponding to solar radiation) are shown in Figures 10 *b,c*. Good prospects of this architecture for photosensor arrays operating in near- and short-wave IR regions was noted in 2012.[75] A 640×512 format photosensor with a similar architecture was reported in 2022.[35] A 60 nm-thick NiOx nanolayer functioned as HBL, while a 150-nm ZnO layer served as EBL (see Fig. 11).[35]

The energy diagram of the photosensitive element with an energy barrier at the CQD, p-PbS and n-TiO2 contact is shown in Fig. 12. This is a sequence of nanolayers: *ITO (top contact)/ polyTPD (EBL)/PbS CQD/TiO2:Nb (HBL)/bottom contact*, where polyTPD [poly(4-butyl-*N,N*-diphenylaniline] serves as the electron-blocking layer, and TiO2 is a hole blocking layer. Silver and TiN layers can be used as the top (transparent) and bottom (non-transparent) contacts.[93] The HBL layer with electronic conductivity is fabricated by doping TiO2 with niobium.
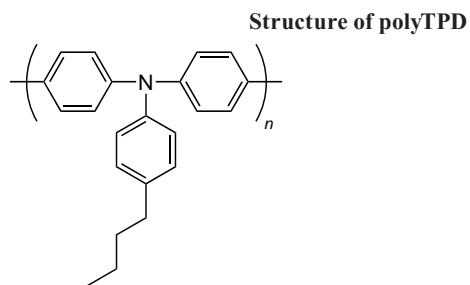

Figure 12. Energy diagram (*a*) and STEM image of the architecture (*b*) of the ITO *(top electrode)/polyTPD (EBL)/PbS CQDs/TiO2:Nb (HBL)/bottom electrode* photosensor.[93]

V.P.Ponomarenko, V.S.Popov, I.A.Shuklov, V.V.Ivanov, V.F.Razumov
Russ. Chem. Rev., 2024, **93** (4) RCR5113

9 of 48

Structure of polyTPD

A key characteristic of photosensors is the specific detectivity D^* (Table 1).[94] The B/BCP/C$_{60}$/PbS CQD/MoO$_3$/ITO photosensors (B is the non-transparent bottom contact) are characterized by the detectivity D^* of 1.0×10^{12} cm Hz$^{1/2}$ W^{-1} (20 °C, $\lambda = 1.4$ μm); as the sensor is cooled down to –20 °C, this value increases to 4.0×10^{12} cm Hz$^{1/2}$ W^{-1}. Figure 13 shows the spectral dependences of the responsivity (A W^{-1}) and the detectivity of a mega-pixel PbS CQD photosensor (1920×1080) with the long cut-off wavelength $\lambda_c = 1.9$ μm.[33, 76]

The key characteristics of the above-described photosensors based on PbS colloidal quantum dots are summarized in Table. 1.[35, 76, 77, 83–90]

In 2022, Gréboval *et al.*[32] described a HgTe CQD-based photosensor array using photoresistive architecture of photosensitive elements. The 640×512 array with a pixel pitch of 15 μm based on HgTe CQDs showed a cut-off wavelength $\lambda = 1.8$ μm and quantum efficiency of ~15%.[32]

In 2023, Luo *et al.*[95] described a 1280×1024 mega-pixel photodetector based on HgTe CQD photoresistors (15 μm pitch) with a cut-off wavelength of 2.0 μm, responsivity of 0.23 A W^{-1} and quantum efficiency of ~14% at room temperature.[95] The search for new elements for sensor arrays based on low-dimensional structures and ways to improve
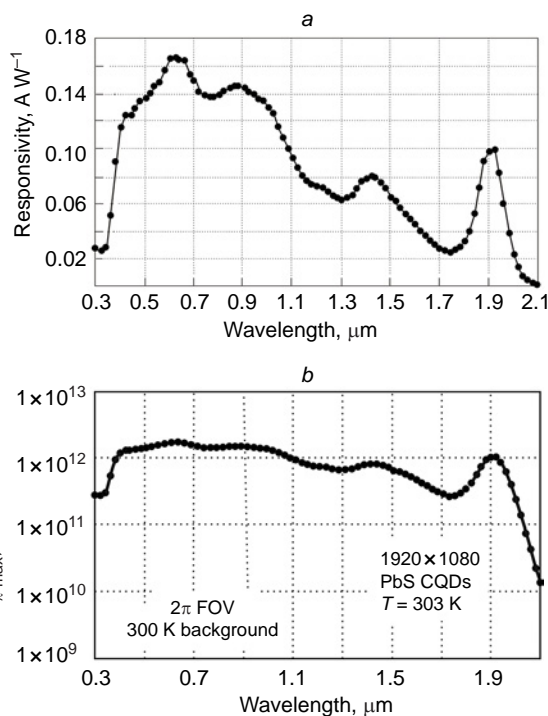
Figure 13. Spectral dependences of the responsivity and (*a*) and specific detectivity (*b*) of a 1920×1080 photosensor array (15 μm pixel pitch).[76]

them has been intensively carried out in recent years as well.[96–103]

A 388×288 array with the PbS CQD-based photosensitive layer and readout circuit was studied by S.Goossens *et al.*[104]

Table 1. Architectures and basic properties of photodetectors based on lead sulfide colloidal quantum dot (PbS CQD) photodiode arrays.[35, 76, 77, 83–90]

Format M × N	Pixel ptch, μm	Architecture	Layer thickness, nm				I_{dark}, A см$^{-2}$	D^*, cm Hz$^{1/2}$ W^{-1} (Jones)	Sensitivity-range, μm	Quantum efficiency (%)	Position of the 1st exciton peak, μm	Ref.
			d_{EBL}	$d_{C_{60}}$	d_{HTL}	d_{PbS}						
1920×1080 1280×1024 640×512	15	*B/BCP/C$_{60}$/ KKT PbS/ MoO$_3$/ITO*	–	–	–	~100	$1.3 \cdot 10^{-7}$ (293 K) ($V = -25$ мВ)	$1 \cdot 10^{12}$ (20 °C, 1.4 μm) $4 \cdot 10^{12}$ (–20 °C, 1.4 μm)	0.35–2.1 0.4–1.65	~15 (1.5 μm) ~60 (0.54 μm)	1.9	76, 83–89
768×512	5	*B/TiO$_2$/KKT PbS/ PolyTPD/T*	–	–	–	~100	3.3×10^{-6}	–	0.4–1.6	~70 (vis) ~40 (1 μm)	1.45	90
640×512	15	*B/NiOx/KKT PbS/ C$_{60}$/ZnO/T*	150	15	60	~600	17.8×10^{-9}	$2.1 \cdot 10^{12}$ (1.1 μm)	0.4–1.3	~90 (0.46 μm) ~63 (0.96 μm)	0.97	35
640×480 128×128 128×128	5 2.1 1.82	*B/HBL//KKT PbS/ EBL/T*	–	–	–	600	3×10^{-7} 1.5×10^{-7} 2.0×10^{-7}		0.4–1.4	~35 (0.43 μm) ~13 (1.4 μm)	1.4	77

Notes. B is non-transparent bottom contact; T is transparent top contact; HBL is hole blocking layer; EBL is electron blocking layer; C$_{60}$ is fullerene; ITO is indium tin oxide (In$_2$O$_3$)$_{0.9}$(SnO$_2$)$_{0.1}$; polyTPD is poly(4-butyl-*N,N*-diphenylaniline); BCP is 2,9-dimethyl-4,7-di-phenyl-1,10-phenanthroline; D^* is specific detectivity; I_{dark} is the dark current;

$D^* = \dfrac{S_i}{i_n}(A\Delta f)^{1/2}$, where $S_i = \dfrac{dI}{dP}$ is the responsivity (I is the current in the photodetector circuit arising under the action of radiation with power P), i_n is the root-mean-square noise, A is the detector area, Δf is the amplifier bandwidth.[94]

10 of 48

V.P.Ponomarenko, V.S.Popov, I.A.Shuklov, V.V.Ivanov, V.F.Razumov
Russ. Chem. Rev., 2024, **93** (4) RCR5113

The sensor sensitivity and detectivity were $0.3-1.0\ \mu m$ and $10^{12}\ cm\ Hz^{1/2}\ W^{-1}$, respectively.

4. Electrophysical properties of CQDs and layers based on them

4.1. Electronic structure of CQDs

Colloidal quantum dots are commonly defined as crystalline inorganic particles with a nearly spherical shape and radius R ranging from ~1 to ~25 nm containing hundreds to thousands of atoms. A quantum dot is larger than a molecular cluster, typically containing 10 to 100 atoms and having ~1 nm in size.

Bulk (3D) binary compounds PbS, PbSe and PbTe crystallize in the face-centred cubic lattice of rock salt NaCl (space group O_h^5-$Fm3m$), which has four atoms in the unit cell.[105] At high pressure, they undergo a polytype transition to a crystal lattice with space group D_{2h}^{16}-$Pnma$. The energy band structures of lead salts PbS, PbSe and PbTe are very similar. Their Brillouin zones are the same as that of Group A^{IV} elemental semiconductors. In the lead chalcogenides PbS, PbSe and PbTe with cubic symmetry (O_h point group of symmetry), the first Brillouin zone has a system of eight semi-ellipsoids of equal energy, the symmetry axes of which coincide with the [111] directions. The centres of ellipsoids are located on the hexagonal faces of the Brillouin zone. Therefore, the full constant-energy surface in the first Brillouin zone is formed by four ellipsoids ($N = 4$), each consisting of two half-ellipsoids on the opposite faces of the Brillouin zone. The chemical bonding in compounds $A^{IV}B^{VI}$ is fairly complex and includes three components: covalent, ionic and metallic bonds. The considered lead salts are direct-band-gap semiconductors (the band gaps for bulk PbS, PbSe and PbTe are 0.42, 0.278 and 0.311 eV, respectively). However, unlike binary $A^{III}B^V$ semiconductors (InAs, GaAs and other), in PbS, PbSe and PbTe, conduction and valence band extrema are located at the L rather than Γ point of the Brillouin zone. In lead salts, the conduction and valence bands are highly non-parabolic. The band gap width has a positive temperature coefficient. The effective masses of electrons and holes differ little. The excess Pb atoms behave as shallow donors, whereas Te, S and Se are acceptors with a very low activation energy. This brings about certain difficulties for the preparation of stoichiometric compositions in these crystals.

At thermodynamic equilibrium, bulk (3D) binary compounds $A^{II}B^{VI}$ crystallize in the cubic sphalerite structure (space group T_d^2-$F\bar{4}3m$) and hexagonal wurtzite structure (space group C_{6v}^4-$P6_3mc$). An exception is mercury sulfide HgS, which may exist not only as the cubic β-polymorph but also as the α-polymorph (space group $P3_121$).[106]

Mercury telluride HgTe is a semimetal with a zero band gap and an *inverted* band structure. The Brillouin zone of mercury telluride HgTe has the same structure as that of cadmium telluride CdTe. However, the Γ_6 state is much lower in HgTe than in CdTe. As a result, after spin−orbit coupling, the Γ_6 state is located below Γ_8. This is accompanied by band inversion: the curvature of Γ_6 and Γ_8 states changes the sign in HgTe with respect to CdTe, the Γ_6 state now forms the light-hole band E_{v2}, while Γ_8 forms the conduction band E_c. The Γ_8 state is still degenerate, but now the heavy-hole band E_{v1} and the conduction band E_c are converged in this state. This gives rise to a zero-band-gap semiconductor. The value $E_{\Gamma g} = E_{\Gamma 6} - E_{\Gamma 8}$, which is *negative*, unlike that in CdTe, is referred to as negative band gap. It is not a band gap in the general meaning accepted in semiconductor physics, but only emphasizes the interaction

between E_c and E_{v2}. In the case of HgTe at point $\mathbf{k} = 0$, the heavy-hole band and the conduction band are degenerate. Due to the relatively large effective mass of heavy holes, the maximum of the heavy hole band splits and shifts from the point $\mathbf{k} = 0$. This shift gives rise to some overlap ΔE between E_c and E_{v1}. This overlap is small, being approximately $1.0-1.5$ meV.[106] It is maximum along the [111] direction. The presence of overlap, although slight, allows mercury telluride to be classified as a semimetal. Due to the zero band gap, the temperature dependence of the intrinsic concentration of charge carriers in HgTe is a power $(n_i \sim T^{3/2})$ rather than activation $[n_i \sim \exp(-E_g/kT)]$ function. A similar band structure is inherent in mercury selenide. The binary compound β-HgS has a minor energy gap near the Γ point of the Brillouin zone, equal approximately to -0.15 eV, caused by the spin−orbit coupling; therefore, mercury sulfide should rather be *classified* as a semiconductor and not a semimetal. The Kane model developed for the description of non-parabolic zones in indium antimonide InSb is fully applicable to HgSe and HgTe. Near the conduction band minimum, the dependences E_c ($\mathbf{k} = 0$) without taking into account more remote bands in HgSe and HgTe are parabolic, that is, $E \sim |\mathbf{k}|^2$. As the $\mathbf{k}$ value increases, the conduction bands become non-parabolic: their curvature decreases and the effective mass of electrons increases. The heavy hole band in HgTe is usually described with the assumption that it looks similarly to that in InSb. In this case, the constant-energy surfaces are ellipsoids arranged along the $\langle 111 \rangle$ axes. Since 2016, HgSe and HgTe have been considered as Weil semimetals.[107]

Considering physical characteristics, a quantum dot can be regarded as both a quasi-zero-dimensional nanocrystal and a large inorganic molecule. This defines different theoretical approaches to the development of physical models and calculations of the energy structures of CQDs.[20−23]

According to the former approach, which is conventionally called bottom-up, a quantum dot is represented as a multiatomic molecule with a set of electron orbitals (discrete levels). The energy structure of a quantum dot is built *via* successive addition of single atoms to the basic particle. As computing power increased, this approach, initially applicable to quantum dots composed of a small number of atoms, became more important and started to be used to calculate the energy structure for dots consisting of hundreds of atoms.

According to the latter approach, conventionally called the top−down approach, a quantum dot is considered as a semiconductor nanocrystal with a characteristic radius R, which meets the condition $a_0 < R < \lambda_{DB}$, where a_0 is the crystal lattice parameter, λ_{DB} is the de Broglie wavelength of a particle in the bulk semiconductor crystal. This approach allows the use of a model well developed in quantum mechanics that describes the wave functions of a particle in a spherical potential well with infinitely high wall. For an electron−hole pair, the movement of which is confined by a spherical quantum dot, the size quantization is characterized by the effective exciton Bohr radius a_B^* equal to $a_B^* = \hbar^2 \varepsilon / m^* e^2$ [ε is the dielectric permittivity of the nanocrystal material, $(m^*)^{-1} = (m_e^*)^{-1} + (m_h^*)^{-1}$ is the reduced effective exciton mass, m_h^* are the electron and hole effective masses, respectively]. If $R/a_B^* > 4$, then a weak, or exciton, confinement regime is implemented; this means that an electron−hole pair behaves as an exciton in which the motion of the centre of mass is quantized due to the confinement. If $R/a_B^* > 2$, a strong, or individual, confinement regime is implemented. In this case, the kinetic movements of electrons and holes are quantized separately, and there is a clear-cut

V.P.Ponomarenko, V.S.Popov, I.A.Shuklov, V.V.Ivanov, V.F.Razumov
Russ. Chem. Rev., 2024, **93** (4) RCR5113

11 of 48

discretization of energy levels, on the one hand, and a shift of the optical absorption lines depending on the quantum dot radius, on the other hand. The electron and hole interaction with a spatially confined nanocrystal significantly exceeds their Coulomb interaction, which, in this case, can be considered as a small perturbation.

The theory first proposed by Al.A.Efros and A.L.Efros to explain the observed absorption features of CuCl CQDs was initially based on the standard band structure of the direct band gap semiconductor with a parabolic law of dispersion of the valence and conduction bands near $\mathbf{k} = 0$ with the assumption that other linear dimensions of the semiconductor are greater than the lattice constant.[20] This theory, based on the effective mass model and currently recognized as the main one, served as the foundation for all subsequent studies of the optical transitions in semiconductor nanocrystals.[21,108–112] According to this theory, the shift of the band gap energy ΔE_g caused by exciton confinement in the quantum dot with the radius R based on a direct band gap semiconductor with the dispersion law $E = \hbar^2 k^2 / 2m^*$ can be described by the expression

$$\Delta E_g = \frac{\hbar^2 \pi^2}{2R^2}\left(\frac{1}{m_e^*} + \frac{1}{m_h^*}\right) - \frac{1.786\,e^2}{\varepsilon R} - 0.248\,E_{Ry}^* \qquad (2)$$

where $E_{Ry}^* = e^4/2\varepsilon^2\hbar^2[(m_e^*)^{-1} + (m_h^*)^{-1}]$ is the effective Rydberg constant expressed in energy units; the first term is the confinement energy, proportional to R^{-2}, the second term shows the Coulomb interaction energy ($\sim R^{-1}$), and the last term does not depend on R and is usually negligibly small, except that for semiconductors with a low dielectric permittivity.[20,21,108,109] It can be seen from expression (2) that the energy of the first optical exciton transition (that is, the band gap) increases with decreasing quantum dot radius. The allowed energy levels of electrons $E_{n_e\ell_e}$ and holes $E_{n_h\ell_h}$ are derived from solution of the steady-state Schrödinger equation:[20]

$$E_{n_e\ell_e} = \frac{\hbar^2 \rho_{n_e\ell_e}}{2m_e^* R^2} \qquad (3)$$

$$E_{n_h\ell_h} = \frac{\hbar^2 \rho_{n_h\ell_h}}{2m_h^* R^2}$$

where n_e and n_h are electron and hole principal quantum numbers; ℓ_e and ℓ_h are electron and hole orbital quantum numbers; $\rho_{n_e\ell_e}$ and $\rho_{n_h\ell_h}$ are sets of values determined by the roots of the spherical Bessel functions, which *appear in the* solution of the Schrödinger equation.

The studies of *optical absorption*, luminescence, *etc.* in various quantum dot structures carried out in 1998–2016 confirmed the theoretical views about the energy structure of quantum dots that describe weak and strong confinement in terms of the effective mass model and the parabolic dispersion law for the valence and conduction bands.[112–117] The case of intermediate confinement ($2a_B^* < R < 4a_B^*$) in quantum dots has also been studied.[108,109,114] In this case, as was shown in 1982, the $1S_h \rightarrow 1S_e$, $1P_h \rightarrow 1P_e$, $1D_h \rightarrow 1D_e$ and the like transitions are dipole allowed optical transitions the relative intensity of which is determined by the squared overlap integral of the electron $\psi_e(\mathbf{r})$ and hole $\psi_h(\mathbf{r})$ wave functions ($\mathbf{r}$ is radius vector), which is given by $|\int \psi_e(\mathbf{r})\psi_h(\mathbf{r})d^3\mathbf{r}|^2$ (Fig. 14a).[20] However, in 1987, significant discrepancies were noted between the theoretical and experimental band gaps and PbS CQD sizes (Fig. 14b);[110,118] they were explained considering the effect of the band structure details, including band anisotropy, deviations from the parabolic dispersion law, effect of degeneracy, complex valence band structure, *etc.*; this resulted in construction of an experimentally confirmed picture of optical processes in quantum dot structures formed by direct band gap binary semiconductors based on Group II, IV and VI elements.[118–126]

For the case of strong confinement in CdSe nanocrystals, inclusion of the effect of the Kane shape of the conduction band, degeneracy of the valence band consisting of light and heavy hole bands and split off band (Scheme 1) resulted in the energy structure shown in Fig. 15a.[111,127] In this case, the allowed optical transitions of noticeable intensity were as follows: $1S_{3/2}(h) \rightarrow 1S_e$, $2S_{3/2}(h) \rightarrow 1S_e$, $1S_{1/2}(h) \rightarrow 1S_e$, $2S_{1/2}(h) \rightarrow 1S_e$, $1P_{1/2}(h) \rightarrow 1P_e$, $3S_{1/2}(h) \rightarrow 1S_e$, $2S_{3/2}(h) \rightarrow 2S_e$, $1P_{1/2}^{so}(h) \rightarrow 1P_e$ and $4S_{3/2}(h) \rightarrow 2S_e$. The energy level diagram in semiconductor quantum dots based on direct band gap semiconductors is shown in Scheme 1, in which *SfSt* stands for the surface level (trap).[127]

In recent years, increasing attention has been paid to quantum dot structures based on indirect band gap semiconductors consisting of silicon, germanium, oxygen, hydrogen and carbon as they are less toxic than heavy elements such as Pb, Hg, Cd, *etc.* and, hence, suitable for medical applications. There is still no full understanding of the energy

Scheme 1
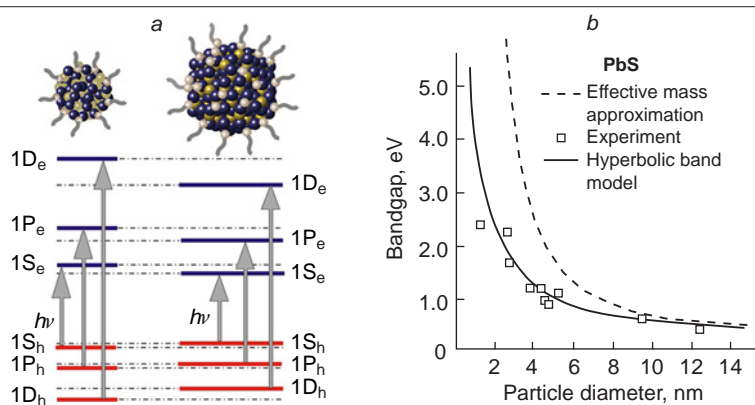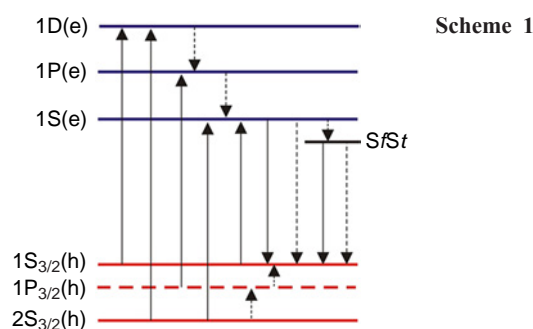
Figure 14. (a) Allowed optical transitions according to the theory based on effective mass approximation and the parabolic band dispersion law for PbS CQDs of various diameters; (b) band gap for PbS CQD array *vs.* CQD diameter (the continuous line corresponds to calculations considering the hyperbolic nature of the valence and conduction bands). The Figure was created by the authors using published data.[20,110,118]

12 of 48

V.P.Ponomarenko, V.S.Popov, I.A.Shuklov, V.V.Ivanov, V.F.Razumov
Russ. Chem. Rev., 2024, **93** (4) RCR5113
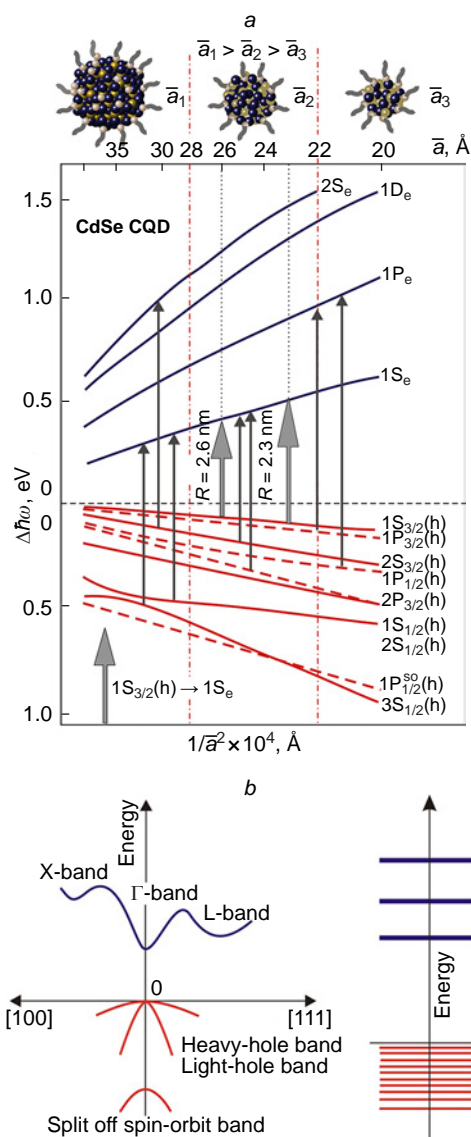
Figure 15. Energy level diagram for nanocrystals based on direct band gap semiconductors: (*a*) energy spectrum of electrons and holes depending on the squared average radius ($\bar{a}$) of CdSe CQDs;[111] (*b*) diagram of allowed energy transitions. The vertical dashed lines are non-radiative transitions.[127]

structure and mechanisms of radiative and non-radiative transitions in quantum dots.

Nevertheless, relying on the certain analogy between the luminescent properties of complex organic molecules in the condensed phase and the properties of quantum dot-based luminophores, an energy diagram for CQDs based on indirect band gap semiconductors has been proposed (Fig. 16); the diagram consists of the singlet ground state (S_0), first excited singlet state (S_1) and metastable triplet state (T_1).[104, 127] The transition between the T_1 and S_1 states is forbidden by the spin selection rules. There are also high-lying singlet excited S_n ($n > 1$) and triplet T_n ($n > 1$) states. This diagram adequately describes the photophysical properties of quantum dot structures composed of indirect band gap semiconductors.[127]

It is noteworthy that, unlike 2D-structures for photodetectors (*e.g.*, QWIP, that is, numerous quantum wells grown by epitaxy), in which additional diffraction gratings, corrugated surfaces, island networks and so on must be used since optical transitions polarized in the photosensitive element (PSE) plane are
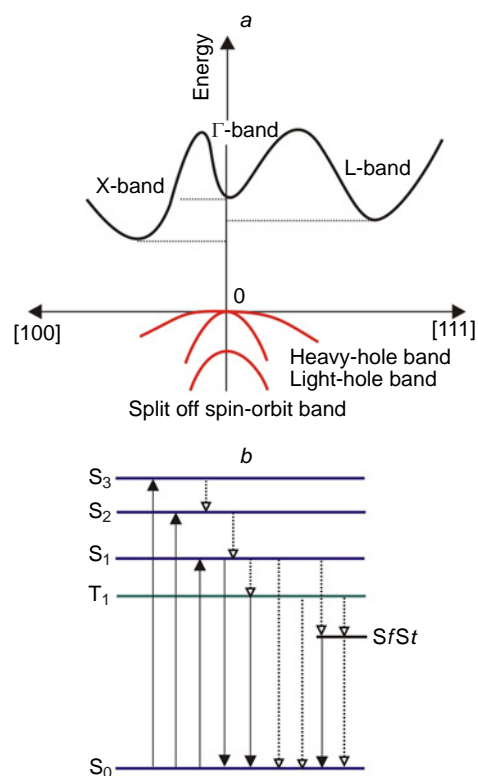
Figure 16. Diagram of energy levels in indirect band gap semiconductor nanocrystals: (*a*) simplified energy diagram; (*b*) diagram[127] of the allowed energy transitions. The vertical dashed lines are non-radiative transitions.
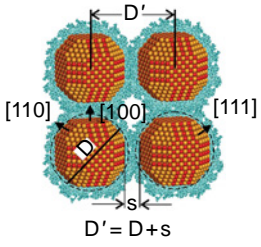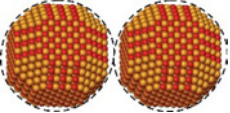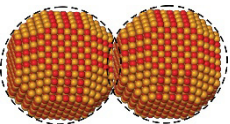
forbidden, in the case of quasi-0D quantum dot structures, the absorption of photons upon normal incidence on the PSE surface is possible, since the above forbidding is removed.[128] This markedly decreases the complexity of the photosensitive structure and simplifies the production process.

4.2. Charge transport in CQD arrays

To attain a high quantum efficiency of photosensors based on quantum dots, it is necessary to generate a high concentration of charge carriers in CQDs. For this purpose, CQD ensembles (arrays) with a layer density of $10^{11} - 10^{12}$ cm^{-2} rather than single quantum dots should be used. The above description of the optical properties is generally valid for both single quantum dots and arrays. The presence of organic (*e.g.*, oleic or mercaptopropionic acid residues, *etc.*) or inorganic ligands (*e.g.*, I$^-$, Cl$^-$ and so on) gives rise to only additional peaks (bands) in the absorption spectrum of the CQD array. However, analysis of the transport properties and charge transfer requires consideration of the whole set of nanocrystals that form the array. Although the properties of the array are still specified by the properties of constituent nanoparticles, the physical characteristics of the array may substantially differ from those of single CQDs. For example, a CQD array is characterized by a certain disorder, which is associated, in the simplest case, with different particle sizes and distances between the particles, different numbers of donors in each CQD, *etc*. As a result, the Fermi level position, dielectric permittivity, density of states and other characteristics may be considerably dissimilar for single quantum dots and for loose or dense CQD arrays.

Theoretical studies consider two types of structure for CQD arrays ordered to form a cubic lattice:[129–131]

V.P.Ponomarenko, V.S.Popov, I.A.Shuklov, V.V.Ivanov, V.F.Razumov
Russ. Chem. Rev., 2024, **93** (4) RCR5113

13 of 48

Table 2. Dielectric permittivity ε of a quantum dot array for different ratios between the dielectric permittivity of a single CQD (ε_{CQD}), the medium in which the CQDs are immersed (ε_i) and the volume fraction of CQDs in the array (f). The Table was composed by the authors using published data.[130, 131]

Type of CQD array structure	Ratio of ε_{CQD}, ε_i and f	Dielectric permittivity ε of CQD array
	Ligand-separated dots with size $D' \cong D \gg s$	
	if $\varepsilon_{CQD}/\varepsilon_i \cong 1$ any f	$\varepsilon_{1/3} = (1-f)\varepsilon_i^{1/3} + f\varepsilon_{CQD}^{1/3}$
	if $f \ll 1$ any $\varepsilon_{CQD}/\varepsilon_i$	$\varepsilon = \varepsilon_i + 3f\varepsilon_i(\varepsilon_{CQD}-\varepsilon_i)/(\varepsilon_{CQD} + 2\varepsilon_i)$
	Ligand-free dots that touch one another ($f \cong \pi/6$), $s > 0$	
	if $\varepsilon_{CQD}/\varepsilon_i \gg 1$	$\varepsilon = \dfrac{\pi}{2}\varepsilon_i[D/(2s + 2\delta)]^{1/3}$, where $\delta = 0.8\,D(\varepsilon_i/\varepsilon_{CQD})^{6/5}$
	Ligand-free dots that touch one another along their facets ($f \cong \pi/6$), $s < 0$	
	if $\varepsilon_{CQD}/\varepsilon_i \gg 1$	$\varepsilon = \varepsilon_{CQD}[2(|d| + \delta)/D]^{1/2}$ where $\delta = 0.8\,D(\varepsilon_i/\varepsilon_{CQD})^{6/5}$

(a) an array in which quantum dots are located at some distances from one another owing to ligands;

(b) quantum dots of the same size, but without ligands, which therefore touch one other with their faces.

Depending on the ratio between the dielectric permittivity values of single colloidal quantum dots (ε_{CQD}) and the medium in which the CQD array is immersed (ε_i) and the volume fraction f of quantum dots in the array, the dielectric permittivity of the array ε is calculated by the relations presented in Table 2,[130–131] which considerably differ from the Maxwell–Garnett and Bruggeman equations derived in the framework of mean-field theory.[129]

The specific features of charge carrier transport across single quantum dots are related to the limited number of electrons located in the CQD energy level. When a quantum dot occurring in an electric field is located between two thin potential barriers, only charge carriers with a definite energy can be involved in the tunnelling current across the dot. If the tunnelling permeabilities of the barriers are different, electrons start to accumulate in the quantum dot and suppress the carrier transport across CQD due to their Coulomb potential (Coulomb blockade). Hence, an additional electron can be added to a CQD only provided that the energy of this electron is high enough to overcome the Coulomb blockade. In semiconductor CQDs, the kinetic energy of electrons is quantized due to the quantum confinement effect, and the quantization energy may far exceed the Coulomb blockade energy.

A theoretical description of the conduction mechanisms in quantum dot arrays was given by Reich.[131] Due to the Coulomb blockade effect noted above, the conductivity in an array of even metallic quantum dots decreases exponentially with temperature, *i.e.*, such an array is usually a dielectric. Similarly, arrays of semiconductor quantum dots, including doped ones, are dielectrics, the conductivity of which is described by the formula [131]

$$G \propto \exp\left[-\left(\frac{E_0}{kT}\right)^p\right] \qquad (4)$$

in which coefficients E_0 and p depend on the conduction mechanism and temperature range.

The conduction mechanism in an array of doped quantum dots at low temperature usually corresponds to the Efros–Shklovskii model ($\ln G \propto T^{-1/2}$), the activation conduction mechanism ($\ln G \propto T^{-1}$) operates at high temperature, while in the intermediate temperature range, Mott transport is implemented ($\ln G \propto T^{-1/4}$).[132] For example, the Mott conduction mechanism is clearly manifested for CdSe CQDs in the 40–230 K temperature range (Fig. 17a).[133]

Figures 17b,c present the temperature dependences of the conductivity in PbS CQD arrays.[134] In the temperature range of 25–220 K, two clear-cut activation conduction regions are observed (Fig. 17b). In the (G, $T^{-0.25}$) coordinates, the temperature dependence is less obvious (Fig. 17c) and does not unambiguously attest to Mott conduction. The charge carrier transport in colloidal quantum dot arrays is addressed in a number of reviews.[131, 135–137] As opposed to metal nanoparticles, semiconductor CQDs are markedly affected by the quantum confinement, which accounts for a significant difference between the metal nanoparticle and semiconductor CQD arrays.[135] In the semiconductor CQD arrays, the disorder in the number of donors may lead to different numbers of electrons at different points. The effects of size, distance and donor number disorders on the conductivity of CQD arrays are considered in a review by Reich.[131]

Organic semiconductors are characterized by strong disorder and weak interaction between molecules, which determines the hopping mechanism of charge carrier transport.[138] The same features of disorder associated with the scatter in size, number of donors and distances between the centres of nanocrystals are also characteristic of CQD arrays.[131] Therefore, charge carrier transport in CQD arrays can also occur *via* hopping between localized energy states of various nanocrystals.[137]

14 of 48

V.P.Ponomarenko, V.S.Popov, I.A.Shuklov, V.V.Ivanov, V.F.Razumov
Russ. Chem. Rev., 2024, **93** (4) RCR5113
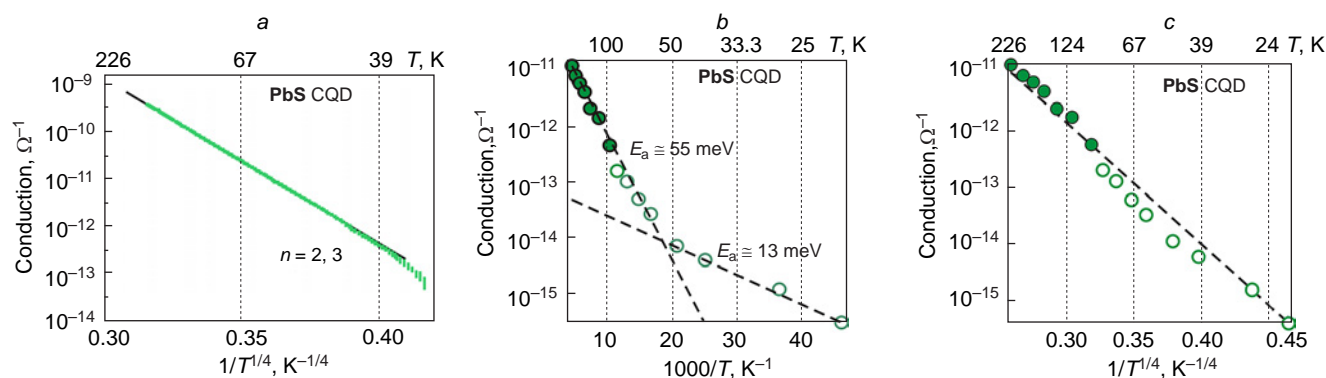
Figure 17. Temperature dependences of the conductivit G of colloidal quantum dot arrays: (*a*) CdSe CQDs in the $G-1/T^{1/4}$ coordinates;[131,133] and PbS CQDs in the (*b*) $G-1000/T$ and (*c*) $G-1/T^{1/4}$ coordinates.[134]
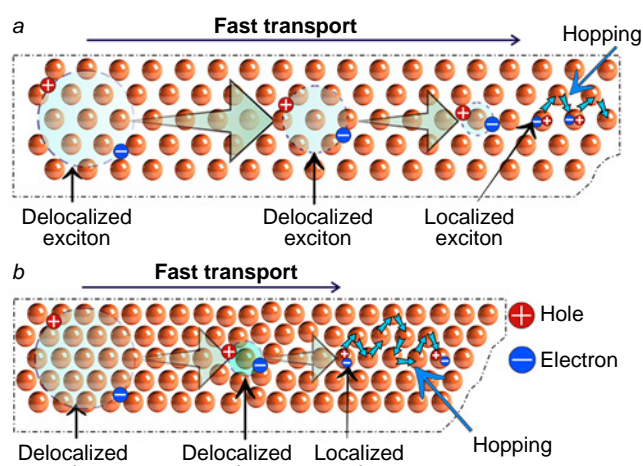
Figure 18. Exciton transport in CQD layers with: (*a*) relatively long distance between quantum dots; (*b*) relatively short distance between CQDs.[139]

The dynamics of intrinsic exciton diffusion in PbS CQDs was investigated by Zhang *et al.*[139] The authors observed a high exciton diffusion rate ($\sim 10^2$ cm^2 s^{-1}) in PbS CQDs during the first several hundred femtoseconds after photoexcitation followed by relatively slow transport ($\sim 10^{-1}$ cm^2 s^{-1}). The authors attributed this fast transport to the large exciton Bohr radius, which is significantly larger than the CQD diameter. Layers with greater distances between CQDs have a higher initial diffusion rate and later transition to the slower transport stage (Fig. 18).[139]

5. Single- and few-element photosensors based on CQDs

5.1. CQD materials for photosensors

Currently, colloidal quantum dots have been synthesized using quite a few semiconductors such as Si, graphite, graphene, ZnO, CdS, CdSe, CdTe, PbS, PbSe, PbTe, ZnSe, ZnS, ZnTe, Ag$_2$Se, Ag$_2$S, HgTe, HgS, HgSe, TiO$_2$, InAs, InP, InSb, GaAs, GaN, GaP, GaInP$_2$, CuInS$_2$, Cd$_x$Hg$_{1-x}$Te, Zn(Te$_{1-x}$Se$_x$), *etc.*

The development of high-temperature colloidal synthesis of quantum dots in 1993 opened prospects for the industrial production of a number of quasi-zero-dimensional materials with unusual and promising physical properties.[30]

To date, a number of architectures of photosensitive elements based on both photoresistors and energy barrier structures formed by heterojunctions or CQD layers with electron and hole types of conduction have been studied.[69,140,141] The greatest success in the design of devices that were implemented in the commercial market of optoelectronics was achieved with the use of PbS CQDs. Apart from the mega-pixel (2.1 MP) cameras demonstrated in 2020 at an exhibition in the USA, a broad-band device based on PbS CQDs with pulse response time of <3 ns was proposed in 2022.[36]

Colloidal quantum dots based on compounds of other elements, A^{IV}B^{VI} and A^{II}B^{VI}, are being actively studied. According to published data, the effective exciton Bohr radii in PbS, PbSe, PbTe, HgSe, HgTe and HgS are 18, 46, 150, 17, 40 and 50 nm, respectively.[142-145] The relatively large Bohr radius, together with the observed optical absorption (Fig. 19),[146-151] makes these compounds promising for the development of near- and mid-wave IR devices. The following analysis of the architectures of CQD-based photosensitive elements will focus on colloidal quantum dots of lead and mercury chalcogenides (PbS, PbSe, HgTe, HgSe, HgS), which were used to fabricate various types of sensor elements.

5.2. Photoresistors

The size quantization in binary compounds of Group IV–VI elements was observed for ultrathin PbS and PbTe CQDs layers obtained by vacuum evaporation back in 1960.[152] Lead sulfide quantum dots synthesized as $8-30$ nm nanocrystals inside a glass matrix by high-temperature heating of silicate glasses were described in 1994 by Borrelli and Smith.[153] In 2001, high-temperature colloidal synthesis of PbSe quantum dots was performed.[154] In 2003, a process for the fabrication of PbS-based colloidal quantum dots was described.[155] PbS and PbSe CQDs are self-assembled to ordered superlattices with high structure perfection and minimum size dispersion (<5%).[69]

The photoresistive structure studied by Hu *et al.*[156] was composed of a PbS CQD layer deposited onto interdigitated electrodes (Fig. 20). Protection from the atmosphere was provided by a 30 nm-thick Al$_2$O$_3$ coating fabricated by atomic layer deposition (ALD) technique. Photosensitivity cut-off wavelength of 2.4 µm, responsivity of approximately 50 A W^{-1} ($\lambda = 1.55$ µm) and detectivity of 3.4×10^8 cm Hz$^{1/2}$ W^{-1} at $T = 230$ K were implemented.

The presence of ligands and dangling bonds on the CQD surface and the presence of surface oxygen adsorbents (such as PbSO$_3$ PbSO$_4$) gives rise to acceptor states in the band gap and

V.P.Ponomarenko, V.S.Popov, I.A.Shuklov, V.V.Ivanov, V.F.Razumov
Russ. Chem. Rev., 2024, **93** (4) RCR5113

15 of 48
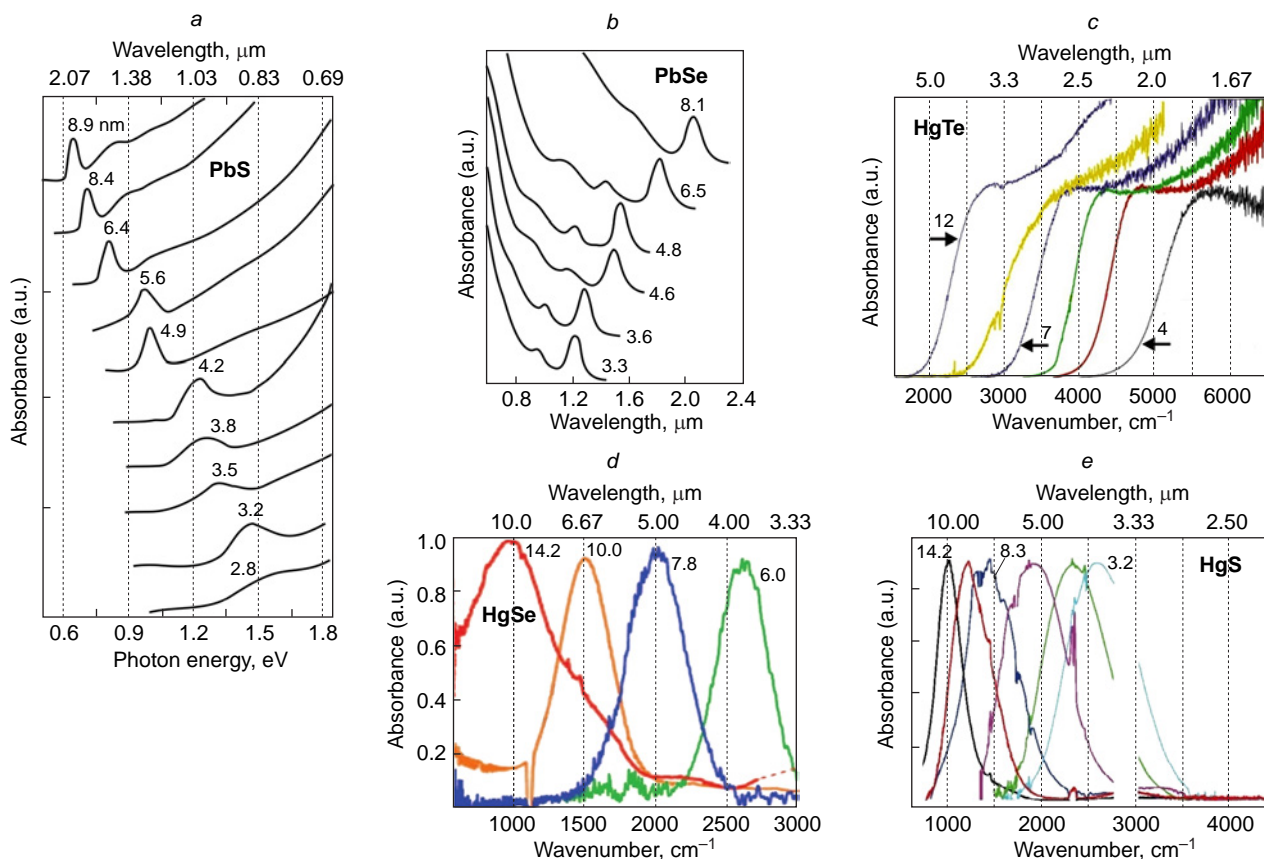
Figure 19. Spectral dependences of absorption in colloidal quantum dots of Group II, IV and VI elements: (a) PbS;[146] (b) PbSe;[147,151] (c) HgTe;[148] (d) HgSe;[149] (e) HgS;[150] the CQD diameter in nanometres is indicated near the curves.
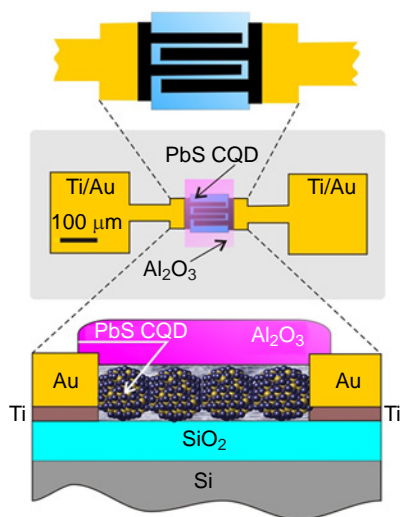
Figure 20. Photoresistive structure based on PbS CQDs with interdigitated finger electrodes. The Figure was created by the authors using published data.[156]

finally results in the switching of the initially n-type PbS CQD layer to hole conduction with a concentration of ~10^{17} cm^{-3}.[157] High concentration of the major charge carriers and the presence of traps for minor charge carriers in the band gap lead to high dark current density and low speed performance of photoresistors. Silver nanocrystals with low electron work function, being located in quantum dot layers near PbS nanocrystals, can act as a sort of donors by injecting electrons, which compensate the acceptor states and passivate the surface trap states. This is in sharp contrast to ionic doping, where replacement of lead cations gives rise to stronger p-type conduction in PbS nanocrystals. By mixing PbS CQDs and Ag nanocrystals in various ratios during the synthesis, the authors attained controlled doping of colloidal quantum dots where CQD layers switched to electronic conduction type.[157] The optimal PbS : Ag ratio was 1 : 0.05; in this case, $D^*_{\lambda=1.55} = 5 \times 10^{11}$ cm Hz$^{1/2}$ W^{-1} at $\lambda = 1.55$ µm and $D^*_{\lambda=0.6} = 1.2 \times 10^{12}$ cm Hz$^{1/2}$ W^{-1} at $\lambda = 0.6$ µm were attained (мкм надо заменить на µm). The frequency band amounted to 200 Hz. This method also leads to passivation of traps in the band gap. A CQD array can also be passivated by being coated with alumina.[157]

Organic ligand shells can noticeably absorb IR radiation, thus limiting the spectral sensitivity range. The replacement of the oleate ligands in PbS CQDs by completely inorganic ligands provided a record-high long-wavelength operation of photoresistors (0.2 level at 3050 nm).[158] The responsivity was 0.14 A W^{-1}, the detectivity reached 1.1×10^{10} cm Hz$^{1/2}$ W^{-1}, and the frequency range was 3 kHz. A beneficial effect of ligand replacement was also noted by Konstantatos *et al.*,[159,160] who performed post-synthetic replacement of the oleate anion by n-butylamine and thus fabricated photoresistors with a specific detectivity D^* of approximately 10^{13} cm Hz$^{1/2}$ W^{-1} at room temperature. A noticeable result for PbS CQD photoresistors was attained by using completely inorganic As$_2$S$_3$ shells as stabilizers.[161] In the cited study, deposition of the absorbing film consisting of approximately 20 (NH$_4$)$_3$AsS$_3$-coated PbS CQD layers on a glass substrate was followed by heating at 130 °C; as a result, the ligand was converted to a thin As$_2$S$_3$ layer transparent for IR radiation. In a PbS CQD–As$_2$S$_3$-based photoresistor (≈0.08 mm^2 active area) with interdigitated Au electrodes (Fig. 21),[161] the specific detectivity was 1.2×10^{13} cm Hz$^{1/2}$ W^{-1} ($\lambda = 1.3$ µm) and the responsivity was 200 A W^{-1} ($\lambda = 1.4$ µm) at room temperature. The average size of the PbS colloidal
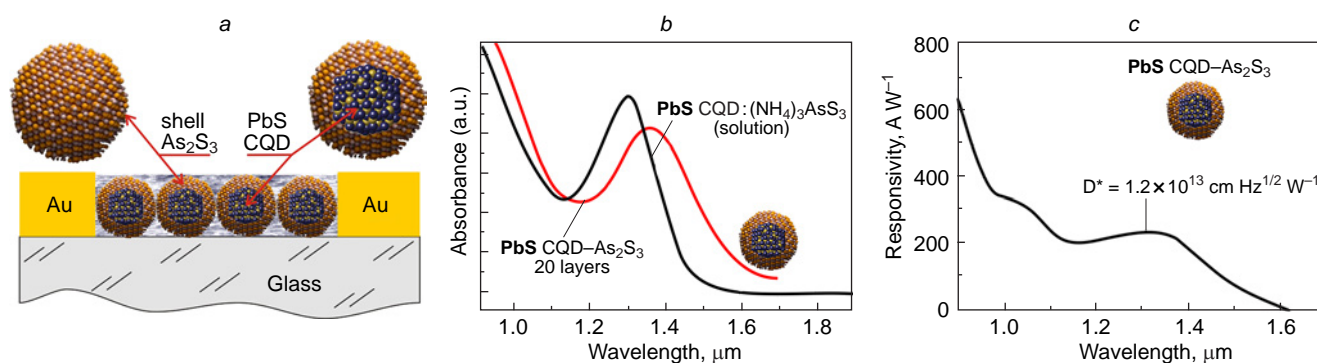
Figure 21. PbS CQD-based photoresistor with the As$_2$S$_3$ ligand: (*a*) photoresistor architecture; (*b*) spectral dependences of the absorbance of a PbS CQD:(NH$_4$)$_3$AsS$_3$ solution and a PbS CQD-As$_2$S$_3$ film; (*c*) spectral dependence of the responsivity and detectivity at λ = 1.3 µm. The Figure was created by the authors using published data.[161]

quantum dots was 4.3–4.4 nm, which resulted in a relatively short cut-off wavelength $\lambda_c \approx 1.5$ µm. He *et al.*[162] proposed a process for the formation of a photoresistive structure on a flexible substrate (paper-like material based on calcium carbonate and high-density polyethylene HDPE). A PbS CQD layer (the quantum dot diameter was 3.7 nm) was used as the photosensitive medium. Gold nanocrystals (8 nm in diameter) were introduced into the layer for doping and trap passivation, as described above for PbS CQD-based photoresistors with the addition of Ag nanocrystals. For a structure with an approximately 5% gold content, the specific detectivity was 1.1×10^{10} cm Hz$^{1/2}$ W^{-1}.

A number of publications address the properties of photoresistive structures based on PbSe CQDs.[121,163–168] The PbSe@PbS core@shell heterophase nanostructures were reported by Sashchiuk and co-workers.[164,166] The large exciton Bohr radius for bulk lead selenide (46 nm) promotes the formation of PbSe CQDs with a radius of more than 10 nm. The PbSe colloidal quantum dots obtained in 2001 by high-temperature colloidal synthesis at temperatures of 90–220 °C had diameters of 3.0 to 15.0 nm.[121] The range of optical absorption from 1.1 to 3.2 µm can be implemented in structures based on these quantum dots. Thambidurai *et al.*[167] reported photoresistors (Fig. 22) manufactured using PbSe CQDs of ~8 nm in diameter perating up to 2.8 µm wavelength.
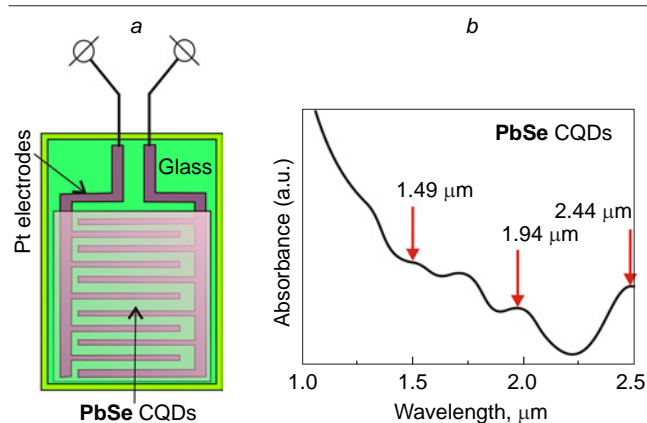
The responsivity, specific detectivity and quantum efficiency at an active layer thickness of 900 nm and at room temperature

Figure 22. Photoresistor composed of PbSe CQDs with interdigitated electrodes: (*a*) photoresistor architecture; (*b*) spectral characteristic of the absorption of a CQD solution.[167]

were 0.96 A W^{-1}, 8.13×10^9 cm Hz$^{1/2}$ W^{-1} and 78%, respectively.[167] Using lead stearate and a selenium solution in oleylamine (OLA–Se) as precursors, the authors synthesized PbSe nanocrystals of various shapes, including quasi-spherical, cubic, octahedral, cuboctahedral and star-shaped ones.[163] The nanocrystal size varied from 18.5 nm (quasi-spherical) to 46 nm (star-shaped).

The multiple exciton generation (MEG), that is, the formation of several excitons upon the absorption of one photon with the energy $hv \gg E_g$, was found for the structures based on PbSe CQDs.[169–171] Owing to the multiple exciton generation effect, a quantum yield of 300% was attained for solar cells.[170] In 2008, the MEG effect was detected for PbS CQDs.[172] A review of studies dealing with MEG was reported in 2018 by Goodwin *et al.*[173] A paper by Jin *et al.*[174] addressed MEG in manganese-doped PbSe@CdSe core@shell structures.

Some studies note the high sensitivity of the PbSe CQD surface to the surrounding atmosphere, which requires surface stabilization and protection. The adverse effect of the atmosphere is usually attributed to the adsorption of oxygen, which increases the density of surface traps that impair the performance of photosensors. A number of publications describe the methods for stabilization using chlorination in the CQD synthesis and protection by using core@shell type heterostructures.[166]

Several studies describe photoresistive structures based on HgTe and HgSe CQDs.[117,175–181] Tang *et al.*[117] and Keuleyan *et al.*[175,176] reported a process for the fabrication of a 12×12 mosaic array of photoresistors (Fig. 23 *a*). Each photoresistor in this two-dimensional array consists of three photosensitive elements with dimensions of approximately 220×220 µm attached to interdigitated electrodes (Au/Cr) for supplying power voltage and recording the photosignals (Fig. 23 *b*). Each of the three photosensitive elements is a HgTe CQD layer with a small, medium or relatively large diameter and thickness of 410, 340 or 210 nm deposited on top of the interdigitated electrodes (Fig. 23 *c*). Figure 23 *d* shows the spectral dependences of absorbance of HgTe CQDs with different quantum dot diameters. The cut-off wavelength of the photoresistor with a CQD layer of 20 nm was approximately 9.5 µm. The selected CQD sizes provided cut-off wavelengths for the three-element photoresistors of $\lambda_{c1} \approx 4.8$ µm, $\lambda_{c2} \approx 6.0$ µm and $\lambda_{c3} \approx 9.9$ µm.[117] The maximum responsivity was approximately 0.1 A W^{-1} and the specific detectivity was about 2×10^7 cm Hz$^{1/2}$ W^{-1}. These studies demonstrated the possibility of fabricating multiple-spectrum photosensors based on colloidal quantum dots sensitive in the short-wave, mid- and far-infrared ranges.

V.P.Ponomarenko, V.S.Popov, I.A.Shuklov, V.V.Ivanov, V.F.Razumov
Russ. Chem. Rev., 2024, **93** (4) RCR5113

17 of 48
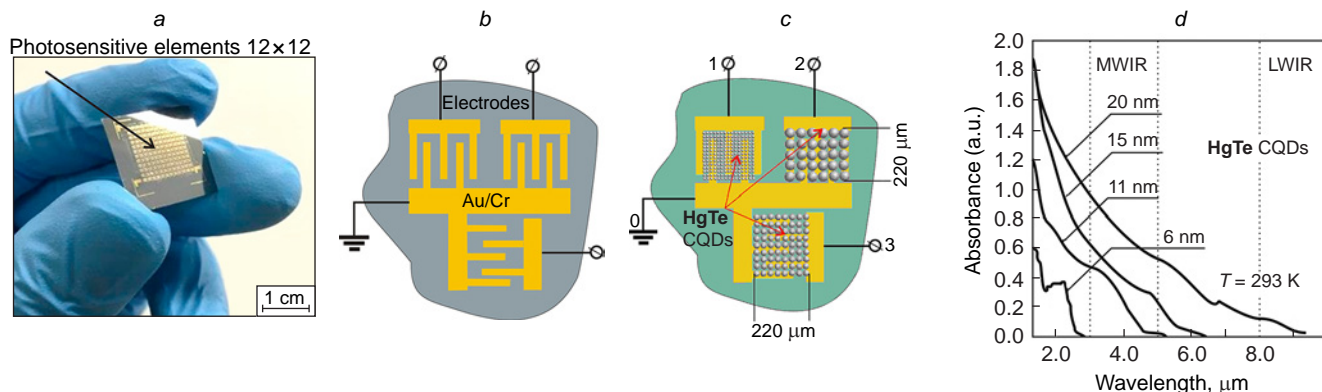
**Figure 23.** Three-spectrum mosaic photoresistor arrays based on HgTe CQDs: (*a*) external view of the product (12×12 array); (*b*) diagram of interdigitated metal electrodes (Au/Cr) on SiO$_2$/Si substrate; (*c*) three-electrode photoresistor based on colloidal quantum dots of three different diameters deposited onto metal electrodes; (*d*) spectral dependences of the absorbance of HgTe CQDs of 6, 11, 15 and 20 nm in diameter.[117]

Table 3. Key characteristics of few-element photoresistive structures based on PbS, PbSe, HgTe and HgSe CQDs.[156−163,177,179−182]

Absorption layer material	Cut-off wavelength λ_c, or sensitivity range $\Delta\lambda$ (μm)	Responsivity S_i, A W^{-1}, at wavelength λ	Specific detectivity D^*, cm Hz$^{1/2}$ W^{-1}	Temperature, K	Ref.
PbS CQDs	2.4 (λ_c)	50	3.4×10^8 (λ = 1.55 μm)	230	156
PbS CQDs : Ag NPs	0.4−1.7 ($\Delta\lambda$)	5	5×10^{11} (λ = 1.55 μm) 1.2×10^{12} (λ = 0.6 μm)	300	157
PbS CQDs	>3.0 (λ_c)	0.14 (λ = 2.7 μm)	⩾1×10^{10}	300	158
PbS CQDs−As$_2$S$_3$	0.9−1.5 ($\Delta\lambda$)	200	1.2×10^{13} (λ = 1.6 μm)	300	161
PbS CQDs	0.8−1.5 ($\Delta\lambda$)	2700	1.8×10^{13} (λ = 1.3 μm)	300	159
PbS CQDs	0.4−0.9 ($\Delta\lambda$)	113	5.0×10^{12} (λ = 0.6 μm)	300	160
PbS CQDs : Ag NPs	0.85−1.0 ($\Delta\lambda$)	0.0016	1.1×10^{10} (λ = 0.65 μm)	300	162
PbS CQDs	2.8 (λ_c)	0.96	8.0×10^9 (λ = 0.9 μm)	300	163
HgTe CQDs−As$_2$S$_3$	3.5 (λ_c)	0.1 (λ = 3.5 μm)	3.5×10^{10} (λ = 3.5 μm)	230	182
HgTe CQDs	2.3 (λ_c) 3.7 (λ_c) 4.3 (λ_c)	0.9 0.2 0.4	8.0×10^9 (λ = 2.3 μm)	300	179
HgSe CQDs	3−5 ($\Delta\lambda$)	(5−12)×10^{-3}	$D^*_{\text{BB 600 °C}}$ (500 Гц) = 8.5×10^8	80	180
HgSe CQDs	4.2 (λ_{max}) 6.4 (λ_{max}) 7.2 (λ_{max}) 9.0 (λ_{max})	0.145 (plasmonic disks) 0.092 (plasmonic disks) 0.089 (plasmonic disks) 0.086 (plasmonic disks)	− − − −	300 300 300 300	177 177 177 177
KKT HgSe	3−5 ($\Delta\lambda$)	0.077	1.2×10^9	80	181

Note. λ_{max} is the wavelength corresponding to the maximum sensitivity; NP is nanoparticle.
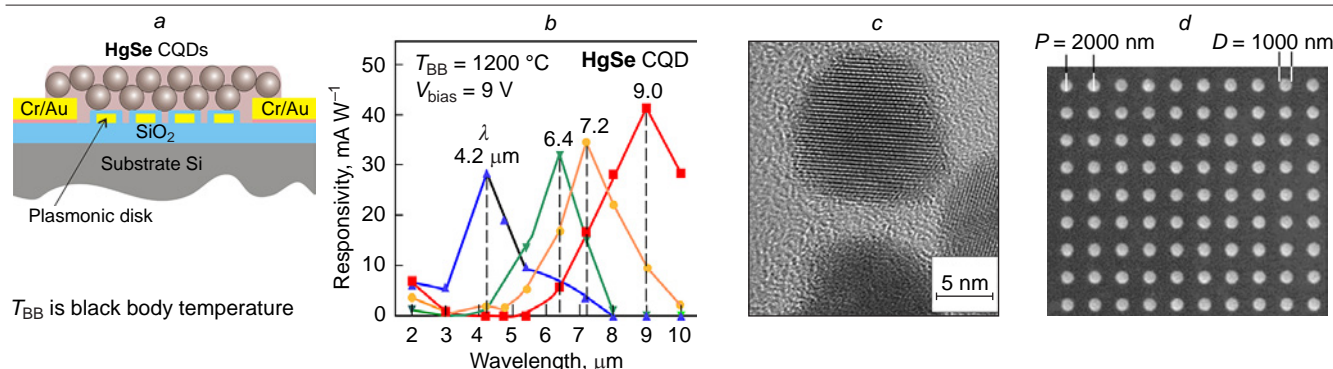
Figure 24. Photoresistor based on HgSe CQDs with plasmonic Au nanodisks: (*a*) photoresistor architecture; (*b*) spectral dependences of the responsivity of CQDs of different diameters (~5 to ~16 nm); (*c*) TEM image of CQDs; (*d*) SEM image of plasmonic disks of 1000 nm in diameter with a 2000 nm distance between the centres on the SiO$_2$ surface.[177]

18 of 48

V.P.Ponomarenko, V.S.Popov, I.A.Shuklov, V.V.Ivanov, V.F.Razumov
*Russ. Chem. Rev.*, 2024, **93** (4) RCR5113

Tang *et al.*[177] investigated photosensors based on HgSe CQDs. Photosensors with the structure depicted in Fig. 24 *a* represented photoresistors fabricated on the SiO$_2$/Si chip. The photoconductivity was due to $1S_e \to 1P_e$ intraband transitions. The size of colloidal quantum dots determining the spectral sensitivity range was ~5 to ~16 nm and was specified by the synthesis temperature and time. The photosensitivity was implemented over a wide wavelength range. The centre wavelengths for the four studied photoresistors were $\lambda_{max1} = 4.2$ μm, $\lambda_{max2} = 6.4$ μm, $\lambda_{max3} = 7.2$ μm and $\lambda_{max4} = 9.0$ μm (Fig. 24 *b*). The high-resolution transmission electron microscopy (TEM) image of HgSe CQDs is shown in Fig. 24 *c*. For increasing the optical absorption, the authors used plasmonic antennas, which were designed as metal nanodisks, with their size and distance between them being specified depending on the size of quantum dots and absorbed wavelength. The nanodisks were made of 80 nm-thick gold layers and coated with approximately 10 nm-thick SiO$_2$ layers. For $\lambda_{max1} = 4.2$ μm, the plasmonic disk diameter was $D = 1000$ nm, while the distance P between the centres of the disks on the SiO$_2$ film coating the Si substrate was chosen to be equal to $2D$ (Fig. 24 *d*). The responsivities for the elements characterized by the centre wavelengths were 145, 92.3, 88.6 and 86.0 mA W^{-1}.

The key characteristics of few-element photoresistive structures based on PbS, PbSe, HgTe and HgSe CQDs are presented in Table 3.[156–163,1177,179–182]

5.3. Photosensors with energy barriers

This Section addresses heterosystems consisting of several contacting solid phases composed of colloidal quantum dot arrays with different band gaps or arrays of identical CQDs but characterized by different types of conduction in different parts of the heterosystem. In all cases, these heterophase photosensors have one or more energy barriers, which provide effective separation of charge carriers formed upon the decay of excitons generated by the absorbed radiation. The energy barriers of photosensors may be based on various types of heterojunctions (P-n, N-p, P-p, n-N), Schottky barriers, p-i-n homo- and heterojunctions, bariode heterosystems, *etc*. Most of modern photosensor arrays made of traditional 3D semiconductors are based on the same principles.

Photovoltaic sensors for measuring IR radiation that are being developed or have been developed to date using CQDs can be conventionally assigned to one of the following types: Schottky photodiodes, p-n junction structures, p-i-n structures, transistor structures and heterojunction structures of various types. Analysis of the available literature devoted to this subject
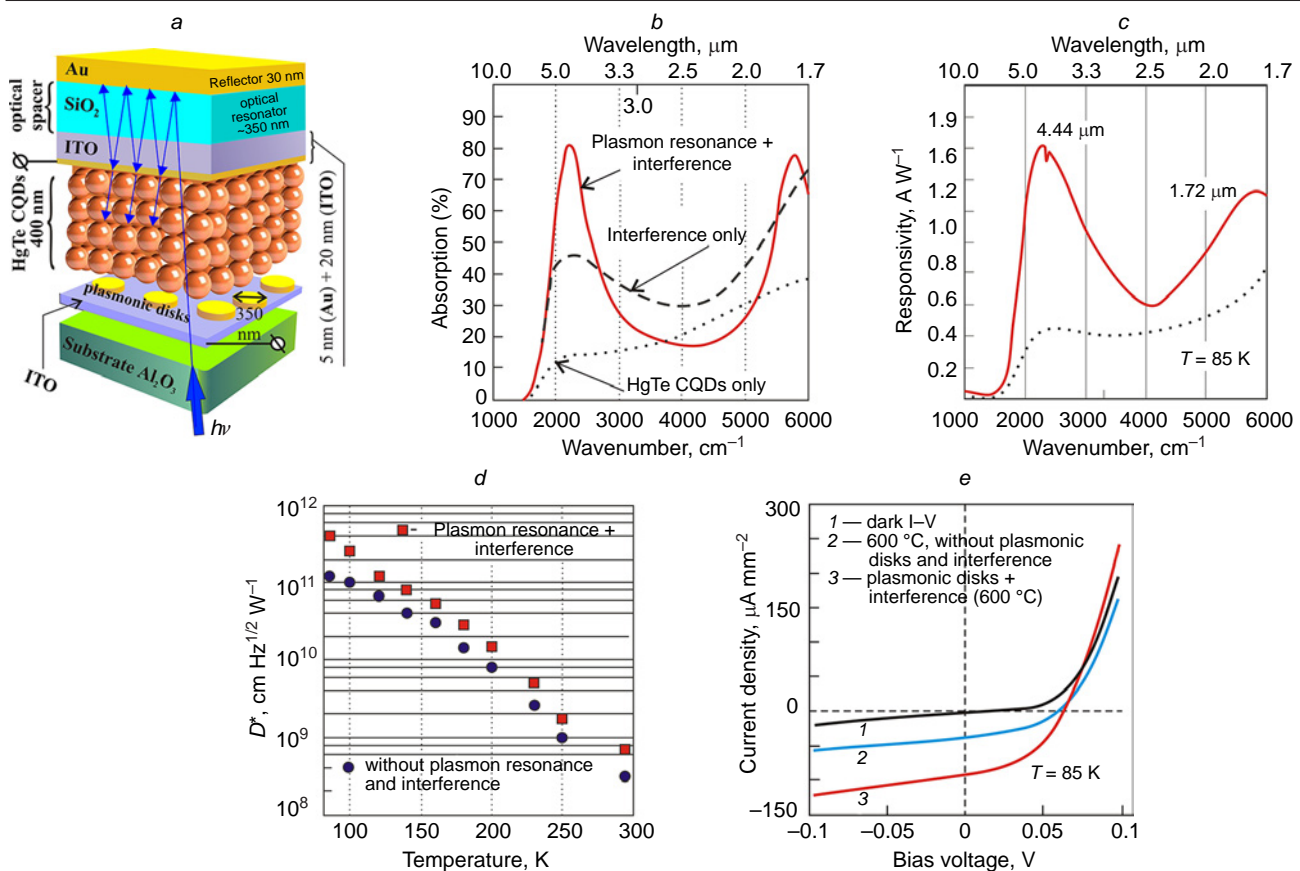
Figure 25. Photodiode sensor with a Schottky energy barrier based on HgTe CQDs with plasmonic disks and interference device: (*a*) photosensor architecture; (*b*) absorption curves in the presence (continuous line) and in the absence of plasmonic disks and interference device (dashed line); (*c*) spectral sensitivity of the photosensor in the presence of plasmonic disks and interference device; (*d*) temperature dependence of the detectivity under illumination from a black body (BB) at $T_{BB} = 600$ °C and modulation frequency of 500 Hz; (*e*) CVC of the photodiode structure under illumination from a BB at $T_{BB} = 600$ °C (curves *2* and *3*) and without illumination (curve *1*) in the presence (curve *3*) or in the absence (curve *2*) of plasmonic disks and interference device; the dashed line in Figures (*b*, *c*) shows dependence of the absorbance and sensitivity on the wavelength without plasmonic disks and interference device.[70]

V.P.Ponomarenko, V.S.Popov, I.A.Shuklov, V.V.Ivanov, V.F.Razumov
Russ. Chem. Rev., 2024, **93** (4) RCR5113

19 of 48

indicates that various organic and nanocomposite materials consisting of a conductive organic polymer and inorganic nanoparticle are widely used in these designs (for example,[183]). The range of organic compounds applied in this area is very broad and is largely inherited from solar cell and organic light-emitting diode technologies. In the beginning of the 21st century science and engineering areas called 'organic photonics' and 'organic optoelectronics' appeared in optoelectronics.[184,185]

Tang *et al*.[70] studied a photodiode structure with a Schottky barrier at the *HgTe CQD/Au* contact (where Au acts as the top contact) (Fig. 25 *a*). The bottom contact was made of ~30 nm-thick ITO layer, on which Au plasmonic disks were deposited. The most pronounced plasmon resonance in the described structure was attained in the case of 350 nm diameter of plasmonic disks and approximately 700 nm distance between their centres. The optical absorption curves in the $1.7-5$ μm wavelength range are shown in Fig. 25 *b* and demonstrate the effect of plasmon resonance and the optical interference device located in the upper part of the structure on the absorbance. The highest responsivity reached 1.62 A W^{-1} (Fig. 25 *c*), which corresponds to quantum efficiency of 45%. The presence of plasmonic disks increased the specific detectivity from 1.2×10^{11} to 4×10^{11} cm Hz$^{1/2}$ W^{-1} at $T = 85$ K and from 3.1×10^8 to 7.2×10^8 cm Hz$^{1/2}$ W^{-1} at $T = 295$ K. At the temperature $T = 220$ K, which can be attained using a thermoelectric cooler, a specific detectivity of 1×10^{10} cm Hz$^{1/2}$ W^{-1} can be reached (Fig. 25 *d*). The effect of plasmon resonance and interference devices on the current–voltage characteristic of the photodiode structure is depicted in Fig. 25 *e*.

Subsequently, a few more structures of photovoltaic sensors based on HgTe CQDs with a Schottky barrier have been proposed and studied. Jagtap *et al*.[186] described a Schottky photodiode with the *glass/ITO/TiO$_2$ CQDs/HgTe CQDs/Au* structure (Fig. 26 *a*) and sensitivity up to $\lambda_c \approx 2.5$ μm (4000 cm^{-1}). Owing to the electron type of conduction of titanium dioxide, the barrier at the *TiO$_2$/HgTe CQDs* interface prevents the passage of photoholes, thus reducing the dark current. The current–voltage characteristic of the photodiode structure is shown in Fig. 26 *b*. The specific detectivity at room temperature was 1.5×10^7 cm Hz$^{1/2}$ W^{-1}.

The subsequent advancement of HgTe CQD photodiodes is associated with the development of ways to expand the spectral
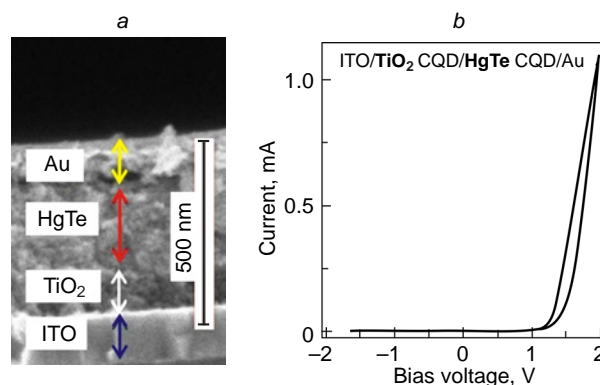
Figure 26. Schottky barrier photodiode with the glass/ITO/TiO$_2$ CQDs/HgTe CQDs/Au structure (*a*) SEM image of the structure cross-section; (*b*) photodiode CVC.[186]

sensitivity range and reduce dark currents, which noticeably reduce the detectivity, by incorporating energy barriers similar to the blocking barriers in bariode heterosystems XB$_n$n and XB$_p$p, capable of suppressing the dark injection of electrons and holes.[187] This photosensor for recording the IR radiation at $\lambda > 2$ μm has the structure: *substrate/ITO or FTO/TiO$_2$ CQDs/ i-HgTe CQDs/p-HgTe CQDs/MoO$_3$/Au* (Fig. 27 *a*), where FTO is fluorine-doped tin oxide.[188,189] The radiation is absorbed in the HgTe CQD layer with ambipolar conduction ($\lambda_c = 2.9$ μm). CQDs with cut-off wavelengths λ_c of 6000 cm^{-1} (1.67 μm), 4000 (2.5 μm) and 700 cm^{-1} (14.3 μm) have the hole, ambipolar and degenerate electron types of conduction, respectively.[188] The TiO$_2$ layer suppresses the dark current of holes from the ITO (or FTO) layer, while p-type HgTe CQD and MoO$_3$ layers block the dark electron current from the gold contact (Fig. 27 *b*). A specific detectivity of 3×10^8 cm Hz$^{1/2}$ W^{-1} (Fig. 27 *c*) at $T = 300$ K was implemented in the structure.

A photosensor based on the *HgTe CQDs : HgSe CQDs* mixture with random distribution of CQDs in the layer was proposed in 2019 (Fig. 28 *a*).[190] An energy structure (Fig. 28 *b*) similar to the structure of multiple quantum wells in GaAs/AlGaAs-based QWIP (Fig. 28 *c*) is formed in this case in the CQD nanolayer. The photosensor is a photodiode structure in which the illumination is performed through a thin (80 nm)
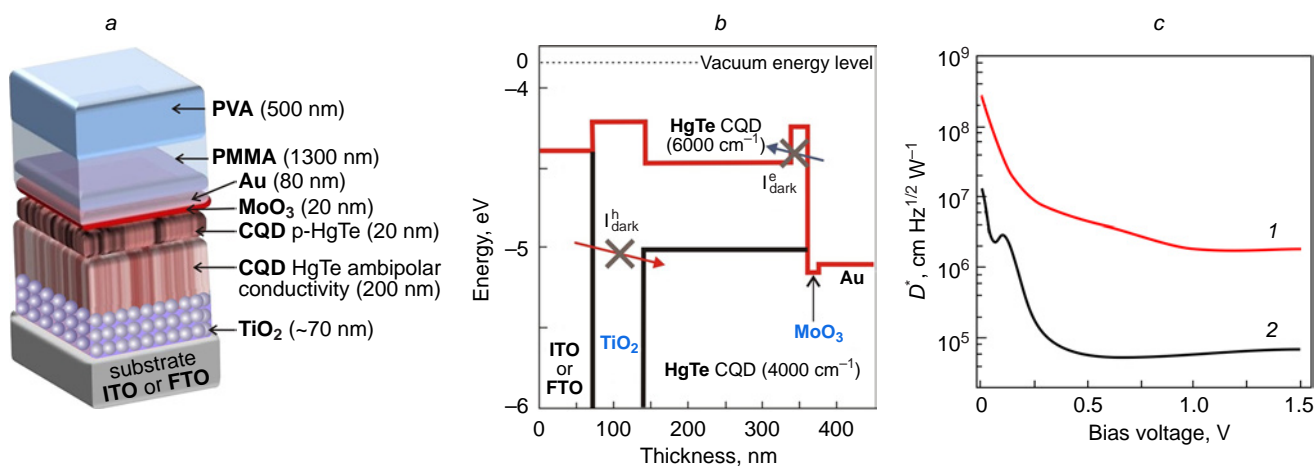
Figure 27. Photodiode with a unipolar energy barrier at the *TiO$_2$/HgTe CQD* contact with unipolar conduction and an additional barrier at the *MoO$_3$/Au* contact: (*a*) photodiode structure; (*b*) energy diagram of the structure; (*c*) specific detectivity: (1) for the photosensor shown in Fig. 27 *a*, (2) for the photosensor shown in Fig. 26 *a*.[188,189] PVA is poly(vinyl acetate), PMMA is poly(methyl methacrylate).
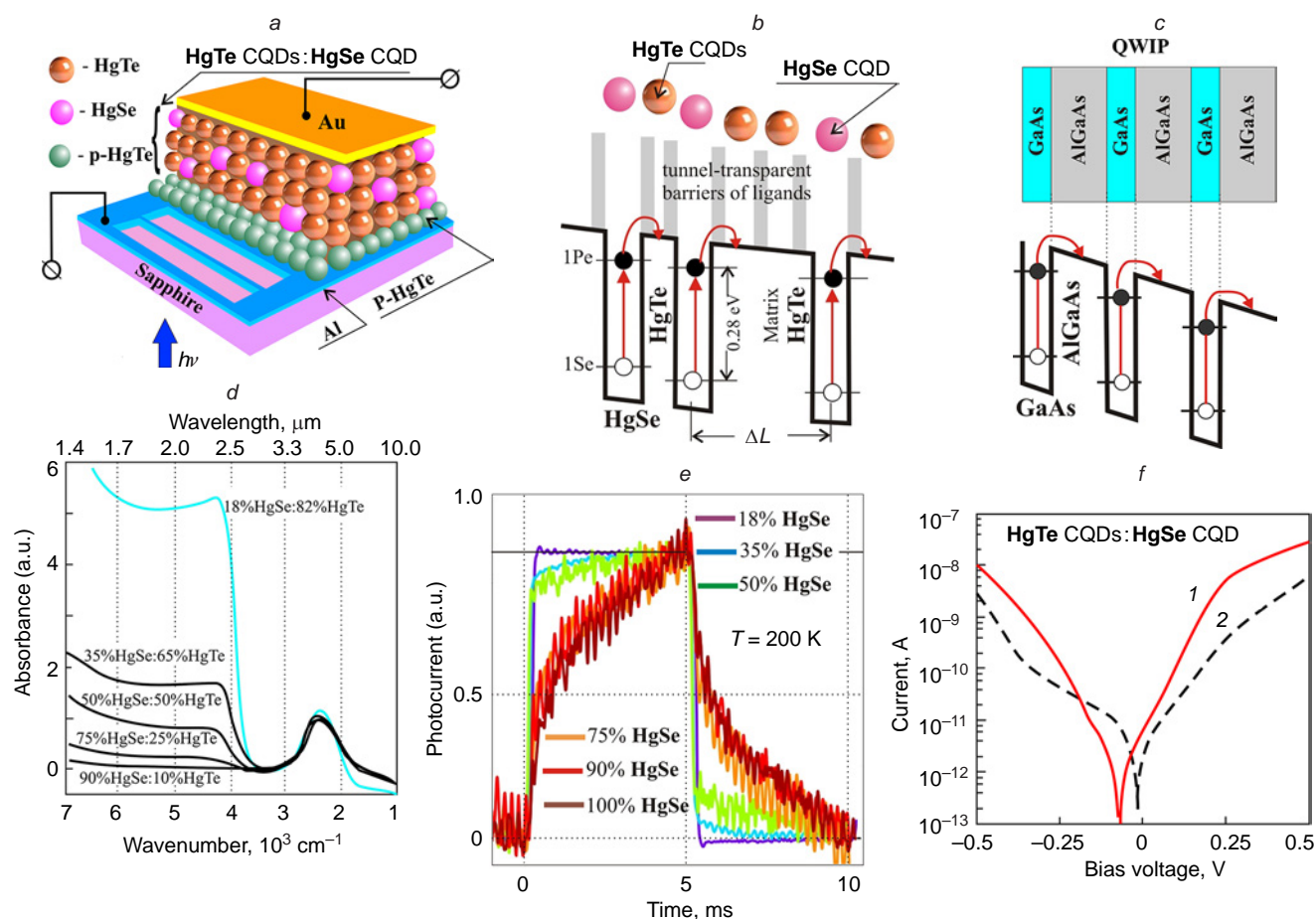
Figure 28. Structure and characteristics of the photosensor based on the *HgSe CQD : HgTe CQD* mixture: (*a*) photosensor structure; (*b*) energy diagram of the photosensor based on the *HgSe CQD : HgTe CQD* mixture; (*c*) energy diagram of the QWIP photosensor based on *GaAs/AlGaAs*; (*d*) absorption spectrum of nanolayers consisting of a *HgSe CQD : HgTe CQD* mixture with different contents of HgSe and HgTe at a HgTe CQD diameter providing a cut-off wavelength of 2.5 µm; (*e*) photoresponse relaxation time for different contents of HgSe at $T = 200$ K; (*f*) current–voltage characteristics of the photodiode structure at $T = 80$ K, (*1*) under illumination at $\lambda \cong 4.4$ µm, (*2*) without illumination.[190]
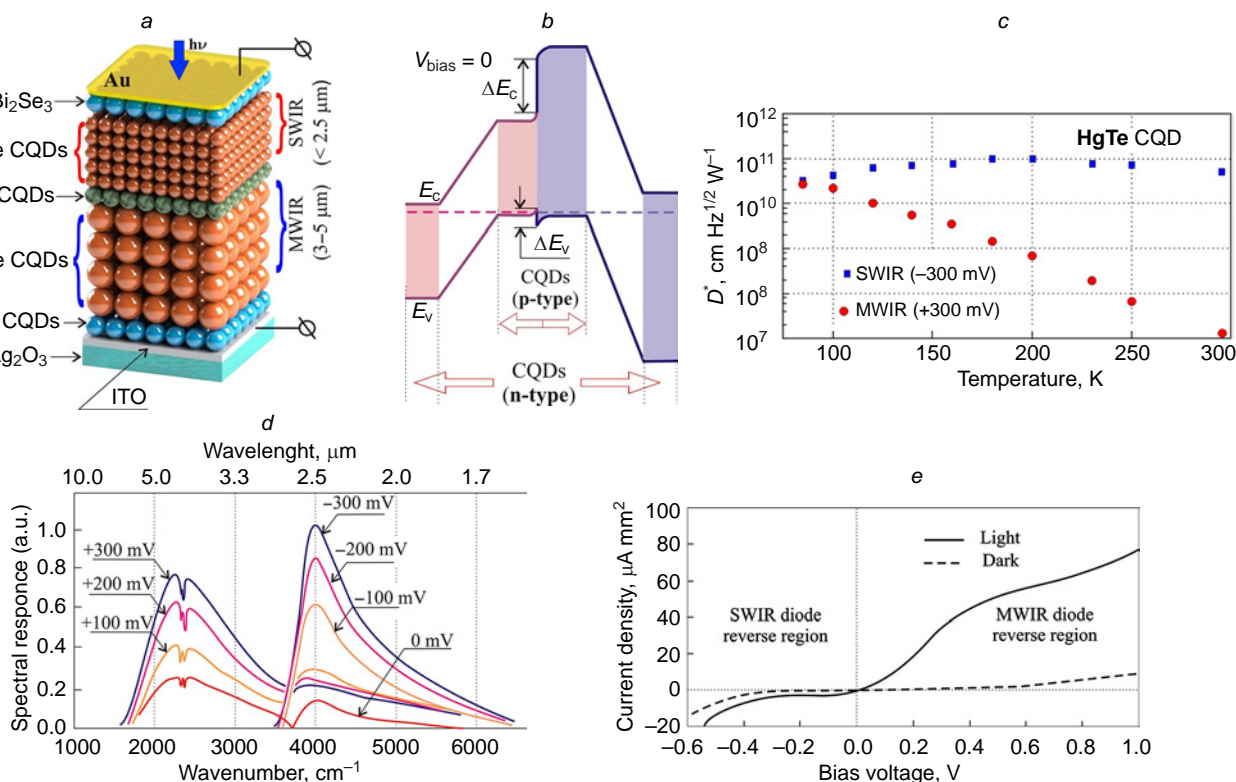
aluminium electrode with 70% optical transmittance in the mid-IR region. The HgTe nanocrystals provide the formation of an energy barrier (analogues of AlGaAs in QWIP), while HgSe nanocrystals are responsible for the appearance of energy wells (analogue of GaAs in QWIP). Thus, the device combines the intraband absorption *via* $1S_e \rightarrow 1P_e$ transitions in HgSe CQDs and the transport of photocarriers over barriers formed by HgTe CQDs (the mobility is higher in HgTe than in HgSe). The optical and transport properties of the quantum dot layer consisting of the *HgTe CQD : HgSe CQD* mixture depends on the dot size and the relative content of HgSe in the HgTe matrix. Figure 28*d* shows the photosensitivity spectrum for several *HgTe CQD : HgSe CQD* mixtures with different contents of HgSe (the HgTe CQD matrix consists of quantum dots with a diameter providing the cut-off wavelength $\lambda_c \approx 2.5$ µm). The photoresponse relaxation time shown in Fig. 28*e* (measured for field-effect transistor samples with channels made of *HgTe CQD : HgSe CQD* mixtures) is approximately 1 ms when the HgSe fraction is high and decreases below 100 µs with increasing HgTe fraction. By reducing the fraction of HgSe CQDs from 100% to 18%, it is possible to increase the effective energy barrier width [*i.e.*, the average distance ΔL (Fig. 28*b*) between nanocrystals in the HgSe : HgTe layer] from ~1 to ~60 nm. The responsivity of the photodiode structure upon illumination from BB with 1.9 µm high-pass filter is a few mA W^{-1}. The noise is defined as $1/f$. The specific detectivity at

$T = 80$ K and modulation frequency of 1 kHz was $D^*_{BB} \cong 1.5 \cdot 10^9$ cm Hz$^{0.5}$ W^{-1}. The current–voltage characteristics of the photodiode structure are depicted in Fig. 28*f*.

In 2019, X.Tang *et al.*[191] developed and studied the architecture of a dual-band photosensor for the 1.5–2.5 µm (SWIR) and 3–5 µm (MWIR) spectral ranges consisting of two photodiodes based on colloidal quantum dots combined into one n-p-n structure (Fig. 29*a*). SWIR radiation is absorbed by the top photodiode consisting of HgTe CQDs of 6 nm in diameter. The MWIR radiation is absorbed in the bottom layer consisting of HgTe CQDs of 9 nm in diameter. The 5 nm-thick semi-transparent Au top electrode transmits ~60% of incident IR radiation. The bottom electrode is fabricated of ITO layer deposited on the Al_2O_3 substrate. Switching from one band to another is performed by changing the polarity of voltage applied to the structure. The n- and p-regions of the photodiode are generated using doped Bi_2Se_3 CQD and Ag_2Te CQD layers, which serve as sources of donor and acceptor impurities in the HgTe CQD layers.

The diffusion of Ag$^+$ ions gives rise to the acceptor p-layer, whereas the n-layer is formed due to the charge transfer from the Bi_2Se_3 phase to HgTe. The energy diagram of the photosensor structure is shown in Fig. 29*b*. The specific detectivity of the SWIR photodiode in the presence of the Bi_2Se_3 n-layer reaches 6×10^{10} cm Hz$^{1/2}$ W^{-1} at room temperature and increases to 1×10^{11} cm Hz$^{1/2}$ W^{-1} on cooling to 200 K (Fig. 29*c*). The

V.P.Ponomarenko, V.S.Popov, I.A.Shuklov, V.V.Ivanov, V.F.Razumov
Russ. Chem. Rev., 2024, **93** (4) RCR5113

21 of 48

Figure 29. Dual-band photosensor based on CQD photodiodes combined into a single n-p-n structure: (*a*) photosensor structure; (*b*) energy diagram; (*c*) temperature dependences of the specific detectivity for SWIR and MWIR photodiodes forming the dual-band photosensor; (*d*) spectral dependences of the photoresponse at different bias voltages applied to the photosensor; (*e*) photosensor CVC.[191]

spectral dependences of the photosensitivity and CVC of photodiodes are shown in Figs 29 *d,e*.

By 2023, the detectivity of photodiodes based on HgTe CQDs reached 1×10^{11} cm Hz$^{1/2}$ W^{-1} at room temperature ($\lambda = 2.2$ μm, $T = 300$ K)[192] and approximately 1×10^{10} cm Hz$^{1/2}$ W^{-1} at low temperature ($\lambda = 4 - 5$ μm, $T = 200$ K).[193] With an appropriate selection of ligands, the responsivity S_i and charge carrier mobilities μ_e and μ_h at room temperature were $S_i = 0.23$ A W^{-1}, $\mu_e = 3.4$ cm$^2 \times$ V$^{-1} \times$ s^{-1} and $\mu_h = 0.45$ cm$^2 \times$ M$^{-1} \times$ s^{-1}.[194] The use of plasmonic structures to enhance optical absorption provided an increase in S_i to approximately 1.6 A W^{-1}.[70]

The highest reported parameters of photosensors based on HgTe CQD photodiodes with a dot gradient homojunction were described by Xue *et al.*[195] At $\lambda = 4.2$ μm and 80 K, the specific

detectivity and responsivity were $D^* = 2.7 \times 10^{11}$ cm Hz$^{1/2}$ W^{-1} (Fig. 30 *c*) and 2.7 A W^{-1}, respectively, and the quantum efficiency reached 77%.[195] Note that the detectivity of photodiodes operating in the background limited infrared photodetector (BLIP) mode does not exceed $D^*_{\lambda = 4.2 \text{ μm}}$ (BLIP, $T_{background} = 300$ K, $\theta = 2\pi$, $f = 100$ Hz is the radiation modulation frequency) $\cong 3 \times 10^{11}$ cm Hz$^{1/2}$ W^{-1}.[4] Thus, the described photosensor based on HgTe CQDs[195] actually has the highest possible detectivity for photodiode structures in the mid-wave IR range. The indicated result for HgTe CQDs was implemented owing to the original architecture (dot gradient homojunction) proposed earlier by Xue *et al.*[195] (Fig. 30 *a,b*) for a PbS CQD-based photodetector.[195] A three-stage procedure of primary ligand replacement modified by the authors was also used to implement the photosensor architecture *Au/p-HgTe*
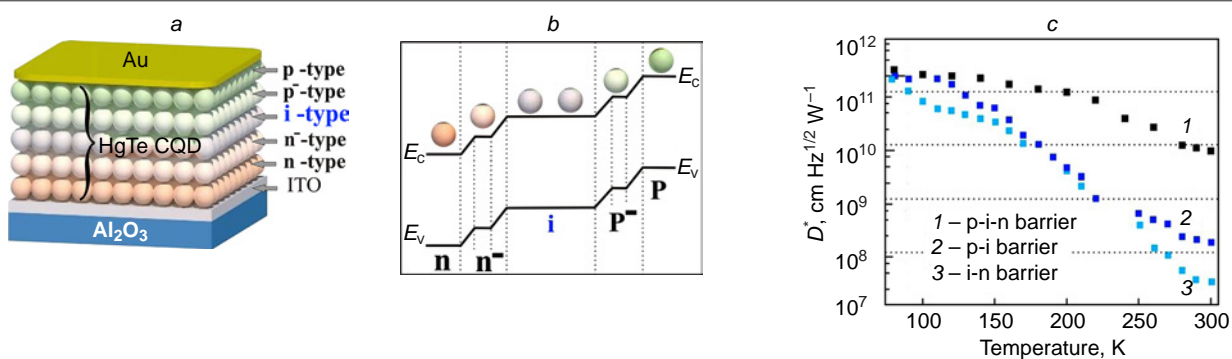
Figure 30. Photosensor based on HgTe CQDs with a dot gradient homojunction: (*a*) architecture; (*b*) energy diagram; (*c*) spectral dependence of the specific detectivity of photosensors the architecture of which involves p-i, i-n and p-i-n energy barriers.[195]
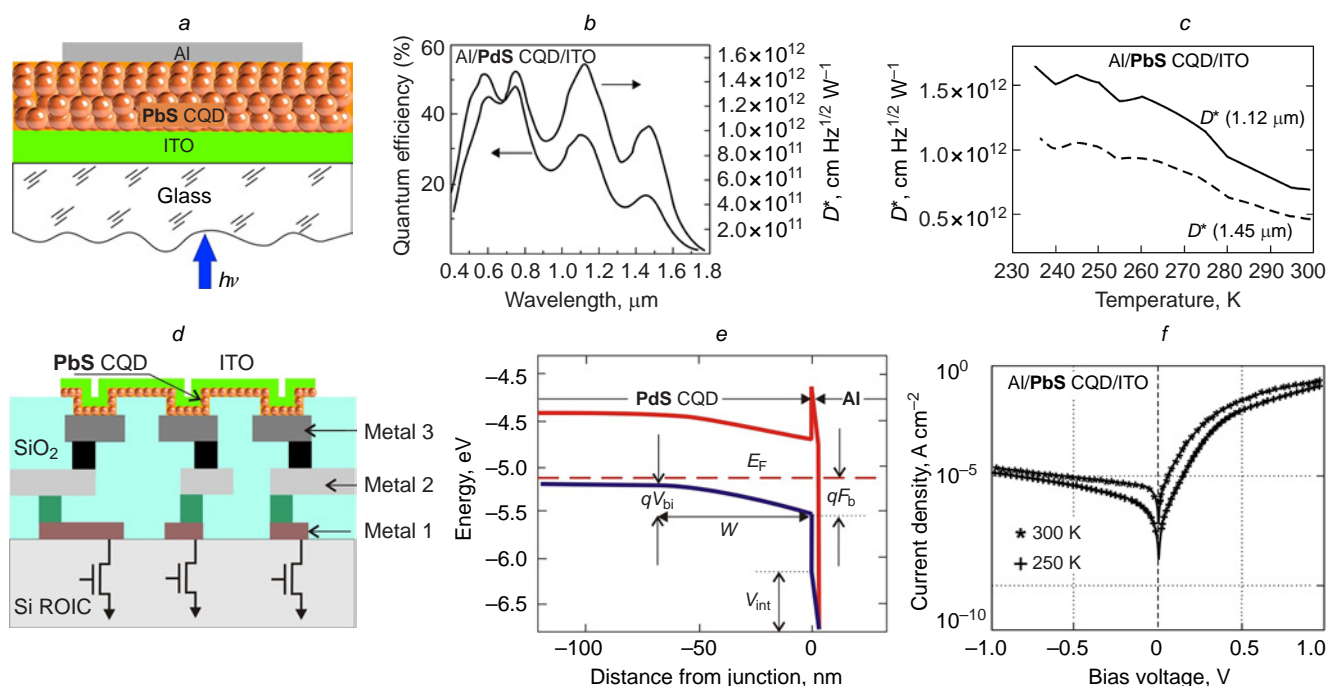
Figure 31. Photodetector with the Schottky barrier at the *Al/PbS CQDs/ITO/glass substrate*: (*a*) photodetector architecture;[197] (*b*) spectral dependence of the quantum efficiency at $T = 295$ K and specific detectivity at $T = 250$ K;[198] (*c*) temperature dependences of specific detectivity;[198] (*d*) diagram of addition of Schottky photodiodes to the readout integrated circuit;[183] (*e*) energy diagram of the structure, where E_F is the Fermi level, q is the charge of the electron, F_b is the height of Schottky barrier, V_{bi} is the built-in potential, V_{int} is the potential drop near the barrier;[196] (*f*) current–voltage characteristics of the Schottky diode at various temperatures.[196]

CQDs/p⁻-HgTe CQDs/i-HgTe CQDs/n⁻-HgTe CQDs/n-HgTe CQDs/ITO/sapphire and provided high charge carrier mobility in the HgTe CQD layer, exceeding 1 cm² V⁻¹ s⁻¹.

Photovoltaic sensors based on CQDs of binary compounds of A^{IV} and B^{VI} elements were designed with Schottky barriers at the *CQDs/metal* contact, various heterostructures including polymer materials and 2D elements, and barriers at the contact between p- and n-type CQD layers.

Clifford *et al*.[196,197] studied a SWIR photosensor with a Schottky barrier with the *Al/PbS CQD/ITO/glass substrate* structure (Fig. 31).[183,196–198] The quantum dot absorption layer with a thickness of approximately 100–300 nm consisted of PbS nanocrystals of ~6 nm in diameter.[196,197] The Schottky barrier was formed at the contact between PbS CQD and a 100 nm-thick aluminium layer (3.14 mm² area) fabricated by thermal deposition. The effective band gap in the semiconductor quantum dots (the distance between the $1S_e$ and $1S_h$ levels) amounted to 0.86 eV, which is close to the value found from the relation $E_g = 0.41 + (0.0392 D^2 + 0.114 D)^{-1}$ (where D is the CQD diameter). The following photodetector characteristics were attained: spectral sensitivity range of 0.4–1.8 µm, quantum efficiency $\approx 17\%$ ($\lambda = 1.55$ µm), specific detectivity $D^* = 1.5 \times 10^{12}$ cm Hz$^{1/2}$ W⁻¹ ($\lambda = 1.12$ µm, $T = 250$ K), $D^* = 0.7 \times 10^{12}$ cm Hz$^{1/2}$ W⁻¹ ($\lambda = 1.12$ µm, $T = 300$ K), $D^* = 0.4 \times 10^{12}$ cm Hz$^{1/2}$ W⁻¹ ($\lambda = 1.6$ µm, $T = 250$ K) and $D^* = 0.8 \times 10^{12}$ cm Hz$^{1/2}$ W⁻¹ ($\lambda = 1.45$ µm, $T = 300$ K) and transmission band width >2.9 MHz.[197,198]

The relatively low quantum efficiency in Schottky barrier structures in the wavelength range $\lambda > 1.2$ µm (~17%) stimulated the development of photosensitive elements based on PbS CQDs and heterojunction structures using organic polymers.

The architecture of a photosensor with a bulk heterojunction and the active layer made of the PbS *CQD:PCBM:P3HT:ZnO CQD* mixture for the 0.3–1.1 µm

range is shown in Fig. 32*a*.[199] The average size of PbS CQDs and ZnO CQDs is 3.3–3.7 nm and 5.0 nm, respectively. Initially, two mixtures, *PbS CQD:PCBM:P3HT* and *ZnO CQD:PCBM:P3HT*, were prepared; then they were mixed to form a four-component mixture. The thickness of the active layer was 200–300 nm. The spectral dependence of the sensor photosensitivity is shown in Fig. 32*b*. Due to the presence of ZnO CQDs in the active layer, the short-wave sensitivity extends up to the UV region. In the absence of illumination, this structure behaves as a photodiode, while under illumination, ohmic conduction is observed. The spectral characteristics of the detectivity for this structure is shown in Fig. 32*c*.

SWIR photodetectors fabricated as *Al/ZnO NPs/PbS@CdS/P3HT/PEDOT:PSS/ITO* structures with the active absorption layer based on core@shell quantum dots, with the core consisting of PbS nanocrystals and the shell being made of CdS ($\lambda_c \approx 1.45$ µm, and the first exciton absorption peak is located at 1.41 µm), were studied by Kwon *et al*.[200] By varying the core and shell materials, one can deliberately control the properties of the structure, where the core determines the absorption spectrum and the shell provides passivation of the core surface and low recombination of charge photocarriers. The average size of PbS colloidal quantum dots used to manufacture these photodetectors was in the 4.6–5.6 nm range, and the active absorption layer area was 9 mm². The attained responsivity was 600 A W⁻¹, while the specific detectivity was very high, 7.4×10^{12} cm Hz$^{1/2}$ W⁻¹. High characteristics of the photovoltaic solar cells based on core@shell quantum dots made of various materials were noted by Selopal *et al*.,[201] who demonstrated good prospects of using these structures in photosensorics.

Due to the relatively high bond energies in organic materials, the photogenerated excitons dissociate slowly, thus deteriorating the photosensor performance. The use of PbS CQDs, the size of which is controlled by varying the conditions

V.P.Ponomarenko, V.S.Popov, I.A.Shuklov, V.V.Ivanov, V.F.Razumov
Russ. Chem. Rev., 2024, **93** (4) RCR5113

23 of 48
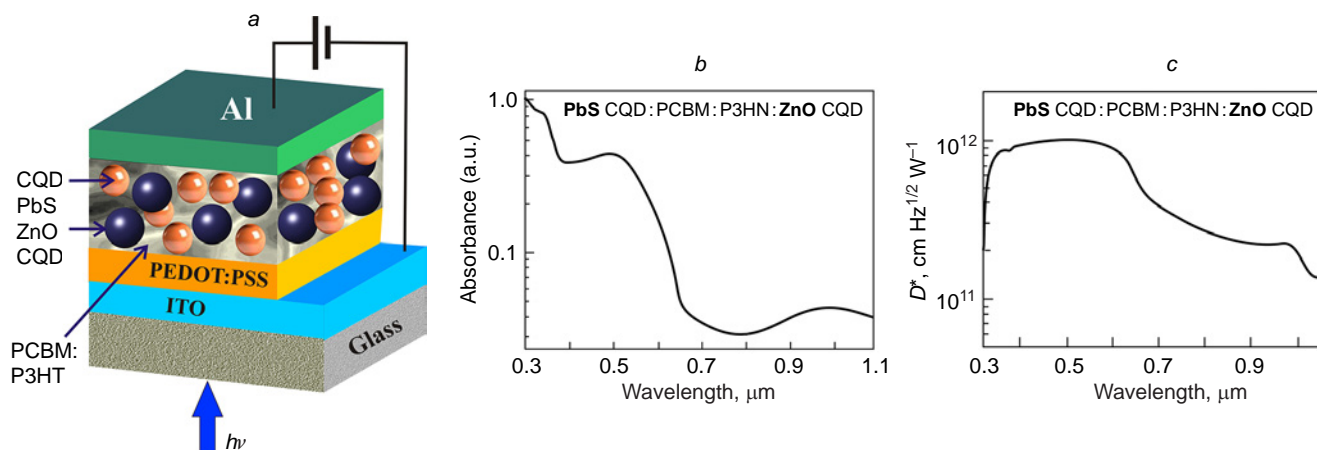
Figure 32. Photovoltaic cell with active absorption region based on the *PbS CQD : PCBM : P3HT : ZnO CQD* mixture with bulk heterojunction: (*a*) cell architecture; spectral dependences of the (*b*) absorbance and (*c*) specific detectivity.[199]

of synthesis, makes it possible to form a heterojunction providing an efficient separation of electrons and holes formed upon the photoexciton dissociation. The architecture of this photosensor is fabricated by deposition of a film made of a mixture of organic materials on the PbS CQD layer.[202] The average size of PbS CQDs used in the cited study is 3 nm; the first exciton absorption peak is located at 0.77 µm. After replacement of the oleate anion used in the PbS CQD synthesis by the iodide anion by treatment CQDs with tetra-n-butylammonium iodide (TBAI), the exciton absorption peak shifts to 0.83 µm. The organic polymer PBDB-T mixed with polyimidazoleporphyrin PBI-Por was used as the second layer deposited on top of the *PbS CQD-TBAI* layer.

The photosensitive element had the structure *Al/PBDB-T : PBI-Por/PbS CQD-TBAI/PBDB-T : PBI-Por/Al*. The specific detectivity at 0.63 µm was 1.12×10^{13} cm Hz$^{1/2}$ W^{-1}. The photosensors with sharply unsymmetrical energy barriers at the *n-ZnO/p-PbS CQDs* and *n-TiO$_2$/p-PbS CQDs contacts* in *Al/n-ZnO/p-PbS CQDs/PEDOT : PSS/ITO* and *Au/p-PbS CQDs/n-TiO$_2$/ITO* structures, characterized by a quantum efficiency of

approximately 70–80% ($\lambda = 0.5 - 0.6$ µm), were studied by Pal *et al*.[203]

Due to the large surface area to volume ratio of PbS CQDs, the surface atoms can strongly affect the conductivity and charge carrier mobility in the layers of colloidal quantum dots. Thus, by selecting the appropriate ligand, it is possible to control, within certain limits, the energy levels of the conduction band minimum (CBM), valence band maximum (VBM) and the Fermi level (E_F) in the CQD layer. Figure 33 *a* shows the VBM, CBM and E_F energy levels for PbS CQDs with various ligands such as benzene-1,2-dithiol (1,2-BDT), benzene-1,3-dithiol (1,3-BDT), benzenethiol (BT), ethane-1,2-dithiol (EDT), 3-mercapto-propionic acid (MPA), ethylene-1,2-diamine (EDA), ammonium thiocyanate, tetra-n-butylammonium halides [tetra-n-butyl-ammonium fluoride, TBAF; tetra-n-butylammonium chloride, TBACl; tetra-n-butylammonium iodide, TBAI], *etc*. (Scheme 2).[204] In the case of 1,3-BDT ligand, the Fermi level in the PbS CQD layer occurs near the centre of the band gap, thus providing a conduction mechanism close to the intrinsic conduction. Using this ligand, Lee *et al*.[205] designed a p-i-n

Structures of PBDB-T and PBI-Por
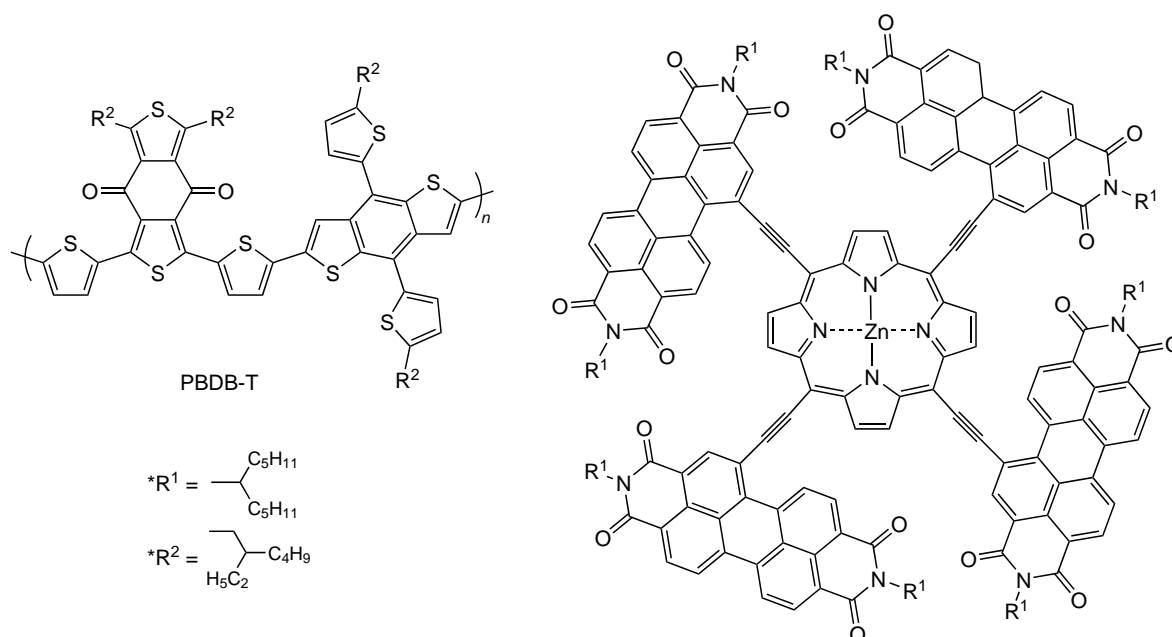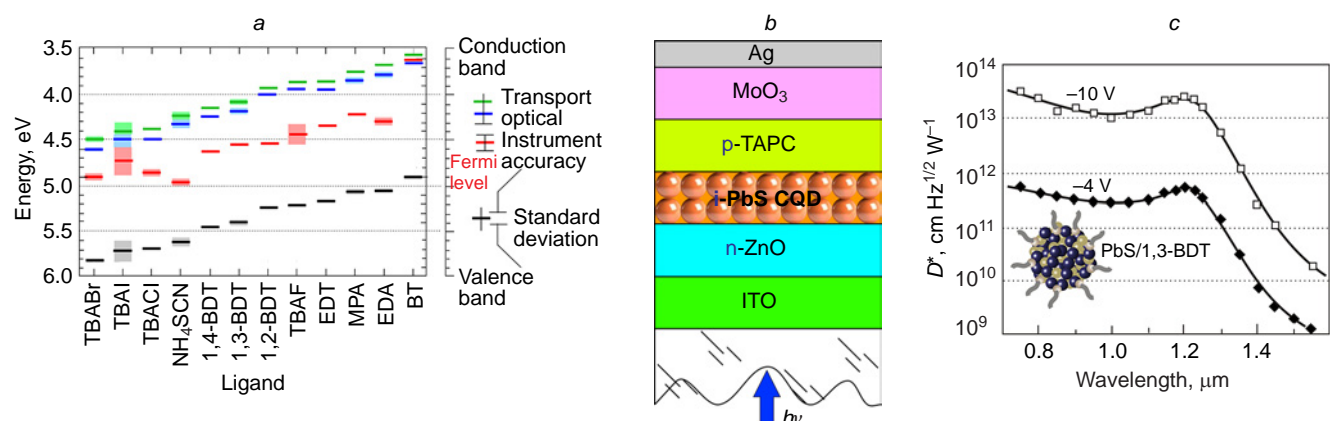
Figure 33. (*a*) Energy diagrams of the PbS CQD layer with various ligands, with the first exciton absorption peak before replacement of oleic acid by an appropriate ligand being at λ = 963 nm in the absorption spectrum of the solution. Each level in the Figure was determined by measuring 2–4 samples; the line width is the deviation from the mean value.[204] (*b*) Architecture of p-i-n photosensor. (*c*) Spectral dependence of the specific detectivity.[205]

Scheme 2
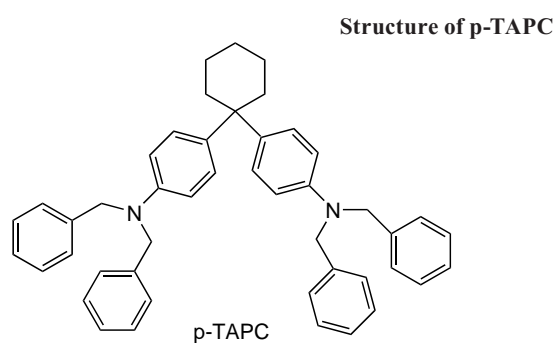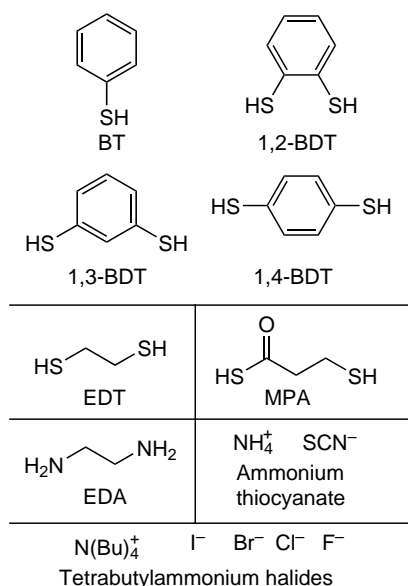
Structure of p-TAPC

SWIR photosensor with i-type PbS CQDs. The photodetector had the structure *Ag/MoO₃/p-TAPC/i-PbS CQDs/n-ZnO/ITO/ glass substrate* (Fig. 33*b*) in which the p-TAPC {1,1-bis[4-(ditolylamino)phenyl]cyclohexane} layer is known as an effective material for hole transport and blocking of the electron current. The n-ZnO layer forms a barrier that blocks the hole current. The MoO₃ layer serves for the transport of holes (extraction of minor carriers from the region in contact with the metal). The p-TAPC and n-ZnO blocking layers decrease the dark current density and provide specific detectivity of approximately 7×10^{13} cm Hz$^{1/2}$ W^{-1} ($\lambda = 1.23$ μm) at room temperature (Fig. 33*c*).

In recent publications, owing to relatively short molecular chains and high affinity to cations on the PbS CQD surface, EDT and TBAI have been more and more often used as ligands in the fabrication of quantum dot layers for solar cells and photosensors.[206, 207] A PbS CQD array passivated by EDT acquires p-type conduction. The PbS CQD array with the TBAI ligand has a clear-cut electron conduction (n-type), owing to the replacement of divalent S²⁻ anions by I⁻.

In PbS CQD arrays, iodine-containing ligands protect lead sulfide nanocrystals from oxidation.[208, 209] Skurlov *et al.*[207]

investigated the properties of PbS CQD arrays passivated by NH₄I, PbI₂ and (Bu)₄NI. Recently, the development of these techniques led to the design of a new type of photodiode structures with an energy barrier at the *p-PbS CQD-EDT/n-PbS CQD-TBAI* contact. The architecture of these photosensors is depicted in Fig. 34*a,b*.[208–210] For optimal layer thicknesses of 40 and 160 nm for p-PbS CQD-EDT and n-PbS CQD-TBAI, respectively, the photodiode *Au/p-PbS CQD-EDT/n-PbS CQD-TBAI/ZnO/ITO* was characterized by specific detectivity of 3.93×10^{13} cm Hz$^{1/2}$ W^{-1} ($\lambda = 0.91$ μm) and 4.52×10^{13} cm Hz$^{1/2}$ W^{-1} ($\lambda = 0.5$ μm) at room temperature under reverse bias of 0.04 V.[208] The responsivity was 385 A W^{-1} ($\lambda = 0.91$ μm) and 444 A W^{-1} ($\lambda = 0.5$ μm). Zinc oxide acted as a barrier blocking the hole current towards the ITO contact, while the p-PbS CQD-EDT layer blocked the electron current towards the Au contact. Photons were mainly absorbed in the n-PbS CQD-TBAI layer.

The architecture of a photosensitive element based on PbS colloidal quantum dots, *AgNW/p-PbS CQD-EDT/n-PbS CQD-TBAI/Ni/Cr*, where NW is nanowire, is shown in Fig. 35*a*.[211] For the fabrication of the n-type PbS CQD layer, the initial ligand (oleate anion) used in the synthesis was replaced by a iodide anion by treatment with TBAI. The p-type conduction was generated by replacing the initial ligand by EDT. Lead chloride (PbCl₂) was used as lead precursor and *N,N'*-diphenylthiourea [SC(NHPh)₂] served as the sulfur precursor. The CQD size (7.6 nm) in the PbS CQD-TBAI(n) layer was greater than the CQD size (3.1 nm) in the PbS CQD-EDT(p) layer, which provided an additional energy barrier between the n- and p-type conduction layers due to different band gap widths

V.P.Ponomarenko, V.S.Popov, I.A.Shuklov, V.V.Ivanov, V.F.Razumov
Russ. Chem. Rev., 2024, **93** (4) RCR5113

25 of 48
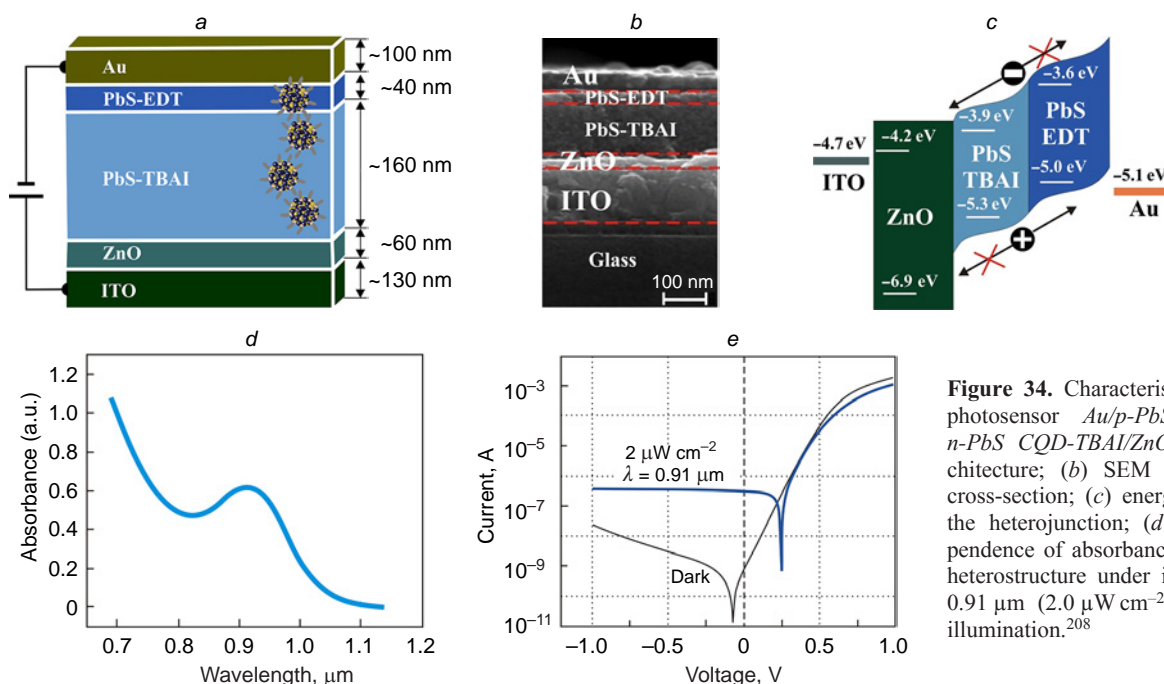
Figure 34. Characteristics of the photosensor *Au/p-PbS CQD-EDT/n-PbS CQD-TBAI/ZnO/ITO*: (*a*) architecture; (*b*) SEM image of the cross-section; (*c*) energy diagram of the heterojunction; (*d*) spectral dependence of absorbance; (*e*) CVC of heterostructure under illumination at 0.91 μm (2.0 μW cm^{-2}) and without illumination.[208]
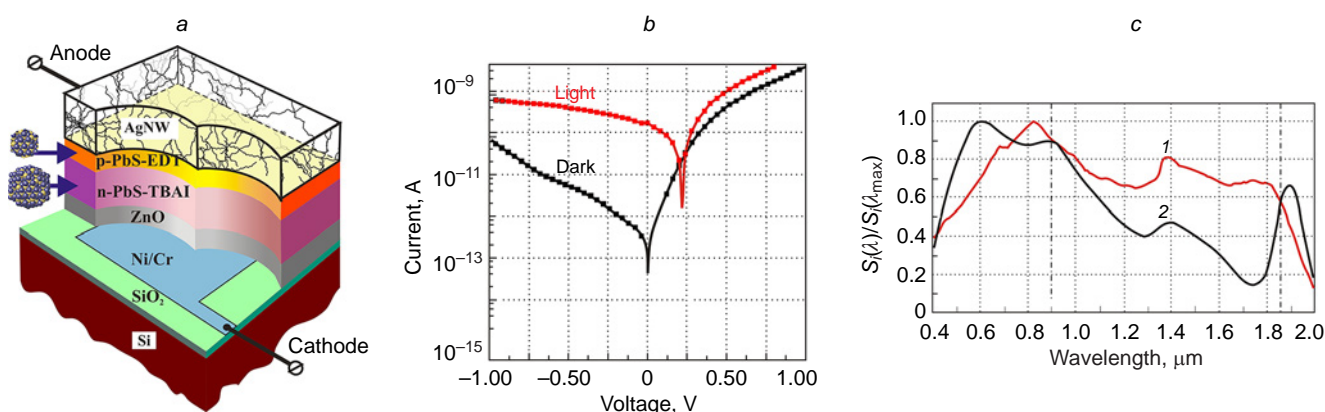
Figure 35. Characteristics of the photosensitive element *AgNW/p-PbS CQD-EDT/n-PbS CQD-TBAI/Ni/Cr*:[211] (*a*) architecture; (*b*) CVC under illumination with an electric filament lamp, incident power of ~3 mW, and without illumination; (*c*) spectral dependence of the relative photosensitivity for (*1*) the sensor architecture shown in inset[211] (*a*) and (*2*) the *PbS/C$_{60}$* architecture on the ROIC surface[76].

and was achieved by varying the synthesis temperature. The n-ZnO nanoparticles of 7–8 nm size were synthesized by the method described by Beek *et al.*[212] As opposed to the studies cited above, the top IR-transparent anode layer was formed by aerosol printing from silver nanowires (AgNWs). They have optical transmittance of about 85–90% in the visible and short-wave IR regions, while having a sufficiently high conductivity, reaching 20–40 Ω m^{-1}.[213] Thus, all functional layers (n-ZnO, n-PbS CQD-TBAI, p-PbS CQD-EDT, anode) were fabricated by liquid colloidal chemistry methods without the use of vacuum or high-temperature processes. The fabricated photosensitive elements had 12×12 μm size. The current–voltage characteristics of the photosensitive elements under illumination (light) or without illumination (dark) are shown in Fig. 35 *b*. The differential resistance of the dark CVC at zero bias for the studied samples is in the range of $(2-20)\times10^{10}$ Ω. The breakdown voltage for various samples is approximately 1.7–2.0 V. The spectral dependence of the relative photosensitivity $S_i(\lambda)/S_i(\lambda_{max})$ is depicted in Fig. 35 *c* (curve *1*), together with that for a sample of the previously described barrier structure based on PbS colloidal quantum dots (curve *2*).[76] The average relative spectral sensitivity $S_i(\lambda)/S_i(\lambda_{max})$ in the wavelength range of 0.9–1.85 μm for the sample studied by Popov *et al.*[211] was 1.5 times as high as that reported previously[76] for PbS CQD barrier nanostructures.

The properties of *Ag/CsPbBr$_3$ CQDs/PbSe CQDs/Ag* and *Au/PbSe CQDs/CdS/CdSe : In/Si* heterostructures are presented in Table 4.[36,70,76,191,192,195,197,199,200,202,205,214,215]

The photosensors with and energy barrier at the contact between two arrays of different colloidal quantum dots of mercury and silver tellurides (HgTe CQDs and Ag$_2$Te CQDs) with the *sapphire/ITO/HgTe CQD/p-Ag$_2$Te NP/Au* architecture were studied by Ackerman *et al.*[192, 193] The spectral sensitivity range was 2–5 μm. The responsivity reached a maximum of 0.56 A W^{-1} at a temperature of 160 K. The specific detectivity under illumination with a 600 °C black body was 2.3×10^{11} cm Hz$^{1/2}$ W^{-1} at $T = 85$ K ($\lambda_c = 4.8$ μm). After thermoelectric cooling (TEC) to 230 K, the specific detectivity decreased to ~10^9 cm Hz$^{1/2}$ W^{-1}, typical of microbolometers.[4]

Table 4. Properties of photovoltaic sensors based on HgTe, PbS and PbSe CQDs [36, 70, 76, 191, 192, 195, 197, 199, 200, 202, 205, 214, 215]

Absorption layer material, energy barrier structure	Active area of the photo-sensitive element	Cut-off wavelength λ_c, sensitivity range $\Delta\lambda$ (μm)	Responsivity S_i, A W^{-1}, at λ or quantum efficiency	Specific detectivity D^*, cm Hz$^{1/2}$ W^{-1}	Tempe-rature, K	Ref.
Sapphire/ITO/Cr/Au/ITO/n-HgTe CQD/НЧ p-Ag$_2$Te/Au (Schottky) PbS CQD diameter of ~8–9 nm	100×200 μm^2	2–5 ($\Delta\lambda$)	1.62 ($\lambda = 4.44$ μm)	3.1×10^8 (no plasm. disk) 7.2×10^8 (plasm. disk) 1.2×10^{11} (no plasm. disk) 4.0×10^{11} (plasm. disk)	300 300 85 85	70
Sapphire/ITO/n-Bi$_2$Se$_3$/HgTe CQDs/p-Ag$_2$Te NPs/HgTe CQDs/ n-Bi$_2$Se$_3$/Au n-p-n type dual-band	–	2.0 (λ_{max}) 5.0 (λ_{max})	0.23 ($\lambda = 2.2$ μm)	SWIR 6.0×10^{10} 1.0×10^{11} MWIR 1.0×10^7 8×10^7 8×10^8 3×10^{10}	300 200 300 250 200 100	191
Sapphire/ITO/HgTe CQDs/p-Ag$_2$Te NPs/Au (Schottky)	–	2.6 (λ_c)	0.7 1.0	1.0×10^{11} ($\lambda = 2.2$ μm) 1.0×10^{10} ($\lambda = 4-5$ μm) 1.0×10^{11} ($\lambda = 4-5$ μm)	300 200 100	192
Au/p-HgTe CQDs/ p$^-$-HgTe CQDs/i- HgTe CQDs/n$^-$-HgTe CQDs/n-HgTe CQDs/ITO/Sapphire	200×200 μm^2	4.4 (λ_c)	2.7	2.7×10^{11} 1.0×10^{11} 1.0×10^{10}	80 200 300	195
PbS/C$_{60}$ on Si ROIC surface (planar heterojunction)	15×15 μm^2	0.3–2.1 ($\Delta\lambda$)	0.10 ($\lambda = 1.9$ μm) 0.17 ($\lambda = 0.6$ μm)	1.0×10^{12} ($\lambda = 1.9$ μm) 1.2×10^{12} ($\lambda = 0.6$ μm) formats:[a] 1920×1080, 640×512, 1280×1024	303	36, 76
Al/ZnO NPs/PbS@CdS/P3HT/ PEDOT:PSS/ITO (planar heterojunction)	9 mm^2	1.45 (λ_c)	600 ($\lambda = 1.4$ μm, $V_{см} = -1.0$ B)	7.4×10^{12} ($\lambda = 1.4$ μm, $V_{см} = -1.0$ B)	300	200
Al/PBDB-T:PBI-Por/PbS CQD-TBAI/PBDB-T:PBI-Por/Al (planar heterojunction)	–	0.4–1.0 ($\Delta\lambda$)	6.32 ($\lambda = 0.63$ μm)	1.12×10^{13} ($\lambda = 0.63$ μm) 4.0×10^{12} ($\lambda = 0.9$ μm)	300	202
Al/PbS CQDs:PCBM:P3HT: ZnO CQDs/ PEDOT:PSS/ITO/ glass (bulk heterojunction)	6.25 mm^2	0.3–1.1 ($\Delta\lambda$)	4.6 ($\lambda = 0.35$ μm) 5.6 ($\lambda = 0.50$ μm) 1.2 ($\lambda = 0.93$ μm)	8.3×10^{11} 1.0×10^{12} 2.3×10^{11}	300	199
Al/PbS CQDs/ITO/glass (Schottky)	1.96 mm^2	0.4–1.8 ($\Delta\lambda$)	45% (295 K) ($\lambda = 0.6$ μm)	1.5×10^{12} ($\lambda = 1.12$ μm) 0.5×10^{12} ($\lambda = 1.45$ μm)	250	197
Ag/MoO$_3$/p-TAPC/i-PbS CQDs/ n-ZnO/ITO/glass	–	0.7–1.6 ($\Delta\lambda$)	–	7.0×10^{13} ($\lambda = 0.7$ μm) 1.0×10^{13} ($\lambda = 1.0$ μm) 4.0×10^{13} ($\lambda = 1.0$ μm) 2.0×10^{10} ($\lambda = 1.6$ μm)	295	205
Ag/CsPbBr$_3$ CQDs/ PbSe CQDs/ Ag/PET	–	0.365–2.0 ($\Delta\lambda$)	7.17 ($\lambda = 0.365$ μm)	8.97×10^{12} ($\lambda = 0.365$ μm)	300	214
Au/PbSe CQDs/CdS/CdSe:In/Si	200×200 μm^2	4.2 (λ_c)	0.36 ($\lambda = 4.2$ μm)	8.5×10^8 ($\lambda = 4.2$ μm)	300	215

Note. [a] Commercial manufacture was started. ROIC is readout integral circuit; ITO is indium tin oxide $(In_2O_3)_{09} - (SnO_2)_{01}$; P3HT is poly(3-hexylthiophene-2,5-diyl); PEDOT:PSS is poly(3,4-ethylenedioxythiophene):poly(styrene sulfonic acid); PBDB-T is poly[(2,6-(4,8-bis(5-(2-ethylhexyl-2-thienyl)benzene[1,2-b:4,5-b']dithiophene)-alt-(5,5-(1′,3′-di-2-thienyl-5′,7′-bis(2-ethylhexyl)benzene[1′,2′-c:4′,5′-c']dithiophene-4,8-dione]; PBI-Por is poly(benzimidazoleporphyrin); PCBM is phenyl-C61-butyric acid methyl ester; TAPC is (1,1-bis[4-(ditolylamino) phenyl]cyclohexane); TBAI is tetra-n-butylammonium iodide; PET is poly(ethylene terephthalate).

The photosensitive structure *Si/Gr/Bi$_2$Se$_3$ NPs/HgTe CQDs/ Ag$_2$Te NPs/Au* was first proposed by Tang *et al*.[216] The photosensor *ITO/n-Bi$_2$S$_3$/HgTe CQDs/p-Ag$_2$Te CQDs/Au* based on analogous types of CQDs and n-Bi$_2$S$_3$ ETL layer provided detectivity of 3×10^{12} cm Hz$^{1/2}$ W^{-1} ($\lambda_c = 2.2$ μm) on cooling to 80 K and 1×10^{11} cm Hz$^{1/2}$ W^{-1} ($\lambda_c = 2.2$ μm) at room temperature.[217]

The photodiode *glass/ITO/LiF/SnO$_2$/PbS CQD-I/PbS CQD-MA/MoO$_x$/Au* (MA is malonic acid) with detectivity of 1.42×10^{12} cm Hz$^{1/2}$ W^{-1} and responsivity of 0.61 A W^{-1} at $\lambda = 1.1$ μm at room temperature was reported by Gong *et al*.[218] The PbS-based colloidal quantum dots had a diameter of 3.8 nm.

Owing to the low density of surface states of 1.21×10^{16} cm^{-3}, the dark current density did not exceed 70 nA cm^{-2}.

The key parameters of photosensors with energy barriers based on PbS, PbSe and HgTe colloidal quantum dots are summarized in Table 4.

5.4. Phototransistors

The field-effect transistors (FETs) based on colloidal quantum dots do not structurally differ from those based on conventional 3D bulk materials. Generally, they can be represented as plane capacitors with a layer of colloidal quantum dots being located

V.P.Ponomarenko, V.S.Popov, I.A.Shuklov, V.V.Ivanov, V.F.Razumov
Russ. Chem. Rev., 2024, **93** (4) RCR5113

27 of 48
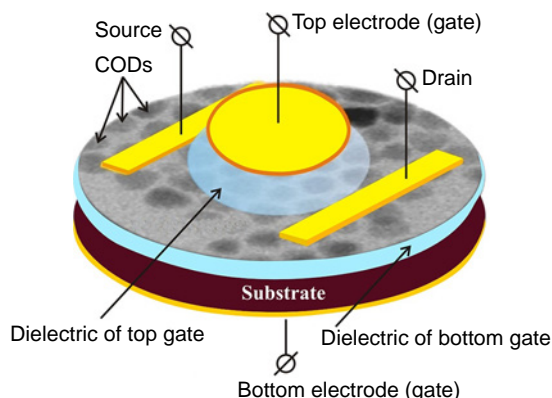
Figure 36. Architecture of a field-effect transistor with a colloidal quantum dot channel and top and bottom field electrodes.

in a dielectric medium between the plates (the top and bottom field electrodes) and acting a conductive channel (Fig. 36). The plates function as a gate that controls the channel conductivity. Field-effect transistors are often used to estimate the mobility of minor charge carriers, since their output characteristics I_{ds} (V_{ds}) in the saturation region are usually adequately described by formulas within the first approximation of the theory of field-effect transistors with an isolated field electrode, according to which [219]

$$I_{ds}(\text{sat}) = \frac{1}{2} C_i \mu^* \frac{Z}{L} (V_{gs} - V_T)^2 \tag{5}$$

$$C_i = \frac{Z \varepsilon_0 \varepsilon_i}{d}$$

where C_i is the specific capacitance of the dielectric of the field electrode (gate); Z and L are the transistor channel width and length, respectively; μ^* is the surface mobility of minor charge carriers in the transistor channel; I_{ds} is the source–drain current; V_{gs} is the source–gate voltage; V_T is the threshold voltage.

The field-effect phototransistors based on colloidal quantum dots studied to date usually make use of hybrid structures consisting of CQD (absorption) layers and functional layers of 2D materials, which give rise to energy barriers and/or transport of photocarriers to the phototransistor drain. These materials include graphene (Gr), black phosphorus (BP) and phosphorene, MoS_2, WS_2, WSe_2, TiO_2 and some other 2D and quasi-2D materials.

The properties of field-effect phototransistors with conductive channels made of HgTe colloidal quantum dots were considered by Chen *et al.*[220] and Huo *et al.*[221] These transistors do not structurally differ from FETs based on other low-dimensional materials and are field-effect transistors with a bottom electrode illuminated from the HgTe CQD layer (Fig. 37).

The specific detectivity of FET with the structure shown in Fig. 37*a* is 2×10^{10} cm Hz$^{1/2}$ W^{-1} at $\lambda = 2.2$ µm and at room temperature.[220] It is lower than that of photodiodes based on HgTe CQDs despite the presence of light signal amplification in the transistor structure. This is apparently caused by relatively high noise of approximately 10^{-11} A Hz$^{-0.5}$, especially at relatively low frequency (10–20 Hz).[220] Markedly higher parameters were implemented in the transistor structures shown in Fig. 37*b*.[221] Unlike the above *Si/SiO₂/HgTe CQDs (/Au)* structure, in this case, the phototransistor with the cut-off wavelength $\lambda = 2.1$ µm is fabricated as the hybrid *Si/SiO₂/MoS₂ (/Au)/TiO₂/HgTe CQDs* including a 2D material (MoS_2) layer and a CQD (HgTe) layer. The TiO_2 buffer layer between
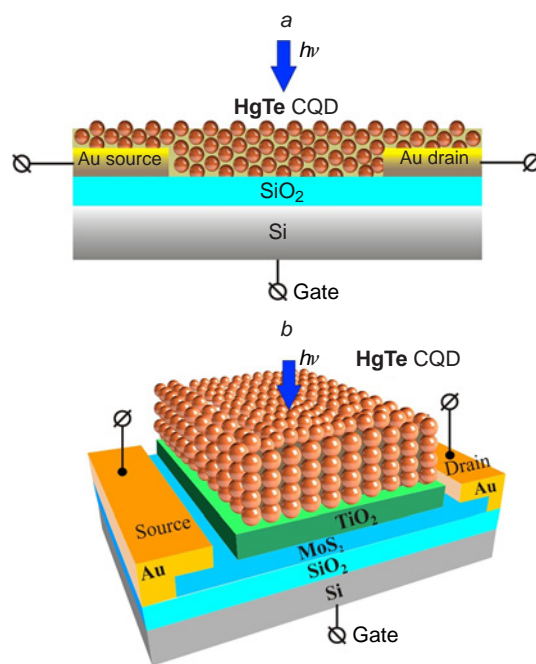
Figure 37. Architecture of field-effect phototransistors: (*a*) based on HgTe CQDs with the structure *Si/SiO₂ /HgTe CQD (/Au)*[220] and (*b*) *Si/SiO₂/MoS₂ (/Au)/TiO₂/HgTe CQD*.[221]

the 2D MoS_2 transport channel and 0D-HgTe CQD absorption layer has an electron type of conduction and serves for the formation of a p-n junction at the *HgTe CQD/TiO₂* interface, which facilitates the transport of charge carriers in the MoS_2 conductive channel. As a result, the dark current modulated by the transistor gate becomes very low ($\sim 10^{-13}$ A Hz$^{-0.5}$ at approximately 10 Hz frequency). In this case, it is possible to implement high responsivity and specific detectivity of approximately 1×10^{12} cm Hz$^{1/2}$ W^{-1} at $\lambda = 2.0$ µm and at room temperaturee.[221] Similar results were obtained by using a new ligand exchange method in which HgTe CQDs with oleic acid residues on the surface were treated with a solution of mercury chloride in a mixture of dimethylformamide, mercaptoethanol, n-butylamine and n-butylammonium chloride, instead of the previously used replacement of the oleate anion by EDT on the surface of the CQD film (see Section 6). This increased the mobility of electrons and holes in the CQD array to approximately 2 and 1 cm^2 V^{-1} s^{-1}, respectively.[222] As a result, the specific detectivity of the *(Si)/SiO₂/HgTe CQDs/PMMA* field-effect transistor (where PMMA is polymethyl methacrylate) (Fig. 38) reached 5.4×10^{10} cm Hz$^{1/2}$ W^{-1} (80 K, $\lambda_c \approx 5$ µm), with the
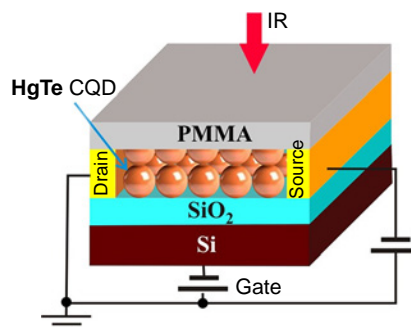
Figure 38. Field-effect transistor (Si)/SiO₂/HgTe CQDs/PMMA.[222]
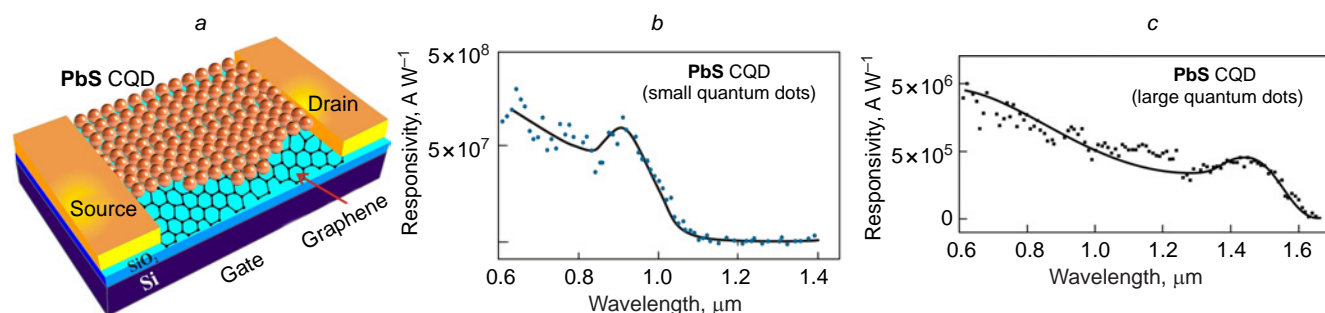
Figure 39. Field-effect phototransistor Si/SiO₂/Gr/PbS CQDs: (*a*) architecture; spectral dependences of the responsivity for transistors based on CQDs with small (*b*) and large (*c*) diameters. Small CQDs have the first exciton absorption peak at 950 nm; for large CQDs, the exciton absorption peak is located at 1450 nm.[223]

responsivity being 0.23 A W^{-1}. The dependence of the specific detectivity on the charge carrier mobility has the form $D^* \sim \sqrt{\mu}$.

The field-effect phototransistors described as *(Si)/SiO₂/Gr/ PbS CQDs and (Si)/SiO₂/Gr/PbSe CQDs*, in which the silicon substrate acts as the field electrode, were reported in a number publications.[223–228] The architecture of a field-effect phototransistor based on PbS CQDs is shown in Fig. 39*a*.[223] The radiation in the 0.6–1.6 µm wavelength range is absorbed in the PbS colloidal quantum dot layer, thus generating electron–hole pairs. The photogenerated holes migrate into the graphene layer and drift towards the transistor drain under the action of the V_{ds} bias voltage applied between the drain and the source, while the photoelectrons remain in the CQD layer. High carrier mobility in the graphene channel (~10³ cm² V^{-1} s^{-1}) provides a relatively high level of photocurrent gain.

The transfer of photogenerated holes to the graphene channel of the transistor is induced by the internal electric field. The time of drift of photogenerated holes τ_{trans} under the action of the field applied between the transistor drain and source is inversely proportional to the hole mobility in the graphene channel. The time during which electrons remain trapped in a colloidal quantum dot layer corresponds, in the order of magnitude, to the lifetime τ_{life} of the charge carriers in PbS CQDs. The gain, which can be described by the τ_{life}/τ_{trans} ratio increases with increasing τ_{life} and decreasing τ_{trans}. The transistor photodetectors had a gain of ~1×10⁸.[223] The spectral dependences of responsivity are shown in Fig. 39*b,c*. The specific detectivity for samples of the detectors is about $(6-7)\times10^{13}$ cm Hz$^{1/2}$ W^{-1}. The product of the G factor by the 10 Hz bandwidth is of the order of 10⁹ Hz.

Sun *et al.*[225] used pyridine (C₅H₅N) as the ligand in the fabrication of the PbS CDT layer, which provided a responsivity of ~10⁷ A W^{-1}. The highest responsivity (~10⁹ A W^{-1}) was attained for the phototransistor *Si/SiO₂/Gr/PbS CQDs* in which a triglycerol:2,3-dimercapto-1-propanol mixture was used as the ligand (0.5 nm long ligand molecule).[226] The detectivity of approximately 1×10¹³ cm Hz$^{1/2}$ W^{-1} and responsivity of 2×10⁶ A W^{-1} were attained in the phototransistor *Si/SiO₂/Gr (/Pd)/PbS CQDs/ITO* with frontal illumination through a conductive ITO layer located above a 300 nm-thick PbS CQD layer. The quantum efficiency was 70% and the photocurrent gain reached 10⁵.[227]

The properties and architectures of the field-effect transistors based on various 2D materials were described by Ponomarenko *et al.*[229,230]

Field-effect phototransistors with an architecture comprising colloidal quantum dots and 2D layers of various materials were studied in a number of publications.[231–238] 2H-Phase bulk or

multilayer dichalcogenides MoS₂, WS₂ and WSe₂ are indirect band gap semiconductors, whereas the monolayer 2D forms are direct band-gap semiconductors with a band gap of 1.9, 2.1 and 1.6 eV, respectively.[13]

Kufer *et al.*[231] described a field-effect phototransistor *Si/SiO₂/MoS₂ (/Ti/Au)/PbS CQDs* in which they used a p-type PbS CQD layer and n-type MoS₂ bilayer. The drain and source electrodes were made of Au/Ti. The architecture of the phototransistors and the energy diagram of the *n-MoS₂/p-PbS CQD* contact are shown in Figs 40*a,b*. The electron–hole pairs photogenerated in the PbS CQD layer are separated by the p-n heterojunction. The electrons move to the n-MoS₂ layer, while the holes remain within the CQD layer. However, unlike the above-described structures using graphene, the current in the channel of MoS₂-based phototransistors can be controlled by varying the gate potential. When a negative voltage V_{gs} is applied to the gate, the MoS₂ layer is markedly depleted in electrons and the channel resistance increases, which ensures a low dark current and increase in the signal-to-noise ratio. This gave a responsivity of ~10⁵ A W^{-1} ($\lambda = 1.0$ µm, Fig. 40*c*) and a specific detectivity of 5×10¹¹ cm Hz$^{1/2}$ W^{-1}. Later, Kufer *et al.*[232] inserted an additional TiO₂ layer, which forms virtually no energy barrier at the contact with n-MoS₂, into the field-effect phototransistor based on p-PbS CQDs (Fig. 40*d*).[232] The high density of localized states at the *n-MoS₂/p-PbS CQD* interface fixes the position of the Fermi level in the band gap of PbS CQDs, thus deteriorating the modulation characteristics of the phototransistor. The insertion of the TiO₂ buffer layer leads to passivation of these states and facilitates the transport of photoelectrons from the PbS CQD layer to the MoS₂ layer (Fig. 40*e*). At room temperature, the described photodetector had a responsivity and a specific detectivity of $(3-15)\times10^2$ A W^{-1} and $(1-5)\times10^{12}$ cm Hz$^{1/2}$ W^{-1}, respectively (Fig. 40*f*).

Field-effect phototransistors *Si/SiO₂/WS₂ (/Ti/Au)/PbS CQDs* and *Si/SiO₂/WSe₂ (/Ti/Au)/PbS CQDs* using tungsten disulfide and diselenide have been reported.[233,234] The higher carrier mobility in these compounds in comparison with MoS₂ makes them promising for the design of field-effect phototransistors. The highest responsivity and specific detectivity were implemented in the Si/SiO₂/WSe₂/PbS CQD structure.[234] The SiO₂ insulating layer was 300 nm thick. The WSe₂ layer with a thickness of ≈0.8 nm, which corresponds to a tungsten diselenide monolayer, was obtained by chemical vapour deposition (CVD). The specific capacitance of the insulating layer was 1.15×10⁻⁸ F cm⁻². The energy diagram of the *n-PbS/p-WSe₂* structure and the spectral and field dependences of the phototransistor are depicted in Fig. 41.
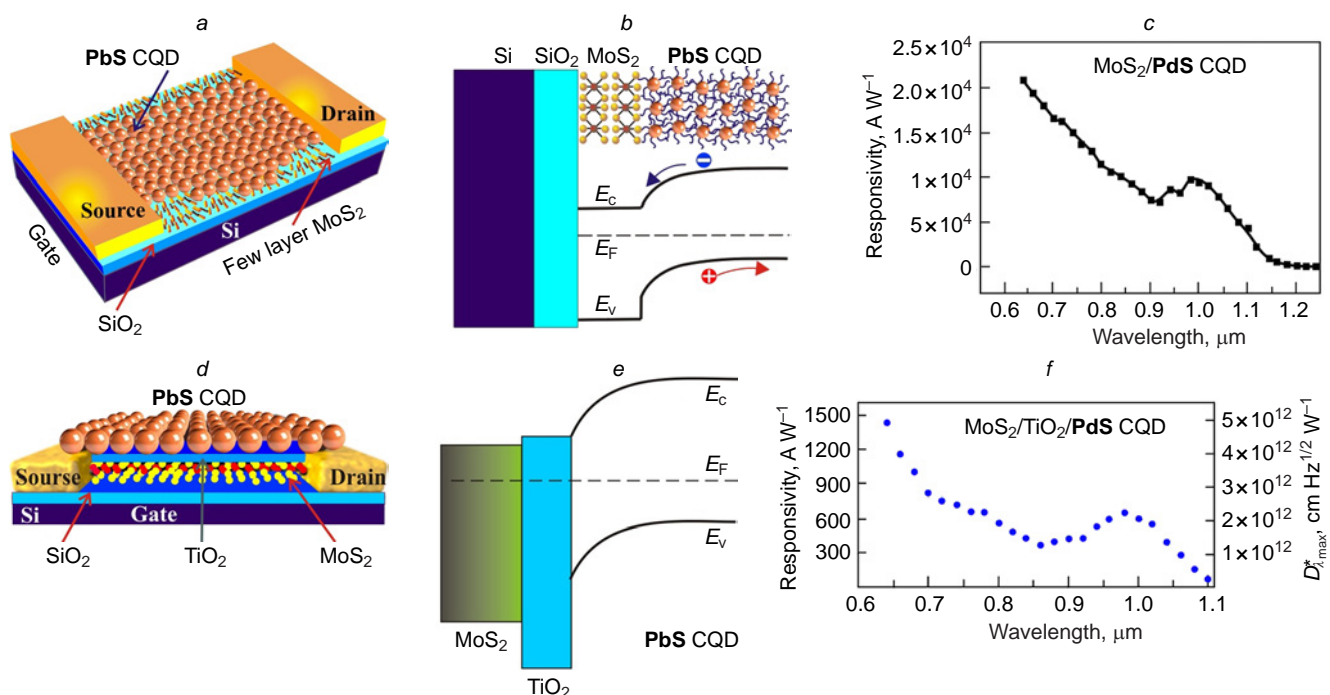
Figure 40. Field-effect phototransistors *Si/SiO₂/MoS₂ (/Ti/Au)/PbS CQDs* (*a, b, c*) and *Si/SiO₂/MoS₂ (/Ti/Au)/TiO₂/PbS CQDs* (*d, e, f*): (*a, d*) photo-FET architectures; (*b, e*) energy diagrams of photo-FET structures; (*c, f*) spectral dependences of the responsivity and specific detectivity of photo-FET.[231,232]

The phototransistor structures *Si/SiO₂/SnS₂/PbS CQDs* and *Si/SiO₂/BP/PbS CQDs* fabricated using two-dimensional sheets of SnS₂ and α-phosphorus [a few black phosphorus (BP) layers] have been reported.[236,237] In the phototransistor with tin disulfide as the field-effect transistor channel, the responsivity and specific detectivity values were 10^6 A W^{-1} and 2.2×10^{12} cm Hz$^{1/2}$ W^{-1} (300 K), respectively. Black phosphorus (BP), or α-phosphorus, is one of the most thermodynamically stable phosphorus allotropes. This is a layered semiconductor with direct band gap of 0.33 eV. A 2D monolayer of black phosphorus, called phosphorene, is also a direct band-gap

semiconductor with a band gap of 1.67 eV. As the number of monolayers increases, the band gap decreases and tends to 0.33 eV. Quasi-2D phosphorene layers can be fabricated by micro-mechanical, liquid-phase or electrochemical cleavage of black phosphorus; CVD method; or etching of a black phosphorus layer in oxygen or argon plasma. Phosphorene has p-type conduction and high mobility of holes at room temperature, which may reach 600 cm² V^{-1} s^{-1} for a monolayer and increase to 4×10^3 cm² V^{-1} s^{-1} for a five-monolayer structure ($E_g = 0.59$ eV).[238] Owing to the semiconductor properties and high hole mobility, phosphorene is promising for the fabrication
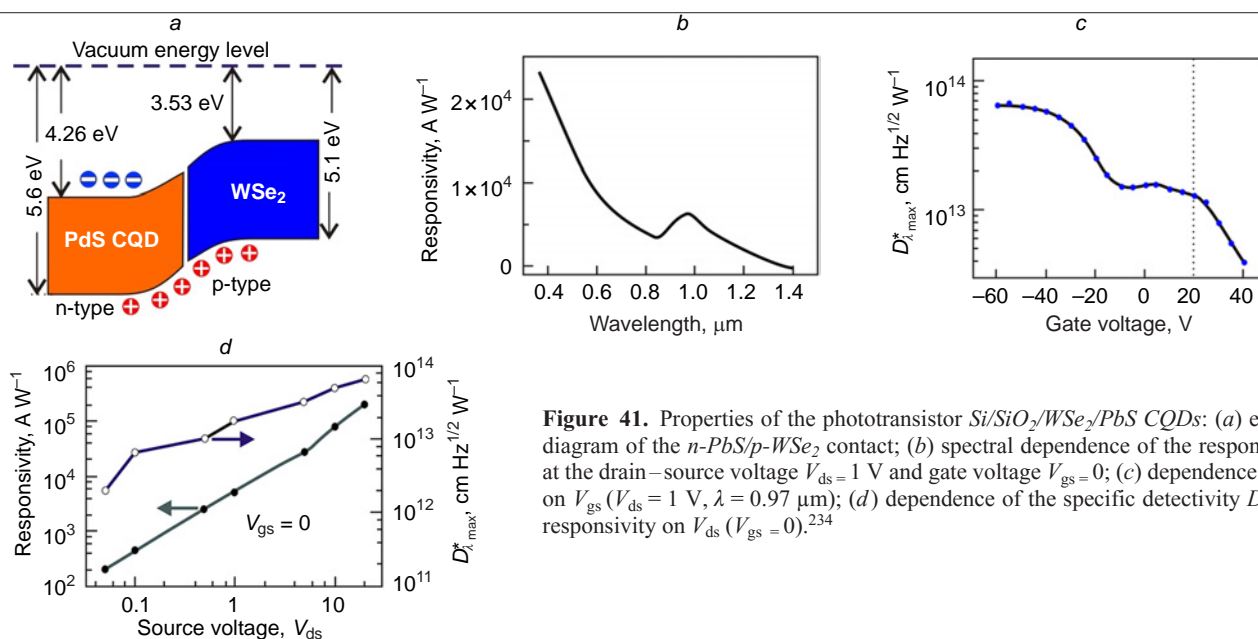
Figure 41. Properties of the phototransistor *Si/SiO₂/WSe₂/PbS CQDs*: (*a*) energy diagram of the *n-PbS/p-WSe₂* contact; (*b*) spectral dependence of the responsivity at the drain–source voltage $V_{ds} = 1$ V and gate voltage $V_{gs} = 0$; (*c*) dependence of D^* on V_{gs} ($V_{ds} = 1$ V, $\lambda = 0.97$ μm); (*d*) dependence of the specific detectivity D^* and responsivity on V_{ds} ($V_{gs} = 0$).[234]

30 of 48

V.P.Ponomarenko, V.S.Popov, I.A.Shuklov, V.V.Ivanov, V.F.Razumov
Russ. Chem. Rev., 2024, **93** (4) RCR5113
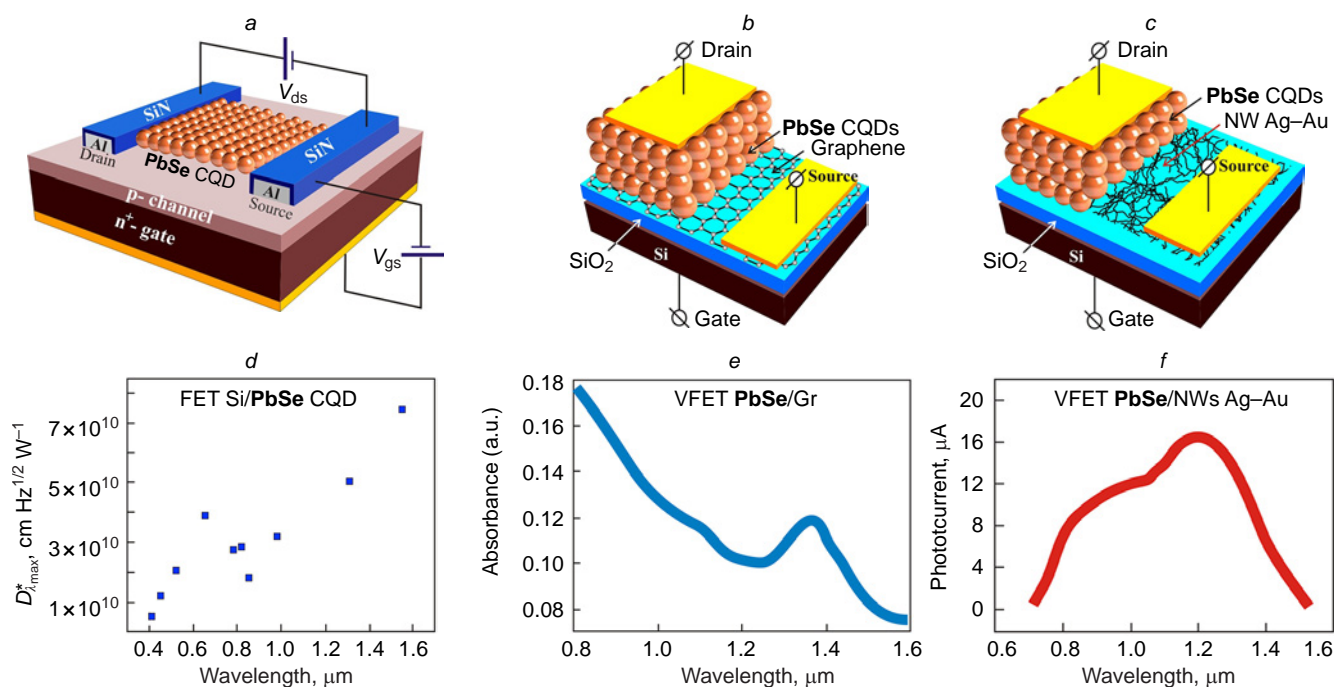
Figure 42. Field-effect transistors based on PbSe CQDs: (*a*) FET with the architecture *(n^+-Si)/SiO$_2$/p-PbSe CQDs/Al/SiN* and (*d*) spectral dependence of the specific detectivity for the transistor;[239] (*b*) FET with the vertical architecture *Au/Gr/((SiO$_2$/n$^+$-Si)/p-PbSe CQDs/Au* and (*e*) FET absorbance;[241] (*c*) FET with the vertical architecture Au/Ag–Au NWs/(*(SiO$_2$/n$^+$-Si)/p-PbSe CQD/Au* and (*f*) spectral dependence of the FET photocurrent for V_{sd} = 1 V, V_g = 1 V.[240] VFET is vertical field-effect transistor.

Table 5. Selected characteristics of field-effect phototransistors based on HgTe, PbSe and PbS CQDs [220–223,227,231,232,235–237,239–241]

CQD FET material	FET architecture	λ_c, µm λ_{max}, µm $\Delta\lambda$, µm	Responsivity S_i, A W^{-1}, at λ (quantum efficiency (%))	Specific detectivity D^*, cm Hz$^{1/2}$ W^{-1}	Ref.
HgTe	*Si/SiO$_2$/HgTe CQDs (/Au)*	2.3 (λ_c)	0.65 (λ = 1.6 µm) 0.30 (λ = 2.2 µm) 0.05 (λ = 2.3 µm)	3.5×10^{10} (λ = 1.6 µm) 2.0×10^{10} (λ = 2.2 µm) 1.0×10^{10} (λ = 2.3 µm)	220
HgTe	*Si/SiO$_2$/MoS$_2$ (/Au)/TiO$_2$/HgTe CQDs*	2.1 (λ_c)	~10^6	1.0×10^{12} (λ = 2.0 µm)	221
HgTe	*Si/SiO$_2$/HgTe CQDs (/Au)*	5.0 (λ_c)	0.2	5.4×10^{10} (λ = 5.0 µm, 80 K)	222
PbSe VFET	*Au/NW Ag–Au/((SiO$_2$/n$^+$-Si)/ KKT p-PbSe/Au*	1.4 (λ_c)	2×10^4	7×10^{12} (λ = 0.81 µm)	240
PbSe VFET	*Au/Gr/((SiO$_2$/n$^+$-Si)/p-PbSe CQD/Au*	1.4 (λ_{max})	1.1×10^4	1.3×10^{10}	241
PbSe Si/n$^+$-p	*(n$^+$-Si)/SiO$_2$/p-PbSe CQD/Al/SiN*	0.41–2.0 ($\Delta\lambda$)	648.7 (λ = 1.55 µm)	7.48×10^{10} (λ = 1.55 µm)	239
PbS	*(Si)/SiO$_2$/Gr/PbS CQDs*	0.6–1.6 ($\Delta\lambda$)	10^7	7×10^{13}	223
PbS	*(Si)/SiO$_2$/Gr/PbS CQDs*	0.6–1.7 ($\Delta\lambda$)	2×10^6 (70%)	1×10^{13}	227
PbS	*Si/SiO$_2$/MoS$_2$ (/Ti/Au)/PbS CQDs*	0.55–1.75 ($\Delta\lambda$)	6×10^5	5×10^{11}	231
PbS	*Si/SiO$_2$/MoS$_2$ (/Ti/Au)/TiO$_2$/PbS CQDs*	0.64–1.1 ($\Delta\lambda$)	10^3–10^5	5×10^{12} (λ = 0.64 µm) 2×10^{12} (λ = 1.0 µm)	232
PbS	*Si/SiO$_2$/WSe$_2$/PbS CQDs*	0.4–1.2 ($\Delta\lambda$)	2×10^5	7×10^{13}	243
PbS	*Si/SiO$_2$/SnS$_2$/PbS CQDs*	0.3–1.0 ($\Delta\lambda$)	10^6	2.2×10^{12}	235
PbS	*Si/SiO$_2$/BP/PbS CQDs*	0.4–1.0 ($\Delta\lambda$)	5.36×10^8	1.89×10^{16}	236
PbS	*Si/SiO$_2$/BP/PbS CQD-EDT/PbS CQD-CTAB*	0.6–1.7 ($\Delta\lambda$)	1.1×10^7	1.75×10^{15}	237

Notes. VFET is vertical field-effect transistor, Gr is graphene, NWs (Ag–Au) are nanowires of the Ag–Au alloy, EDT is 1,2-ethanedithiol, CTAB is the cetyltrimethylammonium bromide, λ_c is the cut-off wavelength, λ_{max} is the maximum sensitivity wavelength, $\Delta\lambda$ is the spectral sensitivity range, BP is multilayer black phosphorus.

of photo-FET. Phototransistor specimens *Si/SiO$_2$/BP/PbS CQDs* showed responsivity and specific detectivity of more than 5×10^8 A W^{-1} and more than 1.8×10^{16} cm Hz$^{1/2}$ W^{-1} (300 K) at gate bias V_{gs} = –90 V, respectively.[236] You *et al.*[237] proposed the

field-effect phototransistor architecture *BP/PbS CQD–EDT/ PbS CQD–CTAB*, where CTAB is cetyltrimethylammonium bromide, which was called a cascade structure. The BP multilayer was obtained by micro-mechanical cleavage of black

V.P.Ponomarenko, V.S.Popov, I.A.Shuklov, V.V.Ivanov, V.F.Razumov
Russ. Chem. Rev., 2024, **93** (4) RCR5113

31 of 48

phosphorus and deposited on an Si/SiO$_2$ substrate. Two PbS CQD layers with EDT and CTAB are located above the BP multilayer. As compared with the transistor *Si/SiO$_2$/BP/PbS CQDs* with only one layer of colloidal quantum dots, in this case, higher responsivity and specific detectivity values of 1.1×10^7 A W^{-1} and 1.75×10^{15} cm Hz$^{0.5}$ W^{-1} (300 K), respectively, were attained.

The transistor structure *(n$^+$-Si)/SiO$_2$/p-PbSe CQDs/Al/SiN* shown in Fig. 42 *a*,[239] which combines the benefits of the silicon photosensorics, which ensures photosensitivity up to cut-off wavelength $\lambda_c \approx 1.1$ µm, with the benefits of the PbSe CQD-based photosensorics, which is able to measure mid-IR radiation, was investigated by Chen *et al.*[239] A responsivity of 648.7 A W^{-1} at 1.55 µm wavelength and a specific detectivity of 7.48×10^{10} cm Hz$^{1/2}$ W^{-1} (300 K) at an external quantum efficiency of 5.2×10^4% were implemented.[239]

Vertical phototransistors based on PbSe colloidal quantum dots have been reported.[240, 241] Unlike the frequently used architectures of field-effect phototransistors, in which the gain is determined by the distance between the source and drain located in one plane, in the vertical FETs, the length of the transistor channels is restricted by only the thickness of the CQD layer and can be minimized. Graphene (Fig. 42 *b*)[241] or Ag–Au nanowires (Fig. 42 *c*)[240] can serve as layers binding the source and drain. Using graphene, a responsivity of 1.1×10^4 A W^{-1} and a specific detectivity of 1.3×10^{10} cm Hz$^{1/2}$ W^{-1} (300 K) were attained under illumination with a 36 mW cm^{-2} laser at 0.808 µm.[241] The vertical architecture was used for the first time in organic field-effect transistors by Ben-Sasson *et al.*[242]

The key characteristics of PbS, PbSe and HgTe CQD-based field-effect transistors are summarized in Table 5.[220–223, 227, 231, 232, 235–237, 239–241]

An attempt to establish an analytical relationship between particular properties of HgTe CQD layers and their macroscopic optical and electrical characteristics was made by Guyot–Sionnest *et al.*,[243] who used barrier structures. Using the measured charge carrier mobilities $\mu_{e,p}$ as functions of temperature and dark current I_0 and photocurrent I under illumination with a calibrated source, the authors determined the charge carrier lifetimes τ and recombination mechanisms for a photoresistor structure based on HgTe CQDs. The use of the analytical expression for D^* obtained by the authors made it possible to determine the maximum possible detectivity, which, as turned out, cannot exceed 1.5×10^8 cm Hz$^{1/2}$ W^{-1} ($\lambda_c = 5.4$ µm) at room temperature under illumination by at black body source at 600 °C. For increasing D^*, the authors[243] proposed to decrease the distance between the photoresistor contacts down to values below 0.6 µm at the same thickness of the photosensitive CQD layer, or to refute the use of the photoresistive effect and switch to CQD barrier structures, which, according to the authors, are more promising for thermal detection.

6. Methods for the synthesis and post-synthetic treatment of CQDs

6.1. Synthetic approaches to the preparation of CQDs

In 1993, Professor Bawendi's research group[30] proposed a high-temperature hot-injection colloidal synthesis that provided the narrowest size distribution of colloidal quantum dots of cadmium chalcogenides. This approach involving temporal separation of nucleation and particle growth phases revolutionized the use of colloidal chemistry techniques to synthesize quantum dots with
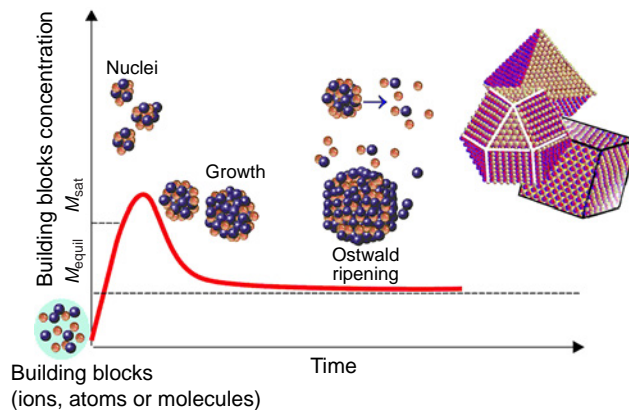
Figure 43. Formation and growth of CQDs. Parameters affecting the growth: temperature, time of growth, surfactants/ligands and surface energy. M_{equil} is the equilibrium concentration, M_{sat} is the concentration upon saturation.

monodisperse size distributions; in 2023, this was acknowledged by awarding the Nobel Prize in Chemistry to Bawendi in a group of authors. Since then, a variety of methods have been applied to the synthesis of metal chalcogenide CQDs, including sol–gel,[244] micellar,[245] hydrothermal,[246] solvothermal[246] and sonochemical[247] methods. However, the best results in the fabrication of photosensor[248] and solar cell[249] structures were attained to date using PbS CQDs and HgTe CQDs obtained exactly by high-temperature colloidal synthesis.[32, 250–252]

According to this method, nanocrystals are prepared by fast injection of the chalcogen precursor to metal precursor at a specified temperature to induce nucleation followed by crystal growth at the same or different temperature.[251] The synthesis takes place in an isolated system in an organic solvent under an inert gas, and the experimental technique is similar to the approaches used in organometallic chemistry.[252] During the synthesis, the surface of the obtained nanocrystals is coated with organic ligands, which increase the aggregative and sedimentation stability of sols and the CQD resistance to oxidation due to steric factors. The particle size is determined by the temperature, reaction time and the concentrations and chemical nature of both precursors (Fig. 43). Characteristic features of Ostwald ripening of CQDs were discussed by Koroleva and Yurtov.[253, 254]

Lead and mercury chalcogenides refer to semiconductor binary compounds of A^{IV}B^{VI} and A^{II}B^{VI} types; however, related approaches are used in their synthesis. Owing to high reactivity of mercury precursors, the synthesis of mercury chalcogenides proceeds at lower temperatures than the syntheses of analogous lead chalcogenides, with chalcogen precursors being the same.

For example, the synthesis of mercury selenide using trioctylphosphine selenide is carried out at 80 °C; the synthesis of lead selenide with the same precursor requires 150 °C.

Below we consider the most important metal and chalcogen precursors used to prepare nanocrystalline materials for photosensitive structures.

6.1.1. Chalcogen precursors

A similar set of chalcogen precursors is used in the synthesis of lead and mercury chalcogenides (selenides, sulfides, tellurides).

6.1.1.1. Sulfides

Traditionally, the following sulfur precursors are used most often to synthesize sulfide nanoparticles:

32 of 48

V.P.Ponomarenko, V.S.Popov, I.A.Shuklov, V.V.Ivanov, V.F.Razumov
Russ. Chem. Rev., 2024, **93** (4) RCR5113

1) thiourea and its derivatives (*e.g.*, thioacetamide);[255, 256]
2) solution of sulfur in oleylamine;[257]
3) bis(trimethylsilyl) sulfide.[258]

Thiourea is a classical precursor in the synthesis of bulk lead sulfide for photoresistors. The preparation of PbS dispersions from thiourea was described in 1961, well before the discovery of quantum-size effect.[259] This reagent is sometimes used as a precursor, but it is poorly suited for the synthesis of colloidal quantum dots with a narrow size distribution.[255] The use of this approach virtually does not allow one to control the stoichiometry (Pb : S ratio) in the nanocrystals. The use of various substituted thiourea derivatives (*e.g.*, those in which some of hydrogen atoms at nitrogen are replaced by butyl and aryl groups) facilitates the size control of the obtained nanocrystals.[256]

The solution of sulfur in oleylamine is relatively stable to atmospheric moisture and oxygen and relatively inexpensive, but has a poorly established variable composition depending on the preparation conditions; therefore, reactions involving this solution can proceed by different mechanisms, which generally reduces the reproducibility of the synthesis.[260] Oleylammonium polysulfides are the major components of the mixture formed upon sulfur dissolution in oleylamine at low temperature (Fig. 44).

Bis(trimethylsilyl) sulfide is preferable in terms of reproducibility of the precursor chemical composition, but it is highly sensitive to moisture and fairly expensive. This precursor has been actively applied since 2003, and currently most of the advanced results on PbS CQD-based photovoltaic solar cells have been obtained using particularly this compound.[155, 258]

$$(Me_3Si)_2S + PbO \longrightarrow (Me_3Si)_2O + PbS_{NP}$$
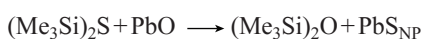
6.1.1.2. Selenides

Tri-n-octylphosphine selenide (TOPSe) is the most frequently used selenium precursor for the synthesis of lead and mercury selenides. As a rule, this reagent is used as a solution in tri-n-octylphosphine and is obtained by dissolution of elemental selenium in trioctylphosphine. Technical-grade tri-n-octylphosphine, used in the syntheses of PbSe CQDs, has variable amounts of impurities including dioctylphosphine and dioctylphosphine oxide and their homologues with a different structure or alkyl chain length.[261] This results in poor reproducibility of the synthesis of selenides with this precursor.
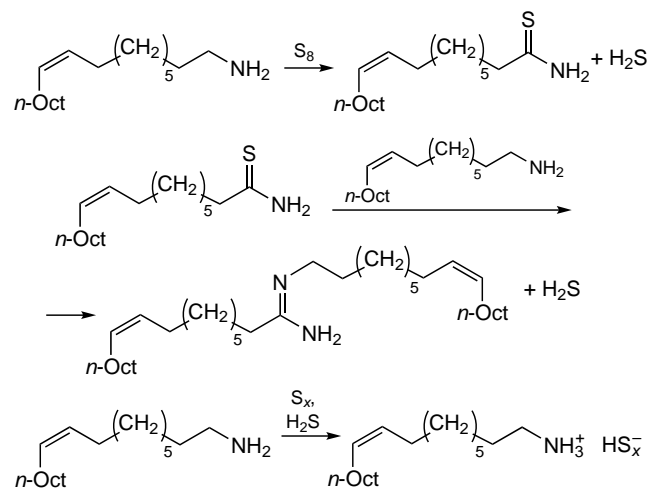
It was shown[261, 262] that the presence of di-n-octylphosphine impurity has an adverse effect on the nucleation. The addition of diphenylphosphine (Ph$_2$PH) was proposed for solving this problem and increasing the reproducibility of the syntheses of selenide nanocrystals.[260, 263, 264] It was found that in the use of this type of TOPSe and Ph$_2$PH mixtures, the equilibrium is always shifted towards the formation of diphenylphosphine selenide (DPPSe).

$$n\,Oct_3P{=}Se + Ph_2PH \longleftrightarrow n\,Oct_3P + Ph_2PSeH$$
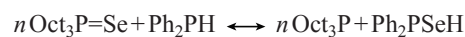
Trioctylphosphine selenide is also actively used in the syntheses of mercury selenide CQDs.[265]

Similarly to the use of a sulfur solution in oleylamine for the synthesis of sulfides, a solution of elemental selenium in oleylamine is sometimes used in the synthesis of selenides. In this case, the products of reaction with selenium are highly different from those obtained with sulfur.[266] Selenium is dissolved at higher temperature than sulfur. This selenium precursor did not find wide use for the synthesis of PbSe CQDs or HgSe CQDs.[141, 267, 268]

The use of bis(trimethylsilyl) selenide in the synthesis of PbSe CQDs was reported in a few studies; however, this reagent is not widely used either because of high cost and high toxicity.[269, 270]

The isolation and application of lead selenide nanocrystals is associated with certain difficulties due to their lower stability to oxidation compared to lead sulfide. For solving this problem, post-synthetic treatment of PbS CQD sols with ammonium halide solutions was proposed. Treatment with solutions of halides, particularly chlorides,[271–273] bromides[162,269] or iodides,[270,274] greatly increases the stability. This does not lead to complete replacement of the initial ligand shell, but only the oleates at the facets more prone to oxidation by air oxygen are replaced. As an alternative to halides, treatment with alkylphosphonic acids was proposed, which increases the oxidative stability of PbSe CQDs.[275]

6.1.1.3. Tellurides

A solution of tellurium in tri-n-octylphosphine (TOPTe) is the most popular precursor in the synthesis of tellurides (Fig. 45). Using this reagent, HgTe CQDs ranging in size from 2 to 200 nm with absorbance up to 65 μm were obtained.[276] The nature of this reagent was investigated only recently.[277,278] Using this reagent, it is possible to obtain lead telluride nanocrystals with sizes ranging from 2.6 to 14 nm.[279] Recently, a related reagent, tricyclohexylphosphine telluride, was proposed as an alternative to TOPTe. This compound makes it possible to obtain stable mercury and lead tellurides.[280]

Unlike sulfur and selenium, elemental tellurium does not react with oleylamine and, as a consequence, no reagent analogous to S or Se solutions in oleylamine is known. The use

Figure 44. Formation of oleylammonium polysulfides upon the dissolution of sulfur in oleylamine at low temperature.
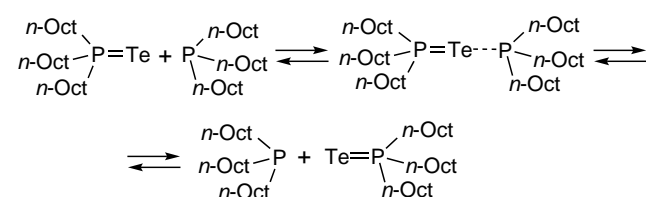
Figure 45. Equilibrium in a tellurium solution in TOPTe at room temperature.

V.P.Ponomarenko, V.S.Popov, I.A.Shuklov, V.V.Ivanov, V.F.Razumov
Russ. Chem. Rev., 2024, **93** (4) RCR5113

33 of 48

of bis(trimethylsilyl) telluride was described in a few syntheses of mercury[281] and lead[269] tellurides. Due to its high cost and low availability, this reagent is not widely used.

6.1.2. Metal precursors

The differences between the reactivities and stabilities of divalent compounds of mercury and lead necessitate the use of substantially different precursors of these two metals.

6.1.2.1. Lead precursors

Two types of precursors are used for the synthesis of lead sulfide and selenide nanocrystals. The first one is lead oleate obtained from lead oxide or acetate in an argon flow to remove the formed water and/or acetic acid.[79] The remaining water or acid can significantly affect the resulting nanocrystals.

$$PbO + 2\,C_{17}H_{33}COOH = Pb(OOCC_{17}H_{33})_2 + H_2O$$

$$Pb(OAc)_2 + 2\,C_{17}H_{33}COOH =$$
$$= Pb(OOCC_{17}H_{33})_2 + 2\,CH_3COOH$$

The second type is a solution of lead chloride in oleylamine.[282] Technical-grade oleylamine, containing also *trans*-isomer, unsaturated amines and short-chain amines are used most often to synthesize CQDs. Solutions of various combinations of lead halides ($PbCl_2$, $PbBr_2$, PbI_2) in oleylamine are known, but they have not become popular. It was shown that oleylamine purity influences the solubility of lead halides and the results of nanoparticle synthesis.[283] The drawbacks of oleylamine as a solvent include very weak coordination on the surface of metal chalcogenide nanocrystals, which leads to oxidation of PbS CQDs during the isolation from the reaction mixture due to ready accessibility of the CQD surface to atmospheric oxygen; one more consequence is increased agglomeration of nanoparticles with the loss of quantum-size effect.

In the synthesis of nanocrystals of a specified size, it is often necessary to prepare precursor solutions of a definite concentration. This problem is addressed using weakly coordinating and non-coordinating high-boiling solvents. Octadecene and diphenyl ether are commonly used solvents for lead chalcogenide precursors.[284,285]

6.1.2.2. Mercury precursors

Mercury telluride is usually obtained using solutions of mercury halides, mainly mercury chloride, in oleylamine.[176,286] Mercury iodide and bromide can also be used, but it is difficult because of their higher reactivity.[274,287,288] The dissolution of mercury halides in dry amines results in the formation of tetrahedral mercury complexes (Fig. 46).[289] Mercury oleate, obtained by dissolution of mercury acetate in oleic acid, is much less commonly used.

The use of octadecene as a solvent for the synthesis of mercury chalcogenides, by analogy with the synthesis of lead

Figure 46. Formation of n-butylamine complex with mercury chloride.[289]

compounds, is hampered by the high reactivity of mercury salts towards alkenes, including octadecene.

6.2. Morphology of lead and mercury chalcogenide nanoparticles

Lead and mercury chalcogenide colloidal quantum dots obtained by high-temperature colloidal synthesis are nano-sized single crystals existing as stable dispersions. Nanocrysta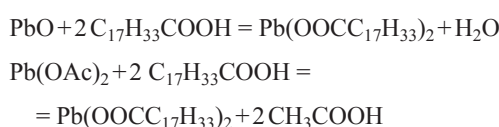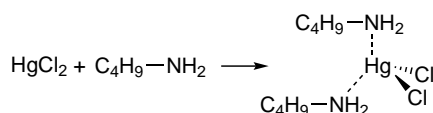ls are highly perfect and rarely show twinning or other defects.[290] The chalcogenide CQDs synthesized by this method have a crystal structure characteristic of bulk crystals of the same chemical composition and faceting clearly seen in SEM images.

Lead chalcogenides (PbS, PbSe and PbTe) do not have allotropes at ambient pressure and crystallize in the cubic lattice, similar to the lattice of halite (rock salt). The interatomic distances are 3.0 Å (PbS), 3.11 Å (PbSe) and 3.23 Å (PbTe).[291] At high pressure, they undergo polymorphic transformation in which the halite lattice is converted to the orthorhombic structure (symmetry group: *P*nma – D2h16).[292–294] Since the high-temperature colloidal synthesis is performed at nearly atmospheric pressure, lead chalcogenide nanocrystals crystallize in the cubic system. Meanwhile, there are published data illustrating significant differences in the shape of PbS, PbSe and PbTe nanoparticles depending on the particle size and synthesis conditions.

During nucleation and growth of lead chalcogenide CQD nanocrystals, two types of crystallographic facets, (100) and (111), may give different contributions to the crystal surface.

Lead chalcogenides differ in the reactivity and affinity to various types of ligands. The surface of (111) facets is formed by Pb^{2+} ions; therefore, these facets have higher surface energy (Fig. 47)[295] and high affinity to coordinating anions able to counterbalance the cation charge, including oleates. For this reason, oleic acid residues bind preferentially to these facets during the synthesis. It was found that alkylamines are preferably coordinated to lead-rich (111) facets.[296]

The surface of (100) facets is a staggered arrangement of alternating lead cations and chalcogen anions. These facets have an affinity to halogen anions (Cl^-, Br^-, I^-).[272] The binding energy of the oleic acid residues to these facets is significantly lower than that to (111) facets; therefore, in the deficiency of halogen anions in the reaction mixture, (100) facets may be virtually not covered by ligands.[295] On the one hand, the absence of ligands on the (100) surfaces may increase the probability of sintering up to the loss of quantum-size effect; on the other hand, the absence of ligands promotes easier oxidation and, as a consequence, the appearance of trap states.[297,298] The control of surface traps is an important task for photosensorics. Therefore, for protection against oxidation and formation of trap states, nanocrystals are obtained with an excess of lead halide precursor or using the post-synthetic treatment of films with solutions of halides or halogens depending on the shape of crystals and the type of predominant surface facets.[299] In view of the above, the efficiency of post-synthetic treatment depends on crystal morphology. Spherical nanocrystals with halogen-rich surface are very stable to oxidation and to the formation of surface traps (Fig. 48).

In general, all lead chalcogenides are prone to oxidation, and the oxidation rate increases in the series PbS – PbSe – PbTe; therefore, the task of selecting growth regimes, procedure of synthesis and post-synthetic treatment methods is important for obtaining CQDs with a small number of surface traps.[300] Depending on the growth conditions, the resulting nanocrystals

34 of 48

V.P.Ponomarenko, V.S.Popov, I.A.Shuklov, V.V.Ivanov, V.F.Razumov
Russ. Chem. Rev., 2024, **93** (4) RCR5113
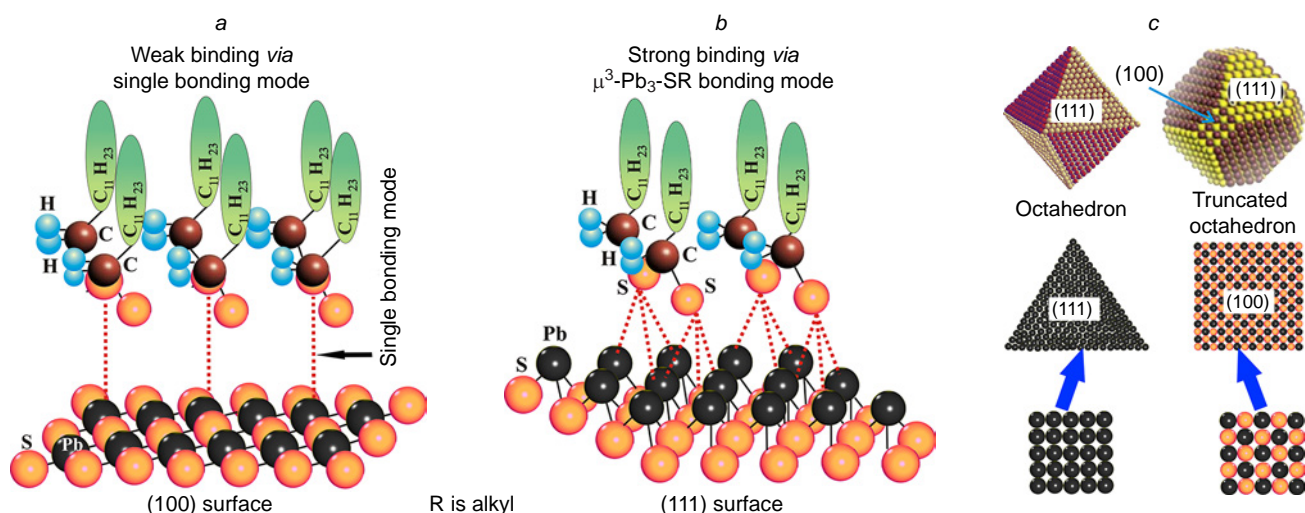
Figure 47. Facet structure in PbS nanocrystals and modes of binding of alkanethiols to the CQD surface: (*a*) μ^3-Pb_3–SR bridging bond on the (111) surface; (*b*) single bond on the (100) surface;[295] (*c*) (111) and (100) facets in PbS nanocrystals.
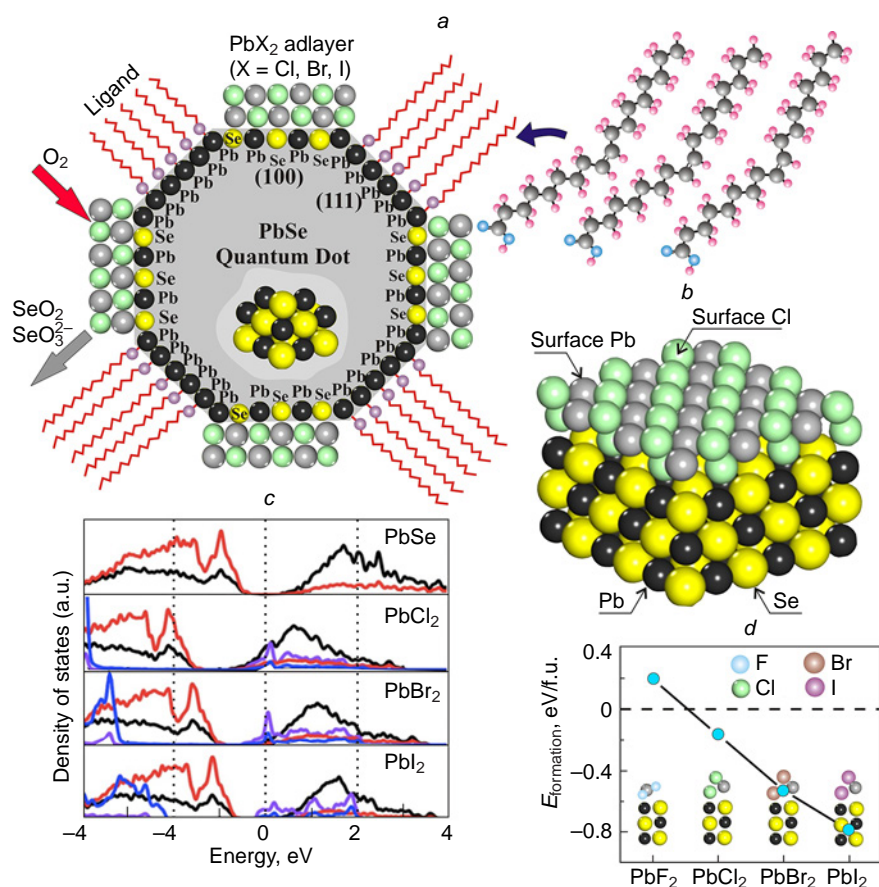
Figure 48. (*a*) Structure of highly stable PbSe CQDs treated with lead halides; (*b*) model of the PbSe(100) surface passivated by $PbCl_2$; (*c*) density of states (DOS) for PbX_2/PbSe(100) (violet is surface Pb; black is bulk Pb; red is Se; blue is halogen X). The zero energy corresponds to the mid-band gap of bare PbSe(100); (*d*) energy of formation of PbX_2 adlayers on the PbSe(100) surface; parts of PbSe CQD(100) cross-section surface-modified by halogens [CQD PbX_2/PbSe(100)].[272]

may be nearly spherical (in the case of isotropic thermodynamic growth), cubic with (100) surface facets or octahedral with (111) surface facets (in the case of anisotropic kinetic growth).[301,302] The concentrations of metal and chalcogen ions play an important role for implementation of a particular growth mode and formation of particles of a definite shape (Fig. 49). Lead chalcogenide nanoparticles may exist as spheres, nanocubes, nanowires, nanorods, octahedra, truncated octahedra and six-pointed stars. The particle morphology affects both the optical properties and conductivity of the resulting layers and the

nanoparticle density in the layer. A nearly spherical shape is typical of lead chalcogenide CQDs of small size.[302] This shape is inherent, most often, in PbSe CQDs with sizes not more than 9 nm. Similarly, in the case of PbS, transition from spheres to nanocubes can be estimated as taking place at the same 9–10 nm, since cube-shaped nanocrystals of 11–15 nm in size are known from the literature.[303–305] In the case of lead telluride, this type of transition supposedly takes place at a diameter of 9–10 nm.[279]

The transition from spherical to cubic and truncated cubic shapes occurs upon further increase in the nanoparticle size. The

V.P.Ponomarenko, V.S.Popov, I.A.Shuklov, V.V.Ivanov, V.F.Razumov
Russ. Chem. Rev., 2024, **93** (4) RCR5113

35 of 48
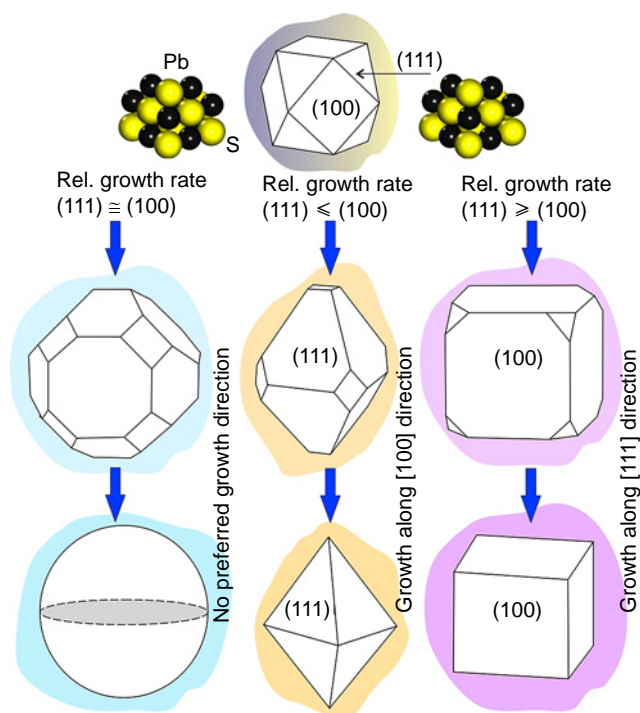
Figure 49. Possible ways of PbS nanocrystal growth: Thermodynamically controlled isotropic growth of spherical nanocrystals with minimum surface energy at high Pb^{2+} concentration (on the left); kinetically controlled anisotropic growth of octahedral nanocrystals, with the surface formed by (111) facets, at low Pb^{2+} concentration (in the middle); kinetically controlled anisotropic growth of cubic nanocrystals, with the surface formed by (100) facets, at low concentration of both Pb^{2+} and S^{2-} ions (on the right).[301]

PbSe nanoparticles with sizes of 14 to 27 nm prepared by the procedure involving n-Oct₃PSe are cube-shaped.[306] It worth to note that nanoparticles that absorb in the near-IR region with cut-off wavelength of 2 µm have a size of 7.5 nm for PbSe and 9 nm for PbS. The change in the ratio between (100) and (111) facets in small and large lead chalcogenide nanocrystals is associated with the problem of ligand exchange in thin layers. This is due to the fact that the facets differ in their chemical nature, and ligand exchange on them occurs at different rates.[307–309]

Most methods of ligand exchange are optimized for small-size PbS nanoparticles, mainly for replacement of oleates by halides on polar (111) facets. These methods are poorly suited for particles of larger diameters.[310,311] Larger PbS nanoparticles are aggregated more readily and even stick together during ligand replacement, as oleic acid residues are readily removed from (100) facets on treatment with polar solvents.[304] Similar problems arise in the case of lead selenide, which, for example, can form honeycomb structures, with particles being stuck together by (100) facets, upon the removal of the oleate shell on treatment with ethylene glycol.[312,313]

A simple or shifted cubic packing is observed in nanocubes assembled on films.[314] Theoretically, these two types of superstructures make it possible to reach the maximum 100% packing density of nanocrystals in the layer.[315]

Lead chalcogenide nanorods are structures with aspect ratio of approximately 3–10, while nanowires are characterized by aspect ratios of more than 10.[316] These related structures are often obtained using similar procedures.

Lead sulfide nanorods (nanowires) can be obtained either by direct synthesis or by cation exchange in existing 1D nanocrystals.[317,318] Lead sulfide nanowires with a diameter of 9 nm were obtained by decomposition of lead thiocarbamate as the only precursor.[319]

Lead sulfide nanorods were prepared by using tris(dimethylamino)phosphine selenide as selenium precursor.[320,321] The aspect ratio in these nanorods can be controlled by varying the rate of hydrolysis of the reactant to the corresponding phosphinite during the reaction.[322] Field-effect transistors with an exciton peak at 1.3 µm were fabricated on the basis of PbSe nanorods.[323] PbSe nanowires are formed as the major structures (more than 95%) at low surfactant (oleic acid) concentrations, high temperature (200–250 °C) and high Pb:Se ratios (1:1 to 3:1). The addition of co-surfactant, hexadecylamine, leads to the formation of zigzag nanowires or stars.[163,324] Similarly to lead sulfide, 9±2 nm-thick lead selenide nanowires with a length of more than 10 µm were prepared by decomposition of lead selenocarabamate as the only precursor.[319]

Even using the same reagents, it is possible to obtain PbSe nanocrystals of different morphology by varying the medium, temperature and oleic acid concentration. Depending on the oleic acid concentration, the growth of PbSe CQD nuclei leads to the formation of nanocubes, octahedra, truncated octahedra or stars (Fig. 50).[163,320] Thus, depending on the particle size, the surfactant/co-surfactant used, the Pb:Se ratio and temperature, it is possible to obtain PbSe nanoparticles of various shapes. Well-formed nanocrystals shaped like truncated octahedra are also known for lead telluride. Using trioctylphosphine telluride, PbTe nanocrystals of this shape with diameters of 28 and 40 nm were obtained.[325] Nanoparticles of similar shapes are also known for PbS with a size of approximately 10 nm.[326]

Lead sulfide nanostars are obtained using a combination of cationic (*e.g*., CTAB) and anionic (*e.g*., sodium dodecyl sulfate) surfactant in an aqueous solution at 80 °C.[327,328] The obtained PbS nanocrystals are well-formed six-pointed stars with arms oriented along the (100) facets. Abu-Hariri *et al*.[329] studied the mechanism of PbS nanoparticle growth for the hydrothermal synthesis based on lead acetate (Fig. 51). The growth of pods is faster from the (100) facets, while (111) facets grow after longer time, and the nanocrystal acquires an octahedral shape.
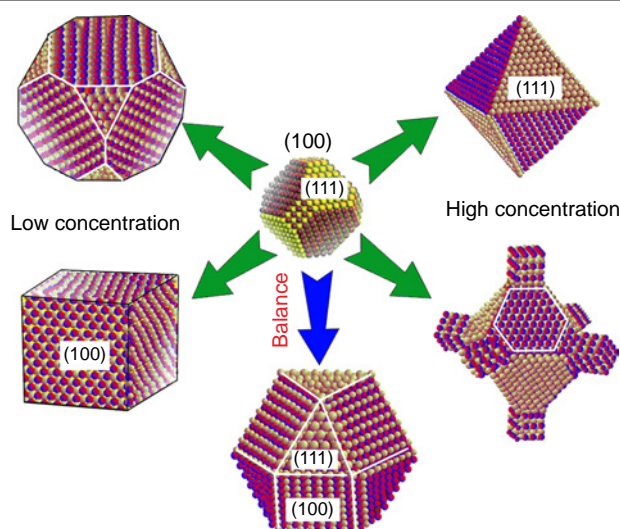
Figure 50. Diagram of the influence of oleic acid concentration on the growth of PbSe CQD nuclei.[163]

36 of 48

V.P.Ponomarenko, V.S.Popov, I.A.Shuklov, V.V.Ivanov, V.F.Razumov
Russ. Chem. Rev., 2024, **93** (4) RCR5113
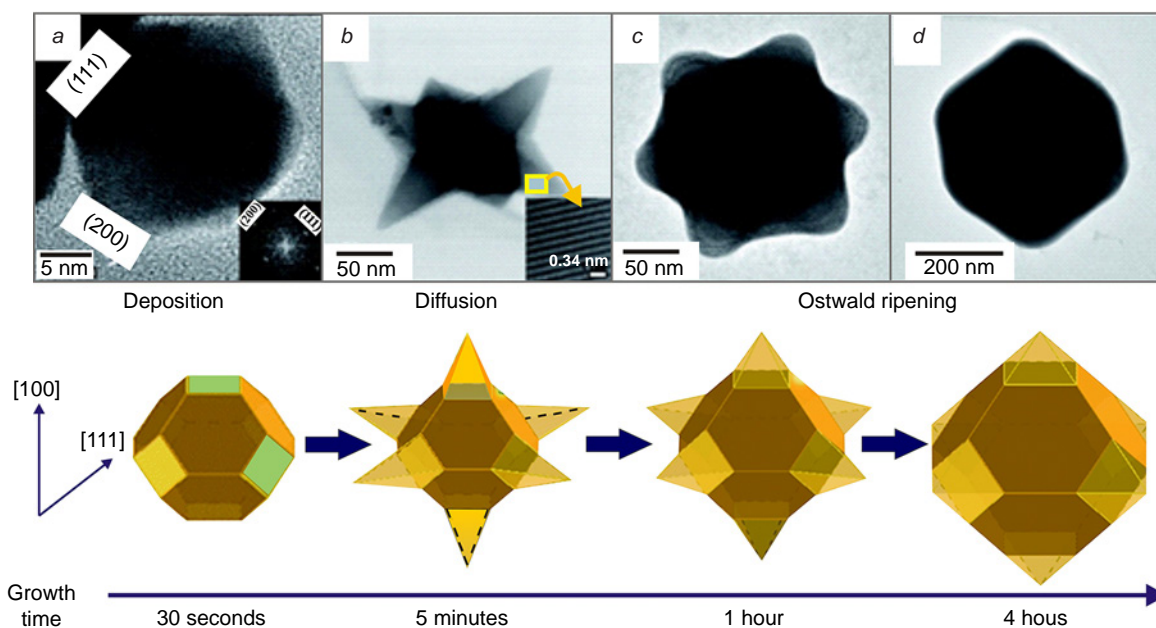
Figure 51. Effect of the growth time on the morphology of PbS CQDs.[329]

PbS nanoflowers of 35 nm in size at room temperature were obtained by the reaction of a solution of lead oxide in oleic acid with a solution of sulfur in oleylamine.[330]

The major polymorph of mercury telluride crystallizes in the cubic system corresponding to space group F43m.[331] Similarly to lead chalcogenide nanocrystals, mercury telluride CQDs with small diameters are spherically shaped. As HgTe nanocrystals grow, they turn into tetrahedra, which often stick together with one of the facets.[332]

6.3. Hybrid procedures

Recently, a large (640×512) photodetector with high detectivity characteristics $(D^* = 2.1 \times 10^{12}$ cm Hz$^{1/2}$ W^{-1} in the $0.4-1.3$ μm range) based on lead sulfide CQDs was manufactured.[35] Colloidal quantum dots were prepared using an original procedure that implied controlled ion exchange of Cd^{2+} ions in CdS CQDs with Pb^{2+} ions; this process was combined with Ostwald ripening.[333,334] Lead chloride mixed with oleic acid served as the lead precursor, while as the sulfur precursors, large (~5 nm) CdS CQDs were used in the initial stage (ion exchange) and smaller (~1.5 nm) CdS CQDs or TOPS were used at the PbS CQD growth stage. A similar synthesis was performed for PbSe CQDs. The relatively large PbS CQDs (8.5 nm) and PbSe CQDs (6.5 nm) obtained in this way had a nearly spherical shape and were coated by oleic acid residues and chloride ions.

6.4. Formation of CQD layers and the influence of ligands

Oleic acid residues, which form the ligand environment on the CQD surface and provide long-term aggregative stability and oxidation resistance, have an adverse effect on the formation of CQD layers for photosensor applications. In the layer, these large ligands isolate single quantum dots from one another and thus hinder the transport of photoinduced charge carriers. The main approach to eliminate this difficulty is to replace the long-chain aliphatic ligands by small ligands such as halide ions or

short molecules such as thiols (ethane-1,2-dithiol is used most often) and so on.

Currently, two main strategies, conventionally called solid-state and liquid-phase ligand exchange, are used to form CQD layers suitable for the design of photosensor structures (Fig. 52).[335]

The solid-state ligand exchange is a two-stage process of ligand replacement in thin films consisting of one or more CQD layers. The process includes deposition of a sol of quantum dots with long-chain ligands onto a substrate to form a CQD layer followed by treatment with a solution containing short-chain ligands (*e.g.*, halogen ions or thiols). The fabrication of thicker layers by this technique is a multi-stage process in which the two above stages are repeated until the desired CQD layer thickness is achieved. The gaps arising in the single CQD layers after replacement of long-chain ligands by shorter ones are healed upon deposition of the subsequent layers.

The alternative liquid-phase exchange strategy implies a ligand exchange reaction in solution, which results in the formation of a CQD sol with shorter ligands on the surface. Sols of this type are generally less aggregatively stable than the traditional systems with long-chain ligands, but thorough selection of solvents and stabilizing agents may result in a fairly high stability. These sols are applicable for deposition of layers
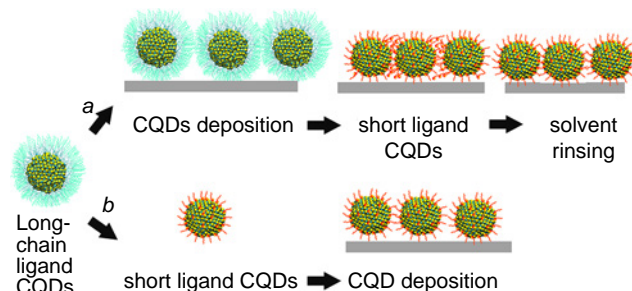
Figure 52. Ligand exchange strategies on the CQD surface: (*a*) solid-state exchange; (*b*) liquid-phase exchange.[335]

V.P.Ponomarenko, V.S.Popov, I.A.Shuklov, V.V.Ivanov, V.F.Razumov
Russ. Chem. Rev., 2024, **93** (4) RCR5113

37 of 48

by various methods (spin-coating, aerosol printing, *etc*.) and do not require post-treatment. In the case of aerosol printing, these sols are called ink and are deposited on the surface in one cycle, thus forming a CQD layer with a specified thickness and topology. In addition, using this approach, so-called bulk homojunction was implemented for the first time for CQDs. In this case, the photosensitive layer is formed by the ink obtained by mixing n- and p-type CQD inks. This approach may improve the charge carrier extraction efficiency.[336]

Meanwhile, lately, approaches combining both strategies have been often used, for example, deposition of HgTe CQD ink layers followed by the solid-state treatment with ethane-1,2-dithiol, since the presence of two terminal thiol groups in ethanethiol allows for bridging of neighbouring CQDs and enhances the layer continuity and electrophysical properties.[195] Apart from the direct layer densification and removal of barriers between particles, it turned out that ligand replacement is highly important for doping of CQDs and affects the band structure and charge carrier type, mobility and concentration (Fig. 53).[337–339]

Doping of colloidal quantum dots is determined by the following parameters:

— metal to chalcogen stoichiometry in CQDs during the chemical synthesis,

— chemical modification of the CQD surface during ligand replacement,

— modification of the CQD surface under the action of atmospheric oxygen,

— bulk doping of CQDs during chemical synthesis.

An important factor for the formation of the conduction type in CQDs is the metal to chalcogen stoichiometry, which considerably affects the properties of chalcogenides.[340] An excess of metal in CQDs leads to n-type conduction, while an excess of chalcogen results in p-conduction (Fig. 53 *b*).[128,341]

An actively developing method for targeted modification of the electrophysical properties of CQD layers is the change in the CQD ligand environment called ligand engineering.[335,338] Talapin and Murray [342] found for the first time that the hydrazine-treated PbSe CQD films have n-type conduction, which can switch to p-type after keeping in vacuum or heat treatment.

Zhitomirsky *et al*.[343] showed for the first time that the presence of halide anions on the PbS CQD surface leads to n-type conduction. Therefore, by using surface doping, it is possible to deliberately generate CQD layers based on the same material with opposite types of conduction for the formation of p–n junction in CQD-based structures. Bederak *et al*.[344] and Tang *et al*.[345] investigated the effect of halide ligands on the optical and electrophysical properties of PbS CQD films. Using chemically different ligands, it was possible to specify the concentration and type of major charge carriers (Fig. 53 *a*,*c*).[337,339] In addition, ligand replacement induces considerable changes in the mobility of charge carriers in CQD
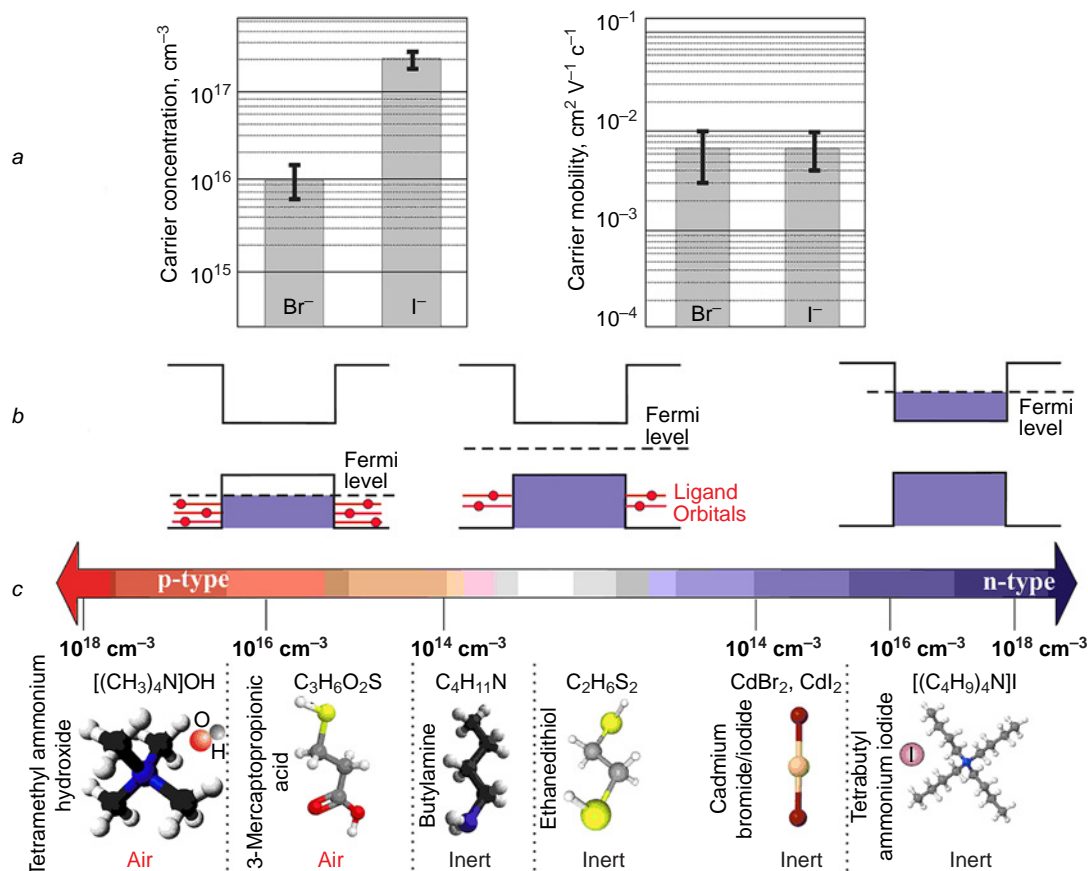
Рисунок 53. (*a*) Concentration of the dopant (on the left) and carrier mobility (on the right) in PbS CQD films treated with tetramethylammonium bromide and iodide;[337] (*b*) n-doping by using excess Pb, resulting in the Fermi level being located near the conduction band maximum (on the right); shift of the Fermi level to the mid-band gap due to increasing number of surface ligands (at the centre); further shift of the Fermi level towards the valence band with formation of free holes due to additional anionic ligands (on the left);[338] (*c*) effect of PbS CQD surface treatment with different compounds on the concentration of dopants (treatment conditions are indicated below).[339]

films, which is of great importance for the operation of photodetectors. Furthermore, ligand replacement leads to significant changes in the mobility of charge carriers in CQD films, which is of great importance for the operation of photodetectors. Some studies indicate that PbS CQD films treated with ethane-1,2-dithiol have a hole conductivity of approximately 1×10^{-4} cm^2 V^{-1} s^{-1}, whereas films treated with tetra-n-butylammonium iodide have a much higher electron mobility of 2.1×10^{-2} cm^2 V^{-1} s^{-1}.[344,346] Martinez *et al.*[347] studied the effect of ligands on the charge carrier mobility in HgTe layers and demonstrated that the mobility increases in the series SCN$^-$<octane-1-thiol<Cl$^-$<butane-1-thiol<1,4-dimer-captobenzene<ethane-1,2-dithiol<As$_2$S$_3$<S^{2-}. Chen *et al.*[348,349] reported a hybrid procedure that allowed for a considerable increase in the charge carrier mobility in HgSe from 10^{-2} cm^2 V^{-1} s^{-1} to 0.9 cm^2 V^{-1} s^{-1}. The recent advances in the development of hybrid ligand exchange methods provided not only n-type but also p-type carrier mobility in the HgSe CQD layers at 1.0 cm^2 V^{-1} s^{-1}.[350] This hybrid procedure included three stages: (1) liquid-phase ligand exchange (oleylamine on the CQD surface was replaced by β-mercaptoethanol); (2) liquid-phase treatment [with a mercury(II) chloride solution for n-type CQDs and with an ammonium sulfide solution for p-type CQDs]; (3) solid-state exchange (a layer of quantum dots deposited on the substrate was treated with a mixture of ethane-1,2-dithiol and hydrochloric acid in isopropyl alcohol).

Depending on the ligand type and donor-acceptor properties, the ligands affect the energy structure of CQDs. In particular, it was shown that the use of different ligands for replacement of oleic acid on the same PbS CQDs results in a shift of the band gap and Fermi level (see Fig. 33 a).[204]

An important issue is the effect of oxygen as a doping impurity on the CQD properties. The PbS CQD layer obtained under inert atmosphere, which has n-type conduction due to non-stoichiometry, acquires p-type conduction when kept in air.[351] Similarly, n-PbS CQDs (which have electron conduction after treatment with tetra-n-butylammonium iodide) switch to p-type conduction upon treatment with amines in air.[339] The targeted treatment with oxygen plasma affords n-type PbS CQD layers for solar energy production, as it enhances layer stability and increases the energy conversion factor by several percent.[352] Meanwhile, as mentioned above, the oxidation of CQD surface gives rise to traps that increase the dark current and noise in photosensitive structures.[298,353]

Sun *et al.*[354] showed experimentally that OH groups and CQD dimers (CQDs fused together) are the sources of traps in CQDs.[354] The ligand exchange procedure reported in this study markedly reduces the formation of traps in PbS CQDs.

Apart from the considered approaches related to surface modification of CQDs, the possibility of classical bulk doping of lead chalcogenide CQDs has been reported. Previously, it was believed that in the synthesis of small semiconductor nanocrystals, bulk doping, well developed in classical microelectronics for bulk and epitaxial materials, is hampered in the case of CQDs due to the self-cleaning effect, *i.e.*, fast migration of dopant atoms on the nanoparticle surface.[355] However, synthetic approaches to address this challenge have been developed; this was demonstrated by manganese doping of CdSe CQDs and ZnSe CQDs.[356] A publication of 2013 is devoted to minor bulk doping of PbSe CQDs with silver in which the carrier mobility and concentration changed only slightly after doping.[357] In the same year, successful bulk doping of PbS CQDs with bismuth with a concentration of free electrons greater than 10^{17} cm^{-3} was demonstrated, with the exciton absorption peak shifting to the higher energy with increasing bismuth content.[358]

7. Optoelectronics based on PbS CQD detector arrays

The most significant results on the design of optoelectronic devices as night vision cameras for short-wave IR range of 0.4–2.0 μm based on photodetector arrays were obtained using PbS CQDs. These cameras were developed for the 640×512, 1280×1024 and 1920×1080 formats (15 μm pixel pitch).[36,76,359,360] The main characteristics of night vision cameras attained to date are summarized in Table 6.[36,76,359,360]

8. Conclusion

The search for alternative approaches to the creation of the element base of infrared optoelectronics has resulted in recent years in the formation of a new subject in science and engineering: photosensorics based on low-dimensional materials and structures. They include structures based on 0D materials, graphene, graphene-like and non-graphene 2D-materials, topological insulators, type II composite superlattices, *etc.* The properties of many of these materials eliminate the drawbacks and engineering difficulties typical of photosensorics based traditional 3D materials and structures, which is analyzed in Section 2.

The most significant results and their practical implementation described in Sections 3, 5 and 7 of the review have been attained using CQD-based short-wave photosensors (0.4–2.0 μm). In the 2020s, the manufacture of uncooled PbS CQD photodetector arrays, including 1280×1024 and 1920×1080 mega-pixel formats; photovoltaic devices with energy barrier at the C$_{60}$/PbS CQD interface in which the percentage of operating photosensitive elements is 99.9–99.95%, quantum efficiency reaches 45% at 1.55 μm and the specific detectivity reaches

Table 6. Properties of optoelectronic night vision devices (NVD) based on PbS colloidal quantum dots.

NVD characteristics	Value	
Array format	1920×1080	640×512
Pixel pitch, μm	15×15	20×20
PSE unit size, mm	28.8×16.2	12.8×10.24
Number of operative PSE (%)	99.5	99.9
Spectral range, μm	0.4–2.1	0.4–2.0
Method of operating temperature stabilization	one-cascade thermoelectric cooler	two-cascade thermoelectric cooler
Operating temperature, °C	$-20 - +55$	$-40 - +55$
Dynamic range, dB	70	120
Frame rate , cadre/s	30–60	86–96
Dimensions, cm	$6.1 \times 6.1 \times 13.2$ $6.1 \times 6.1 \times 10.3$	$16.87 \times 10.2 \times 11.15$
Weight, kg	0.594	1.35
Power supply, V	6–16 (DC)	11–13 (DC)
Power consumed, W	6.5 (40 °C)	–
Interface	Gige Vision	Gige configuration Camera Link
Refs	36, 76, 360	359, 360

V.P.Ponomarenko, V.S.Popov, I.A.Shuklov, V.V.Ivanov, V.F.Razumov
Russ. Chem. Rev., 2024, **93** (4) RCR5113

39 of 48

1.0×10^{12} cm Hz$^{1/2}$ W^{-1} ($\lambda = 1.9$ μm) at room temperature. In the number of photosensitive elements, these photosensors have already caught up with the photodetector arrays based on epitaxial 3D layers of InGaAs. In addition, the CQD-based arrays do not require integration with ROIC by indium bumps, which markedly facilitates the technology. This crucially reduces the cost of photodetector arrays. A pixel pitch for photosensitive elements for CQD-based photodetector arrays is limited only by the pitch that can occur in ROIC. Readout integrated circuits implementing a pixel pitch of 1.82 μm and 1.62 μm have already been demonstrated in the market. This actually makes colloidal quantum dot photosensors for $0.4-1.55$ μm range second to none among devices based on conventional 3D materials.

Using full-format PbS CQD-based arrays with 640×512, 1280×1024 and 1920×1080 elements, infrared night vision cameras with a cut-off wavelength extended up to $2.0-2.1$ μm compared to electro-optical transducers have been developed have become commercially available.

There exist a number of new architectures of IR photosensors using photoresistive, photovoltaic and phototransistor structures containing PbS, PbSe, HgTe and HgSe colloidal quantum dot arrays and functional layers of various, including 2D, materials. The highest specific detectivity values of 2.7×10^{11} cm Hz$^{1/2}$ W^{-1} ($\lambda = 4.2$ μm, $T = 80$ K), close to the maximum achievable values for background limited infrared photodetectors, have been described for the few-element photovoltaic devices in $3-5$ μm spectral range, with the gradient structure *Au/p-HgTe CQDs/p$^-$-HgTe CQDs/i-HgTe CQDs/n$^-$-HgTe CQDs/n-HgTe CQDs/ITO/sapphire*, using three-stage ligand exchange for the fabrication of the photosensitive elements.

When the review was prepared for publication, Wang *et al*.[361] described a SWIR photosensor based on Ag$_2$Te CQDs with the architecture *glass/ITO/SnO$_2$/AgBiS$_2$ CQDs/Ag$_2$Te CQDs/Au*. The specific detectivity of the photosensor over a broad wavelength range ($0.35-1.6$ μm) at room temperature is approximately 1×10^{12} cm Hz$^{1/2}$ W^{-1} and reaches a maximum of 3×10^{12} cm Hz$^{1/2}$ W^{-1} at $\lambda = 1.35$ μm. The authors continued the search for barrier type photosensor architectures (see Section 5.3); a distinctive feature of the authors' solution is the absence of heavy toxic metals (Pb, Hg).

Current studies address the theoretical issues of the structure of the energy spectrum, conduction mechanisms in quantum dot arrays with typical sizes of $3-10$ nm, the effect of ligands on transport phenomena, the effect of disorder in the CQD arrays caused by differences in size, distance and number of donors; these studies are described in Section 4. It has been shown that the theoretical descriptions of the electron transport mechanisms in metal and semiconductor CQDs are considerably different. The conduction mechanism in semiconductor CQD arrays requires additional investigation.

The methods for the synthesis and post-synthetic treatment of CQDs (Section 6) are being improved. The change in the ligand environment of CQDs called ligand engineering considerably affects the electrophysical properties of CQD arrays, which determine the photosensor characteristics. The sources of traps in CQDs are OH groups and CQD dimers, which increase the dark current and noise in photosensitive structures. A ligand exchange procedure markedly reducing trap formation in PbS CQDs is described.

The key challenges that should be solved to significantly accelerate the development of CQD-based photosensorics include: (a) search and development of a procedure for post-synthetic ligand exchange to increase the mobility of charge carriers formed after decay of photoexcitons, in particular using core@shell structures; (b) development of aerosol printing technique for photosensitive and functional layers based on colloidal quantum dots such as PbS, HgTe, PbSe, Ag$_2$Te, ZnO, MoO$_x$, and NiO$_x$ CQDs; conductive coatings optically transparent in the IR range based on nanowires (Ag, Au, Ag$-$Au alloy and so on.) and protective and passivating coatings ensuring long-term stability of IR photosensor parameters; (c) search for CQD architectures and materials to provide high MWIR and LWIR sensor characteristics at elevated temperatures up to room temperature; (d) development of architectures and technologies for the fabrication of multispectral and full-format CQD-based photosensor arrays.

9. List of abbreviations and designations

The following abbreviations, designations and symbols are used in the review:

1,2-BDT — benzene-1,2-dithiol;
1,3-BDT — benzene-1,3-dithiol;
APD — avalanche photodiode;
BB — black body;
BCP — 2,9-dimethyl-4,7-diphenyl-1,10-phenanthroline (bathocuproine);
BLIP — background limited infrared photodetector;
BP — black phosphorus;
BT — benzenethiol;
CBM — conduction band minimum;
CQD — colloidal quantum dot;
CTAB — cetyltrimethylammonium bromide;
CVD — chemical vapour deposition;
EBL — electron blocking layer;
EDA — ethylene-1,2-diamine;
EDT — ethane-1,2-dithiol;
EOC — electrical to optical converter;
EQD — external quantum efficiency;
FET — field-effect transistor;
Gr — graphene;
HBL — hole blocking layer;
HDVIP — high density vertical integrated photodiodes;
IR — infrared;
ITO — indium tin oxide;
LWIR — long-wave infrared;
MEH-PPV — poly[2-methoxy-5-(2′-ethylhexyloxy)-1,4-phenylene vinylene];
MPA — 3-mercaptopropionic acid;
MWIR — mid-wave infrared;
NIR — near infrared;
NNI — natural night illumination;
NVD — night-vision device;
P3HT — poly(3-hexylthiophene-2,5-diyl);
PBI-Por — polybenzimidazoleporphyrin;
PCBM — phenyl-C61-butyric acid methyl ester;
PEDOT — poly(3,4-ethylenedioxythiophene);
PMMA — poly(methyl methacrylate);
polyTPD — poly(4-butyl-*N*,*N*-diphenylaniline);

40 of 48

V.P.Ponomarenko, V.S.Popov, I.A.Shuklov, V.V.Ivanov, V.F.Razumov
Russ. Chem. Rev., 2024, **93** (4) RCR5113

PPV — poly(1,4-phenylene vinylene);

PSE — photosensitive element;

PSS — poly(styrene sulfonic acid);

PVA — poly(vinyl acetate);

QD — quantum dot;

QWIP — quantum well infrared photodetector;

ROIC — readout integrated circuit;

SEM — scanning electron microscopy;

SWIR — short wave infrared;

TAPC — 1,1′-bis[4-(ditolyamino)phenyl]cyclohexane;

TBACl — tetra-n-butylammonium chloride;

TBAF — tetra-n-butylammonium fluoride;

TBAI — tetra-n-butylammonium iodide;

TEC — thermoelectric cooler;

TEM — transmission electron microscopy;

VBM — valence band maximum;

VFET — vertical field-effect transistor;

PbS CQD/C$_{60}$ — heterobarrier or phase boundary;

PbSe@PbS — core@shell structure;

PEDOT:PSS — a mixture of components or a composite layer in which one phase is distributed throughout the other phase;

n-ZnO — n-type semiconductor material;

n⁻-HgTe — very low doped n-type material;

n⁺-Si — high doped n-type material;

p-PbS — p-type semiconductor;

p⁻-HgTe — very low doped p-type material;

p⁺-Si — high doped p-type material;

i-PbS — intrinsic semiconductor;

CQD HgTe (/Au) — field electrode (/Au) is attached to a HgTe CQD layer;

ITO(top contact) — function of the layer;

λ_{DB} — de Broglie wavelength of a particle in a bulk semiconductor;

λ_{max} — wavelength of the maximum sensitivity;

λ_c — cut-off wavelength of a photosensor;

$\Delta\lambda$ — spectral sensitivity range;

μ_e — electron mobility;

μ_h — hole mobility;

ε — dielectric permittivity;

A — photosensor area;

a_0 — lattice constant;

a_B^* — exciton Bohr radius;

D — diameter;

D^* — specific detectivity;

E_c — energy level of conduction band minimum;

E_F — Fermi energy level;

E_g — band gap energy;

F_b — Schottky barrier height;

Δf — amplifier bandwidth;

G — conductivity;

I_{dark} — dark current;

i_n — root-mean-square noise;

m_e^* — effective electron mass;

m_h^* — effective hole mass;

q — charge of the electron;

R — radius;

S_i — responsivity (A W^{-1});

$S_{1\lambda}$ — relative spectral sensitivity;

T — temperature;

V_{bi} — built-in potential,

V_{int} — potential drop near the barrier;

V_{ds} — drain–source bias of FET;

V_{gs} — gate–source bias of FET.

10. References

1. M.Ramamurthy, V.Lakshminarayanan. *Human Vision and Perception. Handbook of Advanced Lighting Technology.* (Cham: Springer, 2015); https://doi.org/10.1007/978-3-319-00295-8_46-1

2. V.Ponomarenko, A.Filachev. *Infrared Techniques and Electro-Optics in Russia: A History 1946–2006.* (Bellingham, Washington, USA: SPIE Press, 2007). 249 p.

3. A.Richards. *Alien Vision. Exploring the Electromagnetic Spectrum with Imaging Technology.* (2nd Edn). (Bellingham, Washington, USA: SPIE Press, 2011)

4. A.Rogalski. *Infrared Detectors.* (2nd Edn). (Boca Raton, FL: CRC Press, 2010); https://doi.org/10.1201/b10319

5. R.D.Hudson. *Infrared System Engineering.* (New-York, London, Sydney, Toronto: Wiley-Interscience, 1969); https://doi.org/10.1016/0022-2860(71)85028-7

6. *Electro-Optical Imaging: System Performance and Modeling.* (Ed. L.M.Biberman). (Bellingham, Washington, USA: SPIE Press, 2000)

7. A.Sadao. *Properties of Semiconductor Alloys. Group-IV, III–V and II–VI Semiconductors.* (Wiley Series in Materials for Electronics & Optoelectronics Applications Book, 2009)

8. M.A.Kinch. *State-of-the-Art Infrared Detector Technology.* (Bellingham, Washington, USA: SPIE Press, 2014)

9. N.Sclar. *Infrared Phys.*, **16**, 435 (1976); https://doi.org/10.1016/0020-0891(76)90084-1

10. D.N.B.Hall, D.Atkinson, K.Hodapp, R.Blank, M.Farris, S.Goebel, K.W.Hodapp, S.M.Jacobson, M.Loost, M.Zandian. *Proc. SPIE*, **9915**, 9915OW (2016); https://doi.org/10.1117/12.2234369

11. M.Zandian, M.Farris, W.McLevige, D.Edwall, E.Arkun, E.Holland, J.E.Gunn, S.Smee, D.N.B.Hall, K.W.Hodapp, A.Shimono, N.Tamura, M.Carmody, J.Auyeung, J.W.Beletic. *Proc. SPIE*, **9915**, 99150F-1 (2016); https://doi.org/10.1117/12.2233664

12. A.Rogalski. *Adv. Opt. Photonics*, **11** (2), 314 (2019); https://doi.org/1364/AOP.11.000314

13. V.P.Ponomarenko, V.S.Popov, S.V.Popov, E.L.Chepurnov. *J. Commun. Technol. Electron.*, **65** (9), 1062 (2020); https://doi.org/10.1134/S1064226920090090

14. V.S.Popov, V.P.Ponomarenko, S.V.Popov. *J. Commun. Technol. Electron.*, **67** (9), 1152 (2022); https://doi.org/10.1134/S1064226922090133

15. V.S.Popov, A.V.Egorov, V.P.Ponomarenko. *J. Commun. Technol. Electron.*, **66** (9), 1092-1095 (2021); https://doi.org/10.1134/S106422692109014X

16. D.Z.-Y.Ting, A.Soibel, L.Höglund, J.Nguyen, C.J.Hill, A.Khoshakhlagh, S.D.Gunapala. In *Advances in Infrared Photodetectors*. Vol. 84. *Type-II Superlattice Infrared Detectors.* (Elsevier, 2011)

17. V.F.Razumov. *Physics-Uspekhi*, **59** (12), 1258 (2016); https://doi.org/10.3367/UFNe.2016.03.037861

18. S.B.Brichkin, V.F.Razumov. *Russ. Chem. Rev.*, **85** (12), 1297 (2016); https://doi.org/10.1070/RCR4656

19. A.I.Ekimov, A.A.Onushchenko. *Pi ̍sma Zh. Eksp. Teor. Fiz.*, **34** (6), 345 (1981)

20. Al.L.Efros, A.L.Efros. *Sov. Phys. Semicond.*, **16** (7), 772 (1982)

21. L.E.Brus. *J. Chem. Phys.*, **79** (11), 5566 (1983); https://doi.org/10.1063/1.445676

22. L.E.Brus. *J. Chem. Phys.*, **80** (9), 4403 (1984); https://doi.org/10.1063/1.447218

23. R.Rossetti, S.Nakahara, L.E.Brus. *J. Chem. Phys.*, **79** (2), 1086 (1983); https://doi.org/10.1063/1.445834

24. H.Weller, U.Koch, M.Gutierres, A.Henglein. *Ber. Bunsenges. Phys. Chem.*, **88**, 649 (1984); https://doi.org/10.1002/bbpc.19840880715

25. A.Ekimov, A.L.Efros, A.Onushchenko. *Solid State Commun.*, **56** (11), 921 (1985); https://doi.org/10.1016/S0038-1098(85)80025-9

V.P.Ponomarenko, V.S.Popov, I.A.Shuklov, V.V.Ivanov, V.F.Razumov
Russ. Chem. Rev., 2024, **93** (4) RCR5113

41 of 48

26. A.J.Nozik, F.Williams, M.T.Nenadovic, T.Rajh, O.I.Micic. *J. Phys. Chem.*, **89** (3), 397 (1985); https://doi.org/10.1021/100249a004

27. H.Weller, A.Fojtik, A.Henglein. *Chem. Phys. Lett.*, **117** (5), 485 (1985); https://doi.org/10.1016/0009-2614(85)80287-6

28. L.Brus. *J. Phys. Chem.*, **90** (12), 2555 (1986); https://doi.org/10.1021/j100403a003

29. M.A.Reed, J.N.Randall, R.J.Aggarwal, R.J.Matyi, T.M.Moore, A.E.Wetsel. *Phys. Rev. Lett.*, **60** (6), 535 (1988); https://doi.org/10.1103/PhysRevLett.60.595

30. C.B.Murray, J.D.Norris, M.G.Bawendi. *J. Am. Chem. Soc.*, **115** (19), 8706 (1993); https://doi.org/10.1021/ja00072a025

31. P.E.Malinowski, E.Georgitzikis, J.Maes, I.Vamvaka, F.Frazzica, J.Van Olmen, P.De Moor, P.Heremans, Z.Hens, D.Cheyns. *Sensors*, **17**, 2867 (2017); https://doi.org/10.3390/s17122867

32. C.Gréboval, D.Darson, V.Parahyba, R.Alchaar, C.Abadie, V.Noguier, S.Ferré, E.Izquierdo, A.Khalili, Y. Prado, P.Potet, E.Lhuillier. *Nanoscale*, **14** (26), 2022; https://doi.org/10.1039/D2NR01313D

33. E.J.D.Klem, C.W.Gregory, D.S.Temple, J.S.Lewis. *Proc. SPIE*, **9555**, 955505 (2015); https://doi.org/10.1117/12.2190372.4519371145001

34. J.Lee, E.Georgitzikis, Y.Li, Z.Lin, J.Park, I.Lieberman, D.Cheyns, M.Jayapala, A.Lambrechts, S.Thijs, R.Stahl, P.E.Malinowski. *2020 IEEE International Electron Devices Meeting (IEDM)*. (San Francisco, CA, 2020). P. 16.5.11; https://doi.org/10.1109/IEDM13553.2020.9372018

35. J.Liu, P.Liu, D.Chen, T.Shi, X.Qu, L.Chen, T.Wu, J.Ke, K.Xiong, M.Li, H.Song, W.Wei, J.Cao, J.Zhang, L.Gao, J.Tang. *Nat. Electron.*, **5** (7), 443 (2022); https://doi.org/10.1038/s41928-022-00779-x

36. C.Gregory, J.A.Hilton, K.Violette, S.Shefte, C.Procida, T.Tessema, M.Bond, E.J.D.Klem. *Proc. SPIE*, **12107**, 1210705 (2022); https://doi.org/10.1117/12.2618320

37. M.Liu, N.Yazdani, M.Yarema, M.Jansen, V.Wood, E.H.Sargent. *Nat. Electron.*, **4**, 548 (2021); https://doi.org/10.1038/s41928-021-00632-7

38. F.P.G.de Arquer, D.V.Talapin, V.I.Klimov, Y.Arakawa, M.Bayer, E.H.Sargent. *Science*, **373**(6555), (2021); https://doi.org/10.1126/science.aaz8541

39. Z.Mamiyev, N.O.Balayeva. *Mater. Today Sustainanable*, **21**, 100305 (2023); https://doi.org/10.1016/j.mtsust.2022.100305

40. W.M.M.Lin, M.Yarema, M.Liu, E.Sargent, V.Wood. *Chimia*, **75** (5), 398 (2021); https://doi.org/10.2533/chimia.2021.398

41. V.Pejovic, E.Georgitzikis, J.Lee, I.Lieberman, D.Cheyns, P.Heremans, P.E.Malinowski. *IEEE Trans. Electron Devices*, **69**, 2840 (2022); https://doi.org/10.1109/TED.2021.3133191

42. M.C.Gupta, J.T.Harrison, M.T.Islam. *Mater. Adv.*, **2**, 3133 (2021); https://doi.org/10.1039/D0MA00965B

43. H.Wu, Z.Ning. *J. Appl. Phys.*, **133**, (2023); https://doi.org/10.1063/5.0133809

44. V.P.Ponomarenko, V.S.Popov, S.V.Popov. *J. Commun. Technol. Electron.*, **67** (Suppl. 1), S1 (2022); https://doi.org/10.1134/S106422692213006X

45. Patent US 4039833 (1977)

46. L.Shkedy, T.Markovitz, Z.Calahorra, I.Hirsh, I.Shtrichman. *Opt. Eng.*, **50** (6), 061008 (2011); https://doi.org/10.1117/1.3572163

47. G.Gershon, A.Albo, M.Eylon, O.Cohen, Z.Calahorra, M.Brumer, M.Nitzani, E.Avnon, Y.Aghion, I. Kogan, E.Ilan, L.Shkedy. *Proc. SPIE*, **8704**, 870438 (2013); https://doi.org/10.1117/12.2015583

48. W.Vereecken, U.Van Bogget, T.Colin, R.-M.Vinella, J.Das, P.Merken, J.Vermeiren. *Proc. SPIE*, **8704**, 870404 (2013); https://doi.org/10.1117/12.2019030

49. V.M.Bazovkin, V.S.Varavin, V.V.Vasil'ev, A.V.Glukhov, D.V.Gorshkov, S.A.Dvoretsky, A.P.Kovchavtsev, Yu.S.Makarov, D.V.Marin, I.V.Mzhelsky, V.G.Polovinkin, V.G.Remesnik, I.V.Sabinina, Yu.G.Sidorov, G.Yu.Sidorov, A.S.Stroganov, A.V.Tsarenko, M.V.Yakushev, A.V.Latyshev.

J. Commun. Technol. Electron., **64** (9), 1011 (2019); https://doi.org/10.1134/S1064226919090043

50. Q.Cai, H.You, H.Guo, J.Wang, B.Liu, Z.Xie, D.Chen, H.Lu, Y.Zheng, R.Zhang. *Light Sci. Appl.*, **10**, 94 (2021); https://doi.org/10.1038/s41377-021-00527-4

51. R.Rehm, R.Driad, L.Kirste, S.Leone, T.Passow, F.Rutz, L.Watschke, A.Zibold. *Phys. Status Solidi A*, **217**, 1900769 (2020); https://doi.org/10.1002/pssa.201900769

52. J.Beck, C.Wan, M.Kinch, J.Robinson, P.Mitra, R.Scritchfield, F.Ma, J.Campbell. *Proc. SPIE*, **5564**, 44 (2004); https://doi.org/10.1117/12.565142

53. J.Beck, C.Wan, M.Kinch, J.Robinson, P.Mitra, R.Scritchfield, F.Ma, J.Campbell. *J. Electron. Mater.*, **35** (6), 1166 (2006); https://doi.org/10.1007/s11664-006-0237-3

54. X.Sun, J.B.Abshire, J.D.Beck, P.R.Mitra, K.Reiff, G.Yang. *Opt. Express*, **25** (14), 16589 (2017); https://doi.org/10.1364/OE.25.016589

55. M.K.Bhowmik, K.Saha, S.Majumder, G.Majumder, A.Saha, A.N.Sarma, D.Bhattacharjee, D.K.Basu, M.Nasipuri. In *Reviews, Refinements and New Ideas in Face Recognition*. (Ed. Dr. P.Corcoran). (InTech, 2011). Ch. 6, P. 120; https://doi.org/10.5772/18986

56. *Modern Developments in Vacuum Electron Sources* (*Topics in Applied Physics 135*). (Eds G.Gaertner, W.Knapp, R.G.Forbes). (Springer, 2020)

57. K.Nakamura, Y.Hamana, Y.Ishigami, T.Matsui. *Nucl. Instr. Meth. Phys. Res. A*, **623**, 276 (2010); https://doi.org/10.1016/j.nima.2010.02.220

58. R.Voilmerhausen, T.Maurer. *Proc. SPIE*, **5076**, 60 (2003); https://doi.org/10.1117/12.487189

59. C.Bellisario, P.Simoneau, P.Keckhut, A.Hauchecorne. *J. Space Weather Space Clim.*, **10**, 21 (2020); https://doi.org/10.1051/swsc/2020017

60. M.L.Vatsia, U.K.Stich, D.Dunlap. *Night-Sky Radiant Sterance from 450 to 2000 Nanometers. Research and Development*. (Technical Report ECOM-7022, U.S.Army Electronics Command, fort Monmouth, NJ, 1972)

61. N.I.Gusarova, N.F.Koshchavtsev, S.V.Popov. *J. Commun. Technol. Electron.*, **61** (10), 1211 (2016); https://doi.org/10.1134/S1064226916100144

62. T.Martin, P.Dixon, M.-A.Gagliardi, N.Masaun. *Proc. SPIE*, **5726**, 85 (2005); https://doi.org/10.1117/12.596409

63. M.D.Enriquez, M.A.Blessinger, J.V.Groppe, T.M.Sudol, J.Battaglia, J.Passe, M.Stern, B.M.Onat. *Proc. SPIE*, **6940**, 69400O (2008); https://doi.org/10.1117/12.778310

64. S.Manda, R.Matsumoto, S.Saito, S.Maruyama, H.Minari, T.Hirano, T.Takachi, N.Fujii, Y.Yamamoto, Y.Zaizen, T.Hirano, H.Iwamoto. *2019 IEEE International Electron Devices Meeting (IEDM)*. (San Francisco, CA, 2019). P. 16.7.1; https://doi.org/10.1109/IEDM19573.2019.8993432

65. S.Lhostis, A.Farcy, E.Deloffre, F.Lorut, S.Mermoz, Y.Henrion, L.Berthier, F.Bailly, D.Scevola, F.Guyader, F.Gigon, C.Besset, S.Pellissier, S.Gay, N.Hotellier, M.Arnoux, A.-L. Le Berrigo, S.Moreau, V.Balan, F.Fournel, A.Jouve, S.Chéramy, B.Rebhan, G.A.Maier, L.Chitu. *2016 IEEE 66th Electronic Components and Technology Conference (ECTC)*. (Las Vegas, NV, 2016). P. 869; https://doi.org/10.1109/ECTC.2016.202

66. Y.Kagawa, S.Hida, Y.Kobayashi, K.Takahashi, S.Miyanomae, M.Kawamura, H.Kawashima, H.Yamagishi, T.Hirano, K.Tatani, H.Nakayama, K.Ohno, H.Iwamoto, S.Kadomura. *2 2019 Electron Devices Technology and Manufacturing Conference (EDTM)*. (Singapore, 2019). P. 297; https://doi.org/10.1109/EDTM.2019.8731186

67. J.Jourdon, S.Lhostis, S.Moreau, J.Chossat, M.Arnoux, C.Sart, Y.Henrion, P.Lamontagne, L.Arnaud, N. Bresson, V.Balan, C.Euvrard, Y.Exbrayat, D.Scevola, E.Deloffre, S.Mermoz, A.Martin, H.Bilgen, F.Andre, C.Charles, D.Bouchu, A.Farcy, S.Guillaumet, A.Jouve, H.Fremont, S.Cheramy. *2018 IEEE International Electron Devices Meeting (IEDM)*. (San

42 of 48

V.P.Ponomarenko, V.S.Popov, I.A.Shuklov, V.V.Ivanov, V.F.Razumov
Russ. Chem. Rev., 2024, 93 (4) RCR5113

Francisco, CA, 2018). P. 7.3.1;
https://doi.org/10.1109/IEDM.2018.8614570

68. S.Moreau, J.Jourdon, S.Lhostis, D.Bouchu, B.Ayoub,
L.Arnaud, H.Fremon. *ECS J. Solid State Sci. Technol.*, 11 (2),
024001 (2022); https://doi.org/10.1149/2162-8777/ac4ffe

69. R.Saran, R.J.Curry. *Nat. Photon.*, 10, 81 (2016);
https://doi.org/10.1038/NPHOTON.2015.280

70. X.Tang, M.M.Ackerman, P.Guyot-Sionnest. *ACS Nano*, 12,
7362 (2018); doi: 10.1021/acsnano.8b03871

71. P.Guyot-Sionnest, M.M.Ackerman, X.Tang. *J. Chem. Phys.*,
151, 060901 (2019); https://doi.org/10.1063/1.5115501

72. T.Nakotte, H.Luo, J.Pietryga. *Nanomaterials*, 10, 172 (2020);
https://doi.org/10.3390/nano10010172

73. P.E.Malinowski, E.Georgitzikis, J.Maes, I.Vamvaka,
F.Frazzica, J.Van Olmen, P.De Moor, P.Heremans, Z.Hens,
D.Cheyns. *Sensors*, 17, 2867 (2017);
https://doi.org/10.3390/s17122867

74. T.Milenkovich, I.A.Shuklov, A.A.Mardini, V.S.Popov. *Mater.
Proc.*, 14 (1), 21 (2023).
https://doi.org/10.3390/IOCN2023-14500

75. E.J.D.Klem, J.Lewis, C.Gregory, G.Cunningham, D.Temple.
Proc. SPIE, 8353, 835337 (2012);
https://doi.org/10.1117/12.919308

76. S.Hinds, E.Klem, C.Gregory, A.Hilton, G.Hames, K.Violette.
Proc. SPIE, 11407, 1140707 (2020);
https://doi.org/10.1117/12.2559115

77. J.Lee, E.Georgitzikis, Y.Li, Z.Lin, J.Park, I.Lieberman,
D.Cheyns, M.Jayapala, A.Lambrechts, S.Thijs, R.Stahl,
P.E.Malinowski. *2020 IEEE International Electron Devices
Meeting (IEDM)*. (San Francisco, CA, 2020). P. 16.5.11;
https://doi.org/10.1109/IEDM13553.2020.9372018

78. J.S.Steckel, E.Josse, A.G.Pattantyus-Abraham, M.Bidaud,
B.Mortini, H.Bilgen, O.Arnaud, S.Allegret-Maret, F.Saguin,
L.Mazet, S.Lhostis, T.Berger, K.Haxaire, L.L.Chapelon,
L.Parmigiani, P.Gouraud, M.Brihoum, P.Bar, M.Guillermet,
S.Favreau, R.Duru, J.Fantuz, S.Ricq, D.Ney, I.Hammad,
D.Roy, A.Arnaud , B.Vianne, G.Nayak, N.Virollet, V.Farys,
P.Malinge, A.Tournier, F.Lalanne, A.Crocherie, J.Galvier,
S.Rabary, O.Noblanc, H.Wehbe-Alause, S.Acharya, A.Singh,
J.Meitzner, D.Aher, H.Yang, J.Romero, B.Chen, C.Hsu,
K.C.Cheng, Y.Chang, M.Sarmiento, C.Grange, E.Mazaleyrat,
K.Rochereau. *2021 IEEE International Electron Devices
Meeting* (IEDM). (San Francisco, CA, 2021). P. 23.2.1;
https://doi.org/10.1109/IEDM19574.2021.9720560

79. I.A.Shuklov, V.F.Toknova, D.V.Dyomkin, G.I.Lapushkin,
L.M.Nikolenko, A.A.Lizunova, S.B.Brichkin, V.N.Vasilets,
V.F.Razumov. *High Energy Chemistry*, 54 (3), 183 (2020);
https://doi.org/10.1134/S0018143920030133

80. S.A.McDonald, P.W.Cyr, L.Levina, E.H.Sargent. *Appl. Phys.
Lett.*, 85 (11), 2089 (2004); https://doi.org/10.1063/1.1792380

81. S.A.McDonald, G.Konstantatos, S.Zhang, P.W.Cyr,
E.J.D.Klem, L.Levina, E.H.Sargent. *Nat. Mater.*, 4, 138
(2005); https://doi.org/10.1038/nmat1299

82. T.Rauch, M.Boberl, S.F.Tedde, J.Furst, M.V.Kovalenko,
G.Hesser, U.Lemmer, W.Heiss, O.Hayden. *Nat. Photon.*, 3,
332 (2009); https://doi.org/10.1038/nphoton.2009.72

83. E.J.Klem, J.S.Lewis, D.Temple. *Proc. SPIE*, 7660, 76602E
(2010); https://doi.org/10.1117/12.849708

84. E.J.D.Klem, C.W.Gregory, G.B.Cunningham, S.Hall,
D.S.Temple, J.S.Lewis. *Appl. Phys. Lett.*, 100, 173109 (2012);
https://doi.org/10.1063/1.4707377

85. E.Klem, J.Lewis, C.Gregory, G.Cunningham, D.Temple,
A.D'Souza, E.Robinson, P.S.Wijewarnasuriya, N.Dhar.
Proc. SPIE, 8868, 886806 (2013);
https://doi.org/10.1117/12.2026972

86. E.Klem, J.Lewis, C.Gregory, G.Cunningham, D.Temple,
A.D'Souza, E.Robinson, P.S.Wijewarnasuriya, N.Dhar.
Proc SPIE, 8704, 870436 (2013);
https://doi.org/10.1117/12.2019521

87. E.J.D.Klem, J.Lewis, C.Gregory, D.Temple,
P.S.Wijewarnasuriy, N.Dhar. *Proc. SPIE*, 9070, 907039
(2014); https://doi.org/10.1117/12.2054215

88. E.J.D.Klem, C.Gregory, D.Temple, J.Lewis. *Proc. SPIE*, 9451,
945104-1 (2015); https://doi.org/10.1117/12.2178532

89. P.Palomaki, S.Keuleyan. *IEEE Spectrum*, 57 (3), 24 (2020);
https://doi.org/10.1109/mspec.2020.9014456

90. V.Pejovic, J.Lee, E.Georgitzikis, Y.Li, J.-H.Kim, I.Lieberman,
P.E.Malinovski, P.Heremans, D.Cheyns. *IEEE Electron
Device Lett.*, 42 (8), 1196 (2021);
https://doi.org/10.1109/LED.2021.3093081

91. E.Georgitzikis, P.E.Malinowski, J.Maes, A.Hadipour, Z.Hens,
P.Heremans, D.Cheyns. *Adv. Funct. Mater.*, 28, 1804502
(2018); https://doi.org/10.1002/adfm.201804502

92. E.Georgitzikis, P.E.Malinowski, Y.Li, J.Lee, A.Süss,
F.Frazzica, J.Maes, S.Gielen, F.Verstraeten, P.Boulenc,
M.Mao, S.Guerrieri, W.Maes, Z.Hens, P.Heremans, D.Cheyns.
2019 International Image Sensor Workshop (Proc. IISW), R43
2019

93. E.Georgitzikis, P.E.Malinowski, Y.Li, J.Maes, L.M.Hagelsieb,
S.Guerrieri, Z.Hens, P.Heremans, D.Cheyns. *IEEE Sensors J.*,
20 (13), 6841 (2020);
https://doi.org/10.1109/JSEN.2019.2933741

94. I.G.Neizvestnyi, A.E.Klimov, V.N.Shumsky. *Physics –
Uspekhi*, 58 (10), 952 (2015);
https://doi.org/ 10.3367/UFNr.0185.201510b.1031

95. Y.Luo, Y.Tan, C.Bi, S.Zhang, X.Xue, M.Chen, Q.Hao, Y.Liu,
X.Tang. *APL Photon*, 8, 056109 (2023);
https://doi.org/10.1063/5.0145374

96. I.M.E.Sachinthanie, M.M.I.H.K.Madigasekara, H.C.S.Perera.
Ceylon J. Sci., 52 (2) 113 (2023);
https://doi.org/10.4038/cjs.v52i2.8154

97. H.Song, Y.Tischenko, D.Wasserman, K.S.Jeong. *Opt. Mater.
Express*, 13 (5/1), 1328 (2023);
https://doi.org/10.1364/OME.489877

98. T.Nakotte, S.G.Munyan, J.W.Murphy, S.A.Hawks, S.Y.Kang,
J.Han, A.M.Hiszpanski. *J. Mater. Chem. C*, 10, 790 (2022);
https://doi.org/10.1039/D1TC05359K

99. C.Gréboval, A.Chu, N.Goubet, C.Livache, S.Ithurria,
E.Lhuillier. *Chem. Rev.*, 121, 3627 (2021);
https://doi.org/10.1021/acs.chemrev.0c01120

100. A.Chu, B.Martinez, S.Ferré, V.Noguier, C.Gréboval,
C.Livache, J.Qu, Y.Prado, N.Casaretto, N.Goubet, H.Cruguel,
L.Dudy, M.G.Silly, G.Vincent, E.Lhuillier. *ACS Appl. Mater.
Interfaces*, 11, 33116 (2019);
https://doi.org/10.1021/acsami.9b09954

101. A.Chatterjee, N.B.Pendyala, A.Jagtap, K.S.R.K.Rao. *e-Journal
Surface Sci. Nanotechnol.*, 17, 95 (2019);
https://doi.org/10.1380/ejssnt.2019.95

102. V.S.Popov, V.P.Ponomarenko, S.V.Popov. *RFBR J.*, 1 (117),
73 (2023);
https://doi.org/10.22204/2410-4639-2023-117-01-73-88

103. I.A.Shuklov, D.V.Dyomkin, V.A.Konavicheva, V.S.Popov,
V.F.Razumov. *J. Commun. Technol. Electron.*, 68 (S2),
S184–S189 (2023);
https://doi.org/ 10.1134/S1064226923140152

104. S.Goossens, G.Navickaite, C.Monasterio, S.Gupta,
J.J.Piqueras, R.Pérez, G.Burwell, I.Nikitskiy, T.Lasanta,
T.Galán, E.Puma, A.Centeno, A.Pesquera, A.Zurutuza,
G.Konstantatos, F.Koppens. *Nat. Photon.*, 11, 366 (2017);
https://doi.org/10.1038/NPHOTON.2017.75

105. O.Madelung. *Semiconductors: Data Handbook*. (3rd Edn).
(Berlin, Heidelberg: Springer, 2004);
https://doi.org/10.1007/978-3-642-18865-7

106. I.M.Tsidilkovski. *Gapless Semiconductors – a New Class of
Materials*. (Berlin: Akademie-Verlag, 1988);
https://doi.org/10.1515/9783112643143

107. J.Ruan, S.-K.Jian, H.Yao, H.Zhang, S.-C.Zhang, D.Xing.
Nat. Commun., 7, 11136 (2016);
https://doi.org/10.1038/ncomms11136

V.P.Ponomarenko, V.S.Popov, I.A.Shuklov, V.V.Ivanov, V.F.Razumov
Russ. Chem. Rev., 2024, **93** (4) RCR5113

43 of 48

108. Y.Kayanuma. *Phys. Rev.*, **38** (14), 9797 (1988);
https://doi.org/10.1103/PhysRevB.38.9797

109. Y.Kayanuma, H.Momiji. *Phys. Rev.*, **41** (14), 10261 (1990);
https://doi.org/10.1103/PhysRevB.41.10261

110. Y.Wang, N.Herron. *J. Phys. Chem.*, **95** (2), 525 (1991);
https://doi.org/10.1021/j100155a009

111. A.I.Ekimov, F.Hache, M.C.Schanne-Klein, D.Ricard,
C.Flytzanis, I.A.Kudryavtsev, T.V.Yazeva, A.V.Rodina,
Al.A.Efros. *J. Opt. Soc. Am. B*, **10**(1), 100 (1993);
https://doi.org/10.1364/JOSAB.10.000100

112. S.V.Gaponenko. *Optical Properties of Semiconductor
Nanocrystals*. (Cambridge, 1998);
https://doi.org/10.1017/CB09780511524141

113. *Colloidal Quantum Dot Optoelectronics and Photovoltaics*.
(Eds G.Konstantatos, E.H.Sargent). (Cambridge: Cambridge
University Press, 2013)

114. S.V.Karpov, S.V.Mikushev. *Phys. Solid State*, **52** (8), 1750
(2010); https://doi.org/10.1134/S1063783410080287

115. C.M.Evans, L.C.Cass, K.E.Knowles, D.B.Tice, R.P.H.Chang,
E.A.Weiss. *J. Coord. Chem.*, 65:13, 2391 (2012);
https://doi.org/10.1080/00958972.2012.695019

116. A.V.Baranov, E.V.Ushakova, V.V.Golubkov, A.P.Litvin,
P.S.Parfenov, A.V.Fedorov, K.Berwick. *Langmuir*, 2014;
https://doi.org/10.1021/la503913z

117. X.Tang, X.Tang, K.W.C.Lai. *ACS Photonics*, **3** (12), 2396
(2016); https://doi.org/10.1021/acsphotonics.6b00620

118. Y.Wang, A.Suna, W.Mahler, R.Kasowski. *J. Chem. Phys.*, **87**,
7315 (1987); https://doi.org/10.1063/1.453325

119. I.Kang, F.W.Wise. *J. Opt. Soc. Am. B*, **14** (7), 1632 (1997);
https://doi.org/10.1364/JOSAB.14.001632

120. A.D.Andreev, A.A.Lipovskii. *Phys. Rev. B*, **59** (23), 15402
(1999); https://doi.org/10.1103/PhysRevB.59.15402

121. C.B.Murray, S.Sun, W.Gaschler, H.Doyle, T.A.Betley,
C.R.Kagan. *IBM J. Res. Dev.*, **45** (1), 47 (2001);
https://doi.org/10.1147/rd.451.0047

122. G.Allan, C.Delerue. *Phys. Rev. B*, **70**, 245321 (2004);
https://doi.org/10.1103/PhysRevB.70.245321

123. J.M.Harbold, H.Du, T.D.Krauss, K.-S.Cho, C.B.Murray,
F.W.Wise. *Phys. Rev. B*, **72**, 195312 (2005);
https://doi.org/10.1103/PhysRevB.72.195312

124. J.M.An, A.Franceschetti, S.V.Dudiy, A.Zunger. *Nano Lett.*, **6**
(12), 2728 (2006); https://doi.org/10.1021/nl061684x

125. G.Nootz, L.A.Padilha, P.D.Olszak, S.Webster, D.J.Hagan,
E.W.Van Stryland, L.Levina, V.Sukhovatkin, L.Brzozowski,
E.H.Sargent. *Nano Lett.*, **10**, 3577 (2010);
https://doi.org/10.1021/nl101867

126. A.N.Poddubny, M.O.Nestoklon, S.V.Goupalov. *Phys. Rev. B*,
86, 035324 (2012);
https://doi.org/10.1103/PhysRevB.86.035324

127. V.L.Ermolaev. *Opt. Spectrosc.*, **125**, 256 (2018);
https://doi.org/10.1134/S0030400X18080052

128. A.Rogalski. *Infrared and Terahertz Detectors*. (3rd Edn).
(CRC Press, 2019); https://doi.org/10.1201/b21951

129. L.D.Landau, E.M.Lifshitz. *Electrodynamics of Continuous
Media*. (Oxford: Pergamon Press, 1984);
https://doi.org/10.1016/8978-0-08-030275-1.50007-2

130. K.V.Reich, B.I.Shklovskii. *Appl. Phys. Lett.*, **108**, 113104
(2016); https://doi.org/10.1063/1.4944407127

131. K.V.Reich. *Phys. Usp.*, **63**, 994 (2020);
https://doi.org/10.3367/UFNr.2019.08.038649

132. B.I.Shklovskii, A.L.Efros. *Electronic Properties of Doped
Semiconductors*. (Berlin, Heidelberg: Springer-Verlag, 1984);
https://doi.org/10.1007/978-3-662-02405-4

133. H.Liu, A.Pourret, P.Guyot-Sionnest. *ACS Nano*, **4** (9), 5211
(2010); https://doi.org/10.1021/nn101376u

134. N.Ray. *Charge Transport in Nanopatterned PbS Quantum Dot
Arrays*. PhD Thesis, Massachusetts Institute of Technology,
2014

135. A.Zabet-Khosousi, Al-Amin Dhirani. *Chem. Rev.*, **108**, 4072
(2008); https://doi.org/10.1021/cr0680134

136. D.V.Talapin, J.-S.Lee, M.V.Kovalenko, E.V.Shevchenko.
Chem. Rev., **110**, 389 (2010);
https://doi.org/10.1021/cr900137k

137. A.A.Chistyakov, M.A.Zvaigzne, V.R.Nikitenko, A.R.Tameev,
I.L.Martynov, O.V.Prezhdo. *J. Phys. Chem. Lett.*, **8**, 4129
(2017); https://doi.org/ 10.1021/acs.jpclett.7b00671

138. S.D.Baranovskii. *Phys. Status Solidi B*, **251** (3), 487 (2014);
https://doi.org/10.1002/pssb.201350339

139. Z.Zhang, J.Sung, D.T.W.Toolan, S.Han, R.Pandya, M.P.Weir,
J.Xiao, S.Dowland, M.Liu, A.J.Ryan, R.A.L.Jones, S.Huang,
A.Rao. *Nat. Mater.*, **21**, 533 (2022);
https://doi.org/10.1038/s41563-022-01204-6

140. C.L.Tan, H.Mohseni. *Nanophotonics*, **7** (1), 169 (2018);
https://doi.org/10.1515/nanoph-2017-0061

141. C.Livache, B.Martinez, N.Goubet, J.Ramade, E.Lhuillier.
Front. Chem., **6**, 575 (2018);
https://doi.org/10.3389/fchem.2018.00575

142. M.C.Gupta, J.T.Harrison, Md Toriqul Islam. *Mater. Adv.*, **2**,
3133 (2021); https://doi.org/10.1039/d0ma00965b

143. B.Martinez, C.Livache, L.D.M.Notemgnou, N.Goubet,
S.Keuleyan, H.Cruguel, S.Ithurria, H.Aubin, A.Ouerghi,
B.Doudin, E.Lacaze, B.Dubertret, M.G.Silly, Ricardo Psm
Lobo, J.F.Dayen, E.Lhuillier. *ACS Appl. Mater. Interfaces*, **9**
(41), 36173 (2017); https://doi.org/10.1021/acsami.7b10665

144. V.Rinnerbauer, K.Hingerl. *Appl. Phys. Lett.*, **89**, 193114
(2006); https://doi.org/10.1063/1.2387110

145. V.A.Harutyunyan, D.B.Hayrapetyan, E.M.Kazaryan. *Phys.
Solid State*, **62** (8), 1305 (2020);
https://doi.org/10.1134/S106378342008003X

146. A.V.Baranov, E.V.Ushakova, V.V.Golubkov, A.P.Litvin,
P.S.Parfenov, A.V.Fedorov, K.Berwick. *Langmuir*, **31**, 506
(2015); https://doi.org/10.1021/la503913z

147. O.E.Semonin, J.M.Luther, M.C.Beard. *Mater. Today*, **15** (11),
508 (2012); https://doi.org/10.1016/S1369-7021(12)70220-1

148. A.Jagtap, C.Livache, B.Martinez, J.Qu, A.C.Hu,
C.H.Gréboval, N.Goubet, E.Lhuillier. *Opt. Mater. Express*, **8**
(5), 1174 (2018); https://doi.org/10.1364/OME.8.001174

149. X.Tang, G.Wu, K.W.C.Lai. *2017 IEEE 17th International
Conference on Nanotechnology (IEEE-NANO)*. (Pittsburgh,
PA, 2017). P. 641;
https://doi.org/10.1109/NANO.2017.8117308

150. S.Guohua, P.Guyot-Sionnest. *J. Phys. Chem. C*, **120** (21),
11744 (2016); https://doi.org/10.1021/acs.jpcc.6b04014

151. J.Qiu, B.Weng, L.L.McDowell, Z.Shi. *RSC Adv.*, **9** (72), 42516
(2019); https://doi.org/10.1039/c9ra07664f

152. W.D.Lawson, F.A.Smith, A.S.Young. *J. Electrochem. Soc.*,
107, 206 (1960); https://doi.org/10.1149/1.2427652

153. N.F.Borrelli, D.W.Smith. *J. Non-Crystal. Solids*, **180**, 25
(1994); https://doi.org/10.1016/0022-3093(94)90393-X

154. C.B.Murray, S.Sun, W.Gaschler, H.Doyle, T.A.Betley,
C.R.Kagan. *IBM J. Res. Dev.*, **45** (1), 47 (2001);
https://doi.org/10.1147/rd.451.0047

155. M.A.Hines, G.D.Scholes. *Adv. Mater.*, **15** (21), 1844 (2003);
https://doi.org/10.1002/adma.200305395

156. C.Hu, A.Gassenq, Y.Justo, K.Devloo-Casier, H.Chen,
C.Detavernier, Z.Hens, R.Roelkens. *Appl. Phys. Lett.*, **105**,
171110 (2014); https://doi.org/10.1063/1.4900930

157. F.P.G.deArquer, T.Lasanta, M.Bernechea, G.Konstantatos.
Small, **11** (22), 2636 (2015);
https://doi.org/10.1002/smll.201403359

158. N.Killilea, M.Wu, M.Sytnyk, A.A.Y.Amin, O.Mashkov,
E.Spiecker, W.Heiss. *Adv. Funct. Mater.*, 1807964 (2019);
https://doi.org/10.1002/adfm.201807964

159. G.Konstantatos, I.Howard, A.Fischer, S.Hoogland, J.Clifford,
E.Klem, L.Levina, E.H.Sargent. *Nature*, **442**, 180 (2006);
https://doi.org/10.1038/nature04855

160. G.Konstantatos, J.Clifford, L.Levina, E.H.Sargent.
Nat. Photon., **1** (9), 531 (2007);
https://doi.org/10.1038/nphoton.2007.147

161. S.Yakunin, D.N.Dirin, L.Protesescu, M.Sytnyk,
S.Tollabimazraehno, M.Humer, F.Hackl, T.Fromherz,

44 of 48

V.P.Ponomarenko, V.S.Popov, I.A.Shuklov, V.V.Ivanov, V.F.Razumov
Russ. Chem. Rev., 2024, **93** (4) RCR5113

M.I.Bodnarchuk, M.V.Kovalenko, W.Heiss. *ACS Nano*, **3**, 12883 (2014); https://doi.org/10.1021/nn5067478

162. J.He, M.Luo, L.Hu, Y.Zhou, S.Jiang, H.Song, R.Ye, J.Chen, L.Gao, J.Tang. *J. Alloys Compd.*, **596**, 73 (2014); https://doi.org/10.1016/j.jallcom.2014.01.194

163. C.Li, T.Bai, F.Li, L.Wang, X.Wu, L.Yuan, Z.Shi, S.Feng. *CrystEngComm*, **15**, 597 (2013); https://doi.org/10.1039/c2ce26516h

164. A.Sashchiuk, D.Yanover, A.Rubin-Brusilovski, G.I.Maikov, R.K.Capek, R.Vaxenburg, J.Tilchin, G.Zaiats, E.Lifshitz. *Nanoscale*, **5** (17), 7724 (2013); https://doi.org/10.1039/c3nr02141f

165. G.Xiao, Y.Wang, J.Ning, Y.Wei, B.Liu, W.W.Yu, G.Zou, B.Zou. *RSC Adv.*, **3** (22), 8104 (2013); https://doi.org/10.1039/c3ra23209c

166. A.Shapiro, Y.Jang, A.Rubin-Brusilovski, A.K.Budniak, F.Horani, A.Sashchiuk, E.Lifshitz. *Chem. Mater.*, **28** (17), 6409 (2016); https://doi.org/10.1021/acs.chemmater.6b02917

167. M.Thambidurai, Y.Jang, A.Shapiro, G.Yuan, X.Hu, Y.Uechao, O.Wang, E.Lifshitz, H.V.Demir, C.Ang. *Opt. Mater. Express*, **7**, 2326 (2017); https://doi.org/10.1364/OME.7.002326

168. I.A.Shuklov, V.F.Razumov. *Russ. Chem. Rev.*, **89**, 379 (2020); https://doi.org/10.1070/RCR4917

169. R.D.Schaller, V.I.Klimov. *Phys. Rev. Lett.*, **92** (18), 186601 (2004); https://doi.org/10.1103/PhysRevLett.92.186601

170. R.J.Ellingson, M.C.Beard, J.C.Johnson, P.Yu, O.I.Micic, A.J.Nozik, A.Shabaev, Al.L.Efros. *Nano Lett.*, **5** (5), 865 (2005); https://doi.org/10.1021/nl0502672

171. M.Kumar, S.Vezzoli, Z.Wang, V.Chaudhary, R.V.Ramanujan, G.G.Gurzadyan, A.Bruno, C.Soci. *Phys. Chem. Chem. Phys.*, **18** (45), 31107 (2016); https://doi.org/10.1039/c6cp03790a

172. G.Nair, S.M.Geyer, L.-Y.Chang, M.G.Bawendi. *Phys. Rev. B*, **78**, 125325 (2008); https://doi.org/10.1103/PhysRevB.78.125325

173. H.Goodwin, T.C.Jellicoe, N.J.L.K.Davis, M.L.Böhm. *Nanophotonics*, **7** (1), 111 (2018); https://doi.org/10.1515/nanoph-2017-0034

174. H.Jin, C.Livache, W.D.Kim, B.T.Diroll, R.D.Schaller, V.I.Klimov. *Nat. Mater.*, **22**, 1013 (2023); https://doi.org/10.1038/s41563-023-01598-x

175. S.Keuleyan, E.Lhuillier, P.Guyot-Sionnest. *J. Am. Chem. Soc.*, **8**(8), 8676 (2011); https://doi.org/10.1021/nn503805h

176. S.Keuleyan, E.Lhuillier, P.Guyot-Sionnest. *J. Am. Chem. Soc.*, **133** (41), 16422 (2011); https://doi.org/10.1021/ja2079509

177. X.Tang, Guang fu Wu, K.W.C.Lai. *J. Mater. Chem. C*, **5** (2), 362 (2017); https://doi.org/10.1039/c6tc04248a

178. Y.Yifat, M.Ackerman, P.Guyot-Sionnest. *Appl. Phys. Lett.*, **110**(4), 041106 (2017); https://doi.org/10.1063/1.4975058

179. M.E.Cryer, J.E.Halp. *ACS Photonics*, **5** (8), 3009 (2018); https://doi.org/10.1021/acsphotonics.8b00738

180. Z.Deng, K.S.Jeong, P.Guyot-Sionnest. *ACS Nano*, **8** (11), 11707 (2014); https://doi.org/10.1021/nn505092a

181. M.Chen, Q.Hao, Y.Luo, X.Tang. *ACS Nano*, **16**, 11027 (2022); https://doi.org/10.1021/acsnano.2c03631

182. E.Lhuillier, S.Keuleyan, P.Zolotavin, P.Guyot-Sionnest. *Adv. Mater.*, **25** (1), 137 (2013); https://doi.org/10.1002/adma.201203012

183. E.Heves, C.Ozturk, V.Ozguz, Y.Gurbuz. *IEEE Electron. Dev. Lett.*, **34** (5), 662 (2013); https://doi.org/10.1109/LED.2013.2253756

184. A.G.Vitukhnovsky. *Phys. Usp.*, **56** (6), 623 (2013); https://doi.org/10.3367/UFNe.0183.201306h.0653

185. A.N.Aleshin. *Phys. Usp.*, **56** (6), 627 (2013); https://doi.org/10.3367/UFNe.0183.201306i.0657

186. A.Jagtap, N.Goubet, C.Livache, A.Chu, B.Martinez, C.Greboval, J.Qu, E.Dandeu, L.Becerra, N.Witkowski, S.Ithurria, F.Mathevet, M.G.Silly, B.Dubertret, E.Lhuillier. *J. Phys. Chem. C*, **122** (26), 14979 (2018); https://doi.org/10.1021/acs.jpcc.8b03276

187. P.Martyniuk, M.Kopytko, A.Rogalski. *Opto-Electron. Rev.*, **22** (2), 127 (2014); https://doi.org/10.2478/s11772-014-0187-x

188. A.M.Jagtap, B.Martinez, N.Goubet, A.Chu, C.Livache, C.Greboval, J.Ramade, D.Amelot, P.Trousset, A.Triboulin, S.Ithurria, M.G.Silly, B.Dubertret, E.Lhuillier. *ACS Photonics*, **5** (11), 4569 (2018); https://doi.org/10.1021/acsphotonics.8b01032

189. B.Martinez, C.Livache, A.Chu, C.Gréboval, H.Cruguel, N.Goubet, E.Lhuillier. *Phys. Status Solidi A*, 1900449 (2019); https://doi.org/10.1002/pssa.201900449

190. C.Livache, B.Martinez, N.Goubet, C.Gréboval, J.Qu, A.Chu, S.Royer, S.Ithurria, M.G.Silly, B.Dubertret, E.Lhuillier. *Nat. Commun.*, **10** (1), 2125 (2019); https://doi.org/10.1038/s41467-019-10170-8

191. X.Tang, M.M.Ackerman, M.Chen, P.Guyot-Sionnest. *Nat. Photon.*, **13** (4), 277 (2019); https://doi.org/10.1038/s41566-019-0362-1

192. M.M.Ackerman, M.Chen, P.Guyot-Sionnest. *Appl. Phys. Lett.*, **116** (8), 083502 (2020); https://doi.org/10.1063/1.5143252

193. M.M.Ackerman, X.Tang, P.Guyot-Sionnest. *ACS Nano*, **12** (7), 7264 (2018); https://doi.org/10.1021/acsnano.8b03425

194. X.Lan, M.Chen, M.H.Hudson, V.Kamysbayev, Y.Wang, P.Guyot-Sionnest, D.V.Talapin. *Nat. Mater.*, **19**, 323 (2020); https://doi.org/10.1038/s41563-019-0582-2

195. X.Xue, M.Chen, Y.Luo, T.Qin, X.Tang, Q.Hao. *Light Sci. Appl.*, **12**, 2 (2023); https://doi.org/10.1038/s41377-022-01014-0

196. J.P.Clifford, K.W.Johnston, L.Levina, E.H.Sargent. *Appl. Phys. Lett.*, **91** (25), 2531171 (2007); https://doi.org/10.1063/1.2823582

197. J.P.Clifford, G.Konstantatos, K.W.Johnston, S.Hoogland, L.Levina, E.H.Sargent. *Nat. Nanotechnol.*, **9** (1), 40 (2008); https://doi.org/10.1038/NNANO.2008.313

198. J.P.Clifford. PhD Thesis. University of Toronto, 2008

199. R.Dong, C.Bi, Q.Dong, F.Guo, Y.Yuan, Y.Fang, Z.Xiao, J.Huang. *Adv. Opt. Mater.*, **2** (6), 549 (2014); https://doi.org/10.1002/adom.201400023

200. J.-B.Kwon, S.-W.Kim, B.-H.Kang, S.-H.Yeom, W.-H.Lee, D.-H.Kwon, J.-S.Lee, S.W.Kang. *Nano Convergence*, **7**, 28 (2020); https://doi.org/10.1186/s40580-020-00238-3

201. G.S.Selopal, H.Zhao, Z.M.Wang, F.Rosei. *Adv. Funct. Mater.*, 1908762 (2020); https://doi.org/ 10.1002/adfm.201908762

202. Y.Wei, Z.Ren, A.Zhang, P.Mao, H.Li, X.Zhong, W.Li, S.Yang, J.Wang. *Adv. Funct. Mater.*, **28** (11), 1706690 (2018); https://doi.org/10.1002/adfm.201706690

203. B.N.Pal, I.Robel, A.Mohite, R.Laocharoensuk, D.J.Werder, V.I.Klimov. *Adv. Funct. Mater.*, **22** (8), 1741 (2012); https://doi.org/10.1002/adfm.201102532

204. P.R.Brown, D.Kim, R.R.Lunt, Z.Ni, M.G.Bawendi, J.C.Grossman, V.Bulovic. *ACS Nano*, **8** (6), 5863 (2014); https://doi.org/10.1021/nn500897c

205. J.W.Lee, D.Y.Kim, F.So. *Adv. Funct., Mater.*, **25** (8), 1233 (2015); https://doi.org/10.1002/adfm.201403673

206. W.Gao, G.Zhai, C.Zhang, Z.Shao, L.Zheng, Y.Zhang, Y.Yang, X.Li, X.Liu, B.Xu. *RSC Adv.*, **8** (27), 15149 (2018); https://doi.org/10.1039/c8ra01422a

207. I.D.Skurlov, I.G.Korzhenevskii, A.S.Mudrak, A.Dubavik, S.A.Cherevkov, P.S.Parfenov, X.Zhang, A.V.Fedorov, A.P.Litvin, A.V.Baranov. *Materials*, **12** (19), 3219 (2019); https://doi.org/10.3390/ma12193219

208. J.Xu, H.Wang, S.Yang, G.Ni, B.Zou. *J. Alloys Compd.*, **764**, 446 (2018); https://doi.org/10.1016/j.jallcom.2018.06.105

209. A.Stavrinadis, S.Pradhan, P.Papagiorgis, G.Itskos, G.Konstantatos. *ACS Energy Lett.*, **2** (4), 739 (2017); https://doi.org/10.1021/acsenergylett.7b00091

210. Q.Xu, L.Meng, K.Sinha, F.I.Chowdhury, J.Hu, X.Wang. *ACS Photonics*, **7**, 1297 (2020); https://doi.org/10.1021/acsphotonics.0c00363

211. V.S.Popov, V.P.Ponomarenko, D.V.Dyomkin, I.A.Shuklov, A.V.Gadomskaya, S.B.Brichkin, N.A.Lavrentiev, V.U.Gak, A.E.Mirofyanchenko, E.V.Mirofyanchenko, A.V.Katsaba, P.V.Arsenov, V.V.Ivanov, V.F.Razumov. *Dokl. Phys.*, **68** (7), 217 (2023); https://doi.org/10.1134/S1028335823070066

V.P.Ponomarenko, V.S.Popov, I.A.Shuklov, V.V.Ivanov, V.F.Razumov
Russ. Chem. Rev., 2024, **93** (4) RCR5113

45 of 48

212. W.J.E.Beek, M.M.Wienk, M.Kemerink, X.Yang, R.A.J.Janssen. *J. Phys. Chem. B*, **109** (19), 9505 (2005); https://doi.org/10.1021/jp050745x

213. D.Langley, G.Giusti, C.Mayousse, C.Celle, D.Bellet, J.-P.Simonato. *Nanotechnology*, **24** (45), 452001 (2013); https://doi.org/10.1088/0957-4484/24/45/452001

214. J.Hu, S.Yang, Z.Zhang, H.Li, C.P.Veeramalai, M.Sulaman, M.I.Saleem, Y.Tang, Y.Jiang, L.Tang, B.Zou. *J. Mater. Sci. Technol.*, **68**, 216 (2021); https://doi.org/10.1016/j.jmst.2020.06.047

215. J.Qiu, B.Weng, L.L.McDowell, Z.Shi. *RSC Adv.*, **9** (72), 42516 (2019); https://doi.org/10.1039/c9ra07664f

216. X.Tang, M.Chen, A.Kamath, M.Ackerman, P.Guyot-Sionnest. *ACS Photonics*, **7** (5), 1117 (2020); https://dx.doi.org/10.1021/acsphotonics.0c00247

217. J.Yang, Y.Lv, Z.He, B.Wang, S.Chen, F.Xiao, H.Hu, M.Yu, H.Liu, X.Lan, H.Y.Hsu, H.Song, J.Tang. *ACS Photonics*, **10** (7), 2226 (2023); https://doi.org/10.1021/acsphotonics.2c01145

218. W.Gong, P.Wang, W.Deng, J.Li, W.Li, J.Li, Z.Chen, J.Li, Y.Zhang. *IEEE Transactions on Electron Devices*, **70** (7), 3668 (2023); https://doi.org/10.1109/TED.2023.3276730

219. R.S.C.Gobbold. *Theory and Applications of Field-Effect Transistors*. (Wiley-Interscience, 1970)

220. M.Chen, H.Lu, N.M.Abdelazim, Y.Zhu, Z.Wang, W.Ren, S.V.Kershaw, A.L.Rogach, N.Zhao. *ACS Nano*, **11** (6), 5614 (2017); https://doi.org/10.1021/acsnano.7b00972

221. N.Huo, S.Gupta, G.Konstantatos. *Adv. Mater.*, **29** (17), 1606576 (2017); https://doi.org/10.1002/adma.201606576

222. M.Chen, X.Lan, X.Tang, Y.Wang, M.H.Hudson, D.V.Talapin, P.Guyot-Sionnest. *ACS Photonics*, **6** (9), 2358 (2019); https://doi.org/10.1021/acsphotonics.9b01050

223. G.Konstantatos, M.Badioli, L.Gaudreau, J.Osmond, M.Bernechea, F.P.G. de Arquer, F.Gatti, F.H.L.Koppens. *Nat. Nanotechnol.*, **7** (6), 363 (2012); https://doi.org/10.1038/NNANO.2012.60

224. D.Zhang, L.Gan, Y.Cao, Q.Wang, L.Qi, X.Guo. *Adv. Mater.*, **24**, 2715 (2012); https://doi.org/10.1002/adma.201104597

225. Z.Sun, Z.Liu, J.Li, G.Tai, S.-P.Lau, F.Yan. *Adv. Mater.*, **24** (43), 5878 (2012); https://doi.org/ 10.1002/adma.201202220

226. L.Turyanska, O.Makarovsky, S.A.Svatek, P.H.Beton, C.J.Mellor, A.Patanè, L.Eaves, N.R.Thomas, M.W.Fay, A.J.Marsden, N.R.Wilson. *Adv. Electron. Mater.*, **1**, 1500062 (2015); https://doi.org/10.1002/aelm.201500062

227. I.Nikitskiy, S.Goossens, D.Kufer, T.Lasanta, G.Navickaite, F.H.L.Koppens, G.Konstantatos. *Nat. Commun.*, **7**, 11954 (2016); https://doi.org/10.1038/ncomms11954

228. Y.Zhang, M.Cao, X.Song, J.Wang, Y.Che, H.Dai, X.Ding, G.Zhang, J.Yao. *J. Phys. Chem. C*, **119** (37), 21739 (2015); https://doi.org/10.1021/acs.jpcc.5b07318

229. V.P.Ponomarenko, V.S.Popov, S.V.Popov. *J. Commun. Technol. Electron.*, **66** (9), 1108 (2021); https://doi.org/10.1134/S1064226921090138

230. V.P.Ponomarenko, V.S.Popov, S.V.Popov. *J. Commun. Technol. Electron.*, **67** (9), 1134 (2022); https://doi.org/10.1134/S1064226922090121

231. D.Kufer, I.Nikitskiy, T.Lasanta, G.Navickaite, F.H.L.Koppens, G.Konstantatos. *Adv. Mater.*, **27** (1), 176 (2015); https://doi.org/10.1002/adma.201402471

232. D.Kufer, T.Lasanta, M.Bernechea, F.H.L.Koppens, G.Konstantatos. *ACS Photonics*, **3** (7), 1324 (2016); https://doi.org/10.1021/acsphotonics.6b00299

233. Y.Yu, Y.Zhang, X.Song, H.Zhang, M.Cao, Y.Che, H.Dai, J.Yang, H.Zhang, J.Yao. *ACS Photonics*, **4** (4), 950 (2017); https://doi.org/10.1021/acsphotonics.6b01049

234. C.Hu, D.Dong, X.Yang, K.Qiao, D.Yang, H.Deng, S.Yuan, J.Khan, Y.Lan, H.Song, J.Tang. *Adv. Funct. Mater.*, **27** (2), 1603605 (2016); https://doi.org/10.1002/adfm.201603605

235. L.Gao, C.Chen, K.Zeng, C.Ge, D.Yang, H.Song, J.Tang. *Light: Sci. Appl.*, **5** (7), e16126 (2016); https://doi.org/10.1038/lsa.2016.126

236. A.-Y.Lee, H.-S.Ra, D.H.Kwak, M.-H.Jeong, J.-H.Park, Y.-S.Kang, W.-S.Chae, J.-S.Lee. *ACS Appl. Mater. Interfaces*, **10** (18), 16033 (2018); https://doi.org/10.1021/acsami.8b03285

237. C.You, G.Zhang, W.Deng, C.Zhao, B.An, B.Liu, B.Wang, H.Yan, D.Liu, Y.Zhang. *J. Mater. Chem. C*, **7**, 2232 (2019); https://doi.org/10.1039/c8tc05735d

238. J.Qiao, X.Kong, Z.-X.Hu, F.Yang, W.Ji. *Nat. Commun.*, **5**, 4475 (2014); https://doi.org/10.1038/ncomms5475

239. P.Chen, Z.Wu, Y.Shi, C.Li, J.Wang, J.Yang, X.Dong, J.Gou, J.Wang, Y.Jiang. *J. Mater. Sci. Mater. Electron.*, **32**, 9452 (2021); https://doi.org/10.1007/s10854-021-05609-y

240. H.Zhang, Y.Zhang, X.Song, Y.Yu, M.Cao, Y.Che, J.Wang, J.Yang, H.Dai, G.Zhang J.Yao. *Nanotechnology*, **27**, 425204 (2016); https://doi.org/10.1088/0957-4484/27/42/425204

241. Y.Che, X.Cao, J.Yao. *Opt. Mater.*, **89**, 138 (2019); https://doi.org/10.1016/j.optmat.2019.01.014

242. A.J.Ben-Sasson, D.Azulai, H.Gilon, A.Facchetti, G.Markovich, N.Tessler. *ACS Appl. Mater. Interfaces*, **7** (4), 2149 (2015); https://doi.org/10.1021/am505174p

243. P.Guyot-Sionnest, J.C.Peterson, C.Melnychuk. *J. Phys. Chem. C*, **126**, 17196 (2022); https://doi.org/10.1021/acs.jpcc.2c05391

244. S.Arya, A.Sharma, B.Singh, M.Riyas, P.Bandhoria, M.Aatif, V.Gupta. *Opt. Mater.*, **79**, 15 (2018); https://doi.org/10.1016/j.optmat.2018.03.035

245. S.Chand, N.Thakur, S.C.Katyal, P.B.Barman, V.Sharma, P.Sharma. *Sol. Energy Mater. Sol. Cells*, **168**, 183 (2017); https://doi.org/10.1016/j.solmat.2017.04.033

246. K.Byrappa, T.Adschiri. *Prog. Cryst. Growth Charact. Mater.*, **53**, 117 (2007); https://doi.org/10.1016/j.pcrysgrow.2007.04.001

247. Y.Zhao, X.-H.Liao, J.-M.Hong, J.-J.Zhu. *Mater. Chem. Phys.*, **87**, 149 (2004); https://doi.org/10.1016/j.matchemphys.2004.05.026

248. H.Lu, G.M.Carroll, N.R.Neale, M.C.Beard. *ACS Nano*, **13**, 939 (2019); https://doi.org/10.1021/ACSnano.8B09815

249. A.L.Efros, L.E.Brus. *ACS Nano*, **15**, 6192 (2021); https://doi.org/10.1021/acsnano.1c01399

250. J.W.Lee, D.Y.Kim, S.Baek, H.Yu, F.So. *Small*, **12**, 1328 (2016); https://doi.org/10.1002/smll.201503244

251. V.K.LaMer, R.H.Dinegar. *J. Am. Chem. Soc.*, **72**, 4847 (1950); https://doi.org/10.1021/ja01167a001

252. Y.Yin, A.P.Alivisatos. *Nature*, **437**, 664 (2005); https://doi.org/10.1038/nature04165

253. M.Yu.Koroleva, E.V.Yurtov. *Russ. Chem. Rev.*, **90**, 293 (2021); https://doi.org/10.1070/RCR4962

254. M.Yu.Koroleva, E.V.Yurtov. *Russ. Chem. Rev.*, **91** (5), RCR5024 (2022); https://doi.org/10.1070/RCR5024

255. C.Li, Y.Zhao, F.Li, Z.Shi, S.Feng. *Chem. Mater.*, **22**, 1901 (2010); https://doi.org/10.1021/cm903648c

256. M.P.Hendricks, M.P.Campos, G.T.Cleveland, I.Jen-La Plante, J.S.Owen. *Science*, **348**, 1226 (2015); https://doi.org/10.1126/science.aaa2951; https://doi.org/10.1126/science.aaa2951

257. B.Yuan, X.Tian, S.Shaw, R.E.Petersen, L.Cademartiri. *Phys. Status Solidi A*, **214**, 1600543 (2017); https://doi.org/10.1002/pssa.201600543

258. W.M.M.Lin, M.Yarema, M.Liu, E.Sargent, V.Wood. *Chimia*, **75**, 398 (2021); https://doi.org/10.3929/ethz-b-000488369

259. M.K.Norr. *J. Phys. Chem.*, **65**, 1278 (1961); https://doi.org/10.1021/j100825a507

260. J.W.Thomson, K.Nagashima, P.M.Macdonald, G.A.Ozin. *J. Am. Chem. Soc.*, **133**, 5036 (2011); https://doi.org/10.1021/ja1109997

261. C.M.Evans, M.E.Evans, T.D.Krauss. *J. Am. Chem. Soc.*, **132**, 10973 (2010); https://doi.org/10.1021/ja103805s

262. J.S.Steckel, B.K.H.Yen, D.C.Oertel, M.G.Bawendi. *J. Am. Chem. Soc.*, **128**, 13032 (2006); doi: 10.1021/ja062626g

263. L.M.De Leon Covian, J.A.Arizpe Zapata, M.A.Garza Navarro, D.I.Garza Gutierrez. *Chalcogenide Lett.*, **11**, 567 (2014)

V.P.Ponomarenko, V.S.Popov, I.A.Shuklov, V.V.Ivanov, V.F.Razumov

264. J.Joo, J.M.Pietryga, J.A.McGuire, S.-H.Jeon, D.J.Williams, H.-L.Wang, V.I.Klimov. *J. Am. Chem. Soc.*, **131**, 10620 (2009); https://doi.org/10.1021/ja903445

265. R.A.Ganeev, I.A.Shuklov, A.I.Zvyagin, D.V.Dyomkin, M.S.Smirnov, O.V.Ovchinnikov, A.A.Lizunova, A.M.Perepukhov, V.S.Popov, V.F.Razumov. *Opt. Express*, **29**, 16710 (2021); https://doi.org/10.1364/OE.425549

266. B.Hou, D.Benito-Alifonso, N.Kattan, D.Cherns, M.C.Galan, D.J.Fermín. *Chem. – Eur. J.*, **19**, 15847 (2013); https://doi.org/10.1039/c4ta00285g

267. T.-M.Wang, B.Gao, Q.Wang, M.Zhao, K.-B.Kang, Z.-G.Xu, H.-L.Zhang. *Chem. – Asian J.*, **8**, 912 (2013); https://doi.org/10.1002/asia.201201154

268. Y.Pan, M.A.Sohel, L.Pan, Z.Wei, H.Bai, M.C.Tamargo, R.John. *Mater. Today Proc.*, **2**, 281 (2015); https://doi.org/10.1016/j.matpr.2015.04.043

269. D.K.Smith, J.M.Luther, O.E.Semonin, A.J.Nozik, M.C.Beard. *ACS Nano*, **5**, 183 (2011); https://doi.org/10.1021/nn102878u

270. Y.Zhang, G.Wu, C.Ding, F.Liu, Y.Yao, Y.Zhou, C.Wu, N. Nakazawa, Q.Huang, T.Toyoda, R.Wang, S.Hayase, Z.Zou, Q.Shen. *J. Phys. Chem. Lett.*, **9**, 3598 (2018); https://doi.org/10.1021/acs.jpclett.8b01514

271. A.Nag, M.V.Kovalenko, J.-S.Lee, W.Liu, B.Spokoyny, D.V.Talapin. *J. Am. Chem. Soc.*, **133**, 10612 (2011); https://doi.org/10.1021/ja2029415

272. J.Y.Woo, J.-H.Ko, J.H.Song, K.Kim, H.Choi, Y.-H.Kim, D.C.Lee, S.Jeong. *J. Am. Chem. Soc.*, **136**, 8883 (2014); https://doi.org/10.1021/ja503957r

273. C.Fu, H.Wang, T.Song, L.Zhang, W.Li, B.He, M.Sulaman, S.Yang, B.Zou. *Nanotechnology*, **27**, 065201 (2016); https://doi.org/10.1088/0957-4484/27/6/065201

274. H.-M.So, J.Y.Woo, S.Jeong, W.S.Chang. *Opt. Mater. Express*, **7**, 2905 (2017); https://doi.org/10.1364/OME.7.002905

275. J.Y.Woo, S.Lee, S.Lee, W.D.Kim, K.Lee, K.Kim, H.J.An, D.C.Lee, S.Jeong. *J. Am. Chem. Soc.*, **138**, 876 (2016); https://doi.org/10.1021/acs.jpcc.6b10920

276. N.Goubet, A.Jagtap, C.Livache, B.Martinez, H.Portalès, X.Z.Xu, R.P.S.M.Lobo, B.Dubertret, E.Lhuillier. *J. Am. Chem. Soc.*, **140**, 5033 (2018); https://doi.org/10.1021/jacs.8b02039

277. I.A.Shuklov, I.S.Mikhel, A.V.Nevidimov, K.P.Birin, N.V.Dubrovina, A.A.Lizunova, V.F.Razumov. *ChemistrySelect*, **5**, 11896 (2020); https://doi.org/10.1002/slct.202002711

278. S.W.O'Neill, T.D.Krauss. *J. Am. Chem. Soc.*, **144**, 6251 (2022); https://doi.org/10.1021/jacs.1c11697

279. Y.Pan, H.Bai, L.Pan, Y.Li, M.C.Tamargo, M.Sohel, J.R.Lombardi. *J. Mater. Chem.*, **22**, 23593 (2012); https://doi.org/10.1039/c2jm15540k

280. I.A.Shuklov, A.A.Mardini, I.V.Skabitsky, N.V.Dubrovina, A.M.Perepukhov, A.A.Lizunova, V.F.Razumov. *Nano-Struc. Nano-Objects*, **35**, 101020 (2023); https://doi.org/10.1016/j.nanoso.2023.101020

281. H.Zhang, P.Guyot-Sionnest. *J. Phys. Chem. Lett.*, **11**, 6860 (2020); https://doi.org/10.1021/acs.jpclett.0c01550

282. L.Cademartiri, E.Montanari, G.Calestani, A.Migliori, A.Guagliardi, G.A.Ozin. *J. Am. Chem. Soc.*, **128**, 10337 (2006); https://doi.org/10.1021/ja063166u

283. D.Baranov, M.J.Lynch, A.C.Curtis, A.R.Carollo, C.R.Douglass, A.M.Mateo-Tejada, D.M.Jonas. *Chem. Mater.*, **31**, 1223 (2019); https://doi.org/10.1021/acs.chemmater.8b04198

284. A.Antanovich, A.Prudnikau, M.Artemyev. *J. Phys. Chem. C*, **118**, 21104 (2014); https://doi.org/10.1021/jp506479

285. T.T.Tan, S.T.Selvan, L.Zhao, S.Gao, J.Y.Ying. *Chem. Mater.*, **19**, 3112 (2007); https://doi.org/10.1021/cm061974e

286. A.Bundulis, I.A.Shuklov, V.V.Kim, A.A.Mardini, J.Grube, J.Alnis, A.A.Lizunova, V.F.Razumov, R.A.Ganeev. *Nanomaterials*, **11**, 3351 (2021); https://doi.org/10.3390/nano11123351

287. E.Bossavit, J.Qu, C.Abadie, C.Dabard, T.Dang, E.Izquierdo, A.Khalili, C.Gréboval, A.Chu, S.Pierini, M.Cavallo, Y.Prado, V.Parahyba, X.Z.Xu, A.Decamps Mandine, M.Silly, S.Ithurria, E.Lhuillier. *Adv. Opt. Mater.*, **10**, 2101755 (2022); https://doi.org/10.1002/adom.202101755

288. Y.Prado, J.Qu, C.Gréboval, C.Dabard, P.Rastogi, A.Chu, A.Khalili, X.Z.Xu, C.Delerue, S.Ithurria, E.Lhuillier. *Chem. Mater.*, **33**, 2054 (2021); https://doi.org/10.1021/acs.chemmater.0c04526

289. S.S.Al-Showiman. *Inorg. Chim. Acta*, **141**, 263 (1988); https://doi.org/10.1016/S0020-1693(00)83918-3

290. F.P.G. de Arquer, D.V.Talapin, V.I.Klimov, Y.Arakawa, M.Bayer, E.H.Sargent. *Science*, **373**, (2021); https://doi.org/10.1126/science.aaz8541

291. A.V.Lukashin, N.S.Falaleev, N.I.Verbitskiy, A.A.Volykhov, I.I.Verbitskiy, L.V.Yashna, A.S.Kumskov, N.A.Kiselev, A.A.Eliseev. *Nanosyst.: Phy. Chem. Math.*, **6**, 850 (2015); https://doi.org/10.17586/2220-8054-2015-6-6-850-856

292. *Lead Sulfide (PbS) Crystal Ctructure, Lattice Parameters, Thermal Expansion*. (Eds O.Madelung, U.Rössler, M.Schulz) In *Non-Tetrahedrally Bonded Elements and Binary Compounds I* (Berlin, Heidelberg: Springer-Verlag, 1998); https://doi.org/10.1007/10681727_889

293. *Lead Sulfide (PbS) Crystal Ctructure, Lattice Parameters, Thermal Expansion*. (Eds O.Madelung, U.Rössler, M.Schulz) In *Non-Tetrahedrally Bonded Elements and Binary Compounds I* (Berlin, Heidelberg: Springer-Verlag, 1998); https://doi.org/10.1007/10681727_903

294. *Lead Sulfide (PbS) Crystal Ctructure, Lattice Parameters, Thermal Expansion*. (Eds O.Madelung, U.Rössler, M.Schulz) In *Non-Tetrahedrally Bonded Elements and Binary Compounds I* (Berlin, Heidelberg: Springer-Verlag, 1998); https://doi.org/10.1007/10681727_711

295. Y.Jun, J.-H.Lee, J.Choi, J.Cheon. *J. Phys. Chem. B*, **109**, 14795 (2005); https://doi.org/10.1021/jp052257v

296. H.-Y.Si, D.Yuan, J.-S.Chen, G.-M.Chow. *RSC Adv.*, **1**, 817 (2011); https://doi.org/10.1039/c1ra00279a

297. Y.Kim, F.Che, J.W.Jo, J.Choi, F.P.G.de Arquer, O.Voznyy, B.Sun, J.Kim, M.Choi, R.Quintero Bermudez, F.Fan, C.S.Tan, E.Bladt, G.Walters, A.H.Proppe, C.Zou, H.Yuan, S.Bals, J.Hofkens, M.B.J.Roeffaers, S.Hoogland, E.H.Sargent. *Adv. Mater.*, **31**, 1805580 (2019); https://doi.org/10.1002/adma201805580

298. Y.Xia, W.Chen, P.Zhang, S.Liu, K.Wang, X.Yang, H.Tang, L.Lian, J.He, X.Liu, G.Liang, M.Tan, L.Gao, H.Liu, H.Song, D.Zhang, J.Gao, K.Wang, X.Lan, X.Zhang, P.Müller Buschbaum, J.Tang, J.Zhang. *Adv. Funct. Mater.*, **30**, 2000594 (2020); https://doi.org/10.1002/adfm.202000594

299. W.K.Bae, J.Joo, L.A.Padilha, J.Won, D.C.Lee, Q.Lin, W.Koh, H.Luo, V.I.Klimov, J.M.Pietryga. *J. Am. Chem. Soc.*, **134**, 20160 (2012); https://doi.org/10.1021/ja309783v

300. A.L.Hagström, A.Fahlman. *Appl. Surf. Sci.*, **1**, 455 (1978); https://doi.org/10.1016/0378-5963(78)90024-7

301. C.Zha, C.Ji, J.Zhang, L.Shen, X.Zhang, S.Dong, N.Bao. *RSC Adv.*, **6**, 107151 (2016); https://doi.org/10.1039/C6RA24119K

302. I.A.Shuklov, V.F.Toknova, A.A.Lizunova, V.F.Razumov. *Mater. Today Chem.*, **18**, 100357 (2020); https://doi.org/10.1016/j.mtchem.2020.100357

303. W.Koh, S.R.Saudari, A.T.Fafarman, C.R.Kagan, C.B.Murray. *Nano Lett.*, **11**, 4764 (2011); https://doi.org/10.1021/nl202578g

304. Z.Quan, W.S.Loc, C.Lin, Z.Luo, K.Yang, Y.Wang, H.Wang, Z.Wang, J.Fang. *Nano Lett.*, **12**, 4409 (2012); https://doi.org/10.1021/nl302324b

305. R.A.Ganeev, I.A.Shuklov, A.I.Zvyagin, D.V.Dyomkin, S.I.Bocharova, V.S.Popov, V.F.Toknova, A.A.Lizunova, O.V.Ovchinnikov, V.F.Razumov. *Opt. Mater.*, **121**, 111499 (2021); https://doi.org/10.1016/j.optmat.2021.111499

306. J.E.Murphy, M.C.Beard, A.G.Norman, S.P.Ahrenkiel, J.C.Johnson, P.Yu, O.I.Mićić, R.J.Ellingson, A.J.Nozik. *J. Am. Chem. Soc.*, **128**, 3241 (2006); https://doi.org/10.1021/ja057497

V.P.Ponomarenko, V.S.Popov, I.A.Shuklov, V.V.Ivanov, V.F.Razumov
Russ. Chem. Rev., 2024, **93** (4) RCR5113

47 of 48

307. A.H.Ip, A.Kiani, I.J.Kramer, O.Voznyy, H.F.Movahed, L.Levina, M.M.Adachi, S.Hoogland, E.H.Sargent. *ACS Nano*, **9**, 8833 (2015); https://doi.org/10.1021/acsnano.5b02164

308. H.Choi, J.-H.Ko, Y.-H.Kim, S.Jeong. *J. Am. Chem. Soc.*, **135**, 5278 (2013); https://doi.org/10.1021/ja400948t

309. H.R.You, J.Y.Park, D.H.Lee, Y.Kim, J.Choi. *Appl. Sci.*, **10**, 975 (2020); https://doi.org/10.3390/app10030975

310. A.Kiani, B.R.Sutherland, Y.Kim, O.Ouellette, L.Levina, G.Walters, C.-T.Dinh, M.Liu, O.Voznyy, X.Lan, A.J.Labelle, A.H.Ip, A.Proppe, G.H.Ahmed, O.F.Mohammed, S.Hoogland, E.H.Sargent. *Appl. Phys. Lett.*, **109**, 183105 (2016); https://doi.org/10.1063/1.4966217

311. M.Liu, O.Voznyy, R.Sabatini, F.P.G.de Arquer, R.Munir, A.H.Balawi, X.Lan, F.Fan, G.Walters, A.R.Kirmani, S.Hoogland, F.Laquai, A.Amassian, E.H.Sargent. *Nat. Mater.*, **16**, 258 (2017); https://doi.org/10.1038/NMAT4800

312. M.M.van der Sluijs, D.Sanders, K.J.Jansen, G.Soligno, D.Vanmaekelbergh, J.L.Peters. *J. Phys. Chem. C*, **126**, 986 (2022); https://doi.org/10.1021/acs.jpcc.1c07430

313. J.L.Peters, T.Altantzis, I.Lobato, M.A.Jazi, C.van Overbeek, S.Bals, D.Vanmaekelbergh, S.B.Sinai. *Chem. Mater.*, **30**, 4831 (2018); https://doi.org/10.1021/acs.chemmater.8b02178

314. J.Zhang, A.Kumbhar, J.He, N.C.Das, K.Yang, J.-Q.Wang, H.Wang, K.L.Stokes, J.Fang. *J. Am. Chem. Soc.*, **130**, 15203 (2008); https://doi.org/10.1021/ja806120w

315. S.Yamamuro, K.Sumiyama. *Chem. Phys. Lett.*, **418**, 166 (2006); https://doi.org/10.1016/j.cplett.2005.10.111

316. *Nanoscale Materials in Chemistry.* (Eds K.J.Klabunde, R.M.Richards). (Wiley, 2009); https://doi.org/10.1002/9780470523674

317. S.Acharya, U.K.Gautam, T.Sasaki, Y.Bando, Y.Golan, K.Ariga. *J. Am. Chem. Soc.*, **130**, 4594 (2008); https://doi.org/10.1021/ja711064b

318. J.M.Luther, H.Zheng, B.Sadtler, A.P.Alivisatos. *J. Am. Chem. Soc.*, **131**, 16851 (2009); https://doi.org/10.1021/ja906503w

319. A.C.Onicha, N.Petchsang, T.H.Kosel, M.Kuno. *ACS Nano*, **6**, 2833 (2012); https://doi.org/10.1021/nn300373w

320. W.Koh, Y.Yoon, C.B.Murray. *Chem. Mater.*, **23**, 1825 (2011); https://doi.org/10.1021/cm1033172

321. B.-R.Hyun, A.C.Bartnik, W.Koh, N.I.Agladze, J.P.Wrubel, A.J.Sievers, C.B.Murray, F.W.Wise. *Nano Lett.*, **11**, 2786 (2011); https://doi.org/10.1021/nl201115

322. J.E.Boercker, E.E.Foos, D.Placencia, J.G.Tischler. *J. Am. Chem. Soc.*, **135**, 15071 (2013); https://doi.org/10.1021/ja404576j

323. L.Han, D.M.Balazs, A.G.Shulga, M.Abdu Aguye, W.Ma, M.A.Loi. *Adv. Electron. Mater.*, **4**, 1 (2018); https://doi.org/10.1002/aelm.201700580

324. K.-S.Cho, D.V.Talapin, W.Gaschler, C.B.Murray. *J. Am. Chem. Soc.*, **127**, 7140 (2005); https://doi.org/10.1021/ja050107s

325. T.Mokari, M.Zhang, P.Yang. *J. Am. Chem. Soc.*, **129**, 9864 (2007); https://doi.org/10.1021/ja074145i

326. J.Novák, R.Banerjee, A.Kornowski, M.Jankowski, A.André, H.Weller, F.Schreiber, M.Scheele. *ACS Appl. Mater. Interfaces*, **8**, 22526 (2016); https://doi.org/10.1021/acsami.6b06989

327. T.Huang, Q.Zhao, J.Xiao, L.Qi. *ACS Nano*, **4**, 4707 (2010); https://doi.org/10.1021/nn101272y

328. N.Zhao, L.Qi. *Adv. Mater.*, **18**, 359 (2006); https://doi.org/10.1002/adma.200501756

329. A.Abu-Hariri, A.K.Budniak, F.Horani, E.Lifshitz. *RSC Adv.*, **11**, 30560 (2021); https://doi.org/10.1039/d1ra04402h

330. Y.Wang, Q.Dai, X.Yang, B.Zou, D.Li, B.Liu, M.Z.Hu, G.Zou. *CrystEngComm*, **13**, 199 (2011); https://doi.org/10.1039/c004459h

331. *Mercury Telluride (HgTe). Lattice Parameters.* (Eds O.Madelung, U.Rössler, M.Schulz). In *II-VI and I-VII Compounds; Semimagnetic Compounds*. (Berlin, Heidelberg: Springer-Verlag, 2005); https://doi.org/10.1007/10681719_677

332. J.Yang, H.Hu, Y.Lv, M.Yuan, B.Wang, Z.He, S.Chen, Y.Wang, Z.Hu, M.Yu, X.Zhang, J.He, J.Zhang, H.Liu, H.-Y.Hsu, J.Tang, H.Song, X.Lan. *Nano Lett.*, **22**, 3465 (2022); https://doi.org/10.1021/acs.nanolett.2c00950

333. J.Zhang, B.D.Chernomordik, R.W.Crisp, D.M.Kroupa, J.M.Luther, E.M.Miller, J.Gao, M.C.Beard. *ACS Nano*, **9**, 7151 (2015); https://doi.org/10.1021/acsnano.5b01859

334. C.Zhang, Y.Xia, Z.Zhang, Z.Huang, L.Lian, X.Miao, D.Zhang, M.C.Beard, J.Zhang. *Chem. Mater.*, **29**, 3615 (2017); https://doi.org/10.1021/acs.chemmater.7b00411

335. R.Wang, Y.Shang, P.Kanjanaboos, W.Zhou, Z.Ning, E.H.Sargent. *Energy Environ. Sci.*, **9**, 1130 (2016); https://doi.org/10.1039/C5EE03887A

336. M.J.Choi, F.P.G. de Arquer, A.H.Proppe, A.Seifitokaldani, J.Choi, J.Kim, S.W.Baek, M.Liu, B.Sun, M.Biondi, B.Scheffel, G.Walters, D.H.Nam, J.W.Jo, O.Ouellette, O.Voznyy, S.Hoogland, S.O.Kelley, Y.S.Jung, E.H.Sargent. *Nat. Commun.*, **11**, 1 (2020); https://doi.org/10.1038/s41467-019-13437-2

337. Z.Ning, D.Zhitomirsky, V.Adinolfi, B.Sutherland, J.Xu, O.Voznyy, P.Maraghechi, X.Lan, S.Hoogland, Y.Ren, E.H.Sargent. *Adv. Mater.*, **25**, 1719 (2013); https://doi.org/10.1002/adma.201204502

338. M.Yuan, D.Zhitomirsky, V.Adinolfi, O.Voznyy, K.W.Kemp, Z.Ning, X.Lan, J.Xu, J.Y.Kim, H.Dong, E.H.Sargent. *Adv. Mater.*, **25**, 5586 (2013); https://doi.org/10.1002/adma201302802

339. O.Voznyy, D.Zhitomirsky, P.Stadler, Z.Ning, S.Hoogland, E.H.Sargent. *ACS Nano*, **6**, 8448 (2012); https://doi.org/10.1021/nn303364d

340. D.Kim, D.-H.Kim, J.-H.Lee, J.C.Grossman. *Phys. Rev. Lett.*, **110**, 196802 (2013); https://doi.org/10.1103/PhysRevLett.110.196802

341. D.M.Balazs, K.I.Bijlsma, H.-H.Fang, D.N.Dirin, M.Döbeli, M.V.Kovalenko, M.A.Loi. *Sci. Adv.*, **3** (1) (2017); https://doi.org/10.1126/sciadv.aao1558

342. D.V.Talapin, C.B.Murray. *Science*, **310**, 86 (2005); https://doi.org/10.1126/science.1116703

343. D.Zhitomirsky, M.Furukawa, J.Tang, P.Stadler, S.Hoogland, O.Voznyy, H.Liu, E.H.Sargent. *Adv. Mater.*, **24**, 6181 (2012); https://doi.org/10.1002/adma.201202825

344. D.Bederak, D.M.Balazs, N.V.Sukharevska, A.G.Shulga, M.Abdu-Aguye, D.N.Dirin, M.V.Kovalenko, M.A.Loi. *ACS Appl. Nano Mater.*, **1**, 6882 (2018); https://doi.org/10.1021/acsanm.8b01696

345. J.Tang, K.W.Kemp, S.Hoogland, K.S.Jeong, H.Liu, L.Levina, M.Furukawa, X.Wang, R.Debnath, D.Cha, K.W.Chou, A.Fischer, A.Amassian, J.B.Asbury, E.H.Sargent. *Nat. Mater.*, **10**, 765 (2011); https://doi.org/10.1038/NMAT3118

346. S.W.Baek, P.Molet, M.J.Choi, M.Biondi, O.Ouellette, J.Fan, S.Hoogland, F.P.G. de Arquer, A.Mihi, E.H.Sargent. *Adv. Mater.*, **31**, 1901745 (2019); https://doi.org/10.1002/adma.201901745

347. B.Martinez, C.Livache, N.Goubet, A.Jagtap, H.Cruguel, A.Ouerghi, E.Lacaze, M.G.Silly, E.Lhuillier. *J. Phys. Chem. C*, **122**, 859 (2018); https://doi.org/10.1021/acs.jpcc.7b09972

348. M.Chen, X.Lan, X.Tang, Y.Wang, M.H.Hudson, D.V.Talapin, P.Guyot-Sionnest. *ACS Photonics*, **6**, 2358 (2019); https://doi.org/10.1021/acsphotonics.9b01050

349. M.Chen, G.Shen, P.Guyot-Sionnest. *J. Phys. Chem. Lett.*, **11**, 2303 (2020); https://doi.org/10.1021/acs.jpclett.0c00587

350. M.Chen, Q.Hao, Y.Luo, X.Tang. *ACS Nano*, **16**, 11027 (2022); https://doi.org/10.1021/acsnano.2c03631

351. R.H.Harada, H.T.Minden. *Phys. Rev.*, **102**, 1258 (1956); https://doi.org/10.1103/PhysRev.102.1258

352. H.T.Dastjerdi, R.Tavakoli, P.Yadav, D.Prochowicz, M.Saliba, M.M.Tavakoli. *ACS Appl. Mater. Interfaces*, **11**, 26047 (2019); https://doi.org/10.1021/acsami.9b08466

353. B.K.Jung, H.K.Woo, C.Shin, T.Park, N.Li, K.J.Lee, W.Kim, J.H.Bae, J.Ahn, T.N.Ng, S.J.Oh. *Adv. Opt. Mater.*, **10**, 2101611 (2022); https://doi.org/10.1002/adom.202101611

354. B.Sun, M.Vafaie, L.Levina, M.Wei, Y.Dong, Y.Gao,
     H.T.Kung, M.Biondi, A.H.Proppe, B.Chen, M.-J.Choi,
     L.K.Sagar, O.Voznyy, S.O.Kelley, F.Laquai, Z.-H.Lu,
     S.Hoogland, F.P.G. de Arquer, E.H.Sargent. *Nano Lett.*, **20**,
     3694 (2020); https://doi.org/10.1021/acs.nanolett.0c00638

355. G.M.Dalpian, J.R.Chelikowsky. *Phys. Rev. Lett.*, **96**, 226802
     (2006); https://doi.org/10.1103/PhysRevLett.96.226802

356. D.J.Norris, A.L.Efros, S.C.Erwin. *Science*, **319**, 1776 (2008);
     https://doi.org/10.1126/science.1143802

357. M.S.Kang, A.Sahu, C.D.Frisbie, D.J.Norris. *Adv. Mater.*, **25**,
     725 (2013); https://doi.org/10.1002/adma.201203114

358. A.Stavrinadis, A.K.Rath, F.P.G. de Arquer, S.L.Diedenhofen,
     C.Magén, L.Martinez, D.So, G. Konstantatos. *Nat. Commun.*,
     4, 2981 (2013); https://doi.org/10.1038/ncomms3981

359. M.Allen, A.Bessonov, T.Ryhänen. *Proc. SID Symp. Dig. Tech.
     Papers*, **52** (1), 987 (2021); https://doi.org/10.1002/sdtp.14855

360. V.S.Popov, V.P.Ponomarenko, S.V.Popov. *Appl. Phys.*, **6**, 45
     (2023); https://doi.org/10.51368/1996-0948-2023-6-45-53

361. Y.Wang, L.Peng, J.Schreier, Y.Bi, A.Black, A.Malla,
     S. Goossens, G.Konstantatos. *Nat. Photon.*, **18**, 236 (2024);
     https://doi.org/10.1038/s41566-023-01345-3